Fluid flow in porous media: A combined numerical and experimental approach

Dissertation

zur Erlangung des Doktorgrades (Dr. rer. nat.)
der Bayreuther Graduiertenschule für Mathematik und Naturwissenschaften (BayNAT)

vorgelegt von
Philipp Eichheimer, geboren in Bensheim

Bayreuth, 2019

Die vorliegende Arbeit wurde in der Zeit von November 2016 bis Dezember 2019 in Bayreuth am Bayerischen Geoinstitut unter Betreuung von Prof. Dr. Gregor J. Golabek angefertigt.

Vollständiger Abdruck der von der Bayreuther Graduiertenschule für Mathematik und Naturwissenschaften (BayNAT) der Universität Bayreuth genehmigten Dissertation zur Erlangung des akademischen Grades eines Doktors der Naturwissenschaften (Dr. rer. nat.).

Dissertation eingereicht am:	17. Dezember 2019
Zulassung durch das Leitungsgremium:	17. Dezember 2019
Wissenschaftliches Kolloquium:	11. Februar 2020

Amtierender Direktor: Prof. Dr. Markus Lippitz

Prüfungsausschuss:

Prof. Dr. Gregor J. Golabek	(Gutachter)
PD Dr. Gerd Steinle-Neumann	(Gutachter)
Prof. Dr. Daniel Frost	(Vorsitz)
Prof. Dr. Michihiko Nakamura	

"All truths are easy to understand once they are discovered;
the point is to discover them."

—Galileo Galilei

Abstract

Earth's plate tectonics provides the basis for different material cycles, which exchange chemical compounds, like water, between Earth's surface and mantle. At subduction zones, the oceanic lithosphere sinks into the mantle, transporting both chemically bound water within minerals and free water within its pore space into Earth's interior. At shallow depth the free water is expelled from the pore space through compaction. However, a significant amount of water remains chemically bound in hydrous mineral phases. With increasing pressure and temperatures those hydrous minerals break down, releasing water, which percolates into the mantle wedge. Those dehydration reactions provide the main source of water in subduction zones, causing partial melt in the mantle wedge and trigger volcanism at the Earth's surface. As already small amounts of water have significant effects on chemical and physical properties of the mantle, it is therefore of crucial importance to constrain the amount of water entering the Earth's mantle. Until now the distribution and total amount of water in Earth's mantle is under debate and estimates for water storage in the deeper mantle range from 0.25 - 4 ocean masses. For this reason it is of major importance for several geoscience disciplines, including Hydrogeology, Petrophysics and Volcanology to investigate fluid flow and its related processes on various scales.

A key parameter controlling fluid flow is the permeability of rocks. Thus, as permeability is a function of the rock microstructure, an accurate determination and prediction of this parameter is necessary. Numerical predictions, where laboratory measurements struggle, has become an important method to complement laboratory approaches. Employing high grid resolutions, this prediction becomes computationally very expensive, which makes it necessary to develop methods that maximize accuracy and efficiency. For this reason the method of stencil rescaling is implemented into the Finite Difference code *LaMEM (Lithosphere and Mantle Evolution Model)* by Anton Popov. The stencil rescaling method improves the description of the solid-fluid interface and therefore allows for a more accurate computation of permeability in porous media using Darcy's law at low Reynolds numbers. The ac-

curacy of this method is successfully verified by comparing numerical to analytical solutions for a set of simplified model setups. Results show that stencil rescaling significantly increases the accuracy at no additional computational costs. Additionally, the modeling framework is used to predict the permeability of a Fontainebleau sandstone and to demonstrate numerical convergence. Results show very good agreement with experimental measurements as well as with previous studies. As the flow of non-Newtonian fluids through porous media has gained importance in recent years due to, e.g. the use of nanofluids for enhanced oil recovery, additionally the ability of the code to simulate the flow of power-law fluids through porous media is also demonstrated. As in case of a Newtonian fluid, results show good agreement with analytical solutions.

However, as most of Earth's dynamics like magma migration and ground water flow occur on a larger scale, it is necessary to parameterize permeability, which can be used as input parameter to investigate fluid flow in large-scale numerical simulations. For this reason several soda-lime glass bead samples with various porosities are sintered. Microstructural parameters like effective porosity and effective specific surface are determined using image processing. Furthermore, flow properties like hydraulic tortuosity and permeability are computed using *LaMEM*. By fitting an analytical equation for the microstructural and flow properties to porosity, a modified Kozeny-Carman equation for isotropic low-porosity media is obtained. This permeability parameterization can be used to simulate fluid flow on the large-scale. In comparison to numerically computed and experimentally measured permeability values this parameterization shows good agreement.

To investigate also the fluid flow on the macroscale results on modelling fluid flow in subduction zones are presented. In a first step a corner flow benchmark is performed successfully and a water migration scheme is implemented into the Finite Element code *MVEP2*. Water migration is modelled with the following three steps:

1) Determination of the amount of free water and bound water as well as the maximum storage capacity of each marker.

2) Extraction of the pressure gradients of the solid phase flow to compute Darcy velocities.

3) Advection of the free water along the computed Darcy velocities.

Markers containing more chemically bound water than the storage capacity are oversaturated and dehydrate, whereas markers are undersaturated if the chemically bound water is below the water storage capacity, leading to hydration in case water is present. First simulations using this routine with different grid resolutions show that the total amount of water is conserved. Future studies are required to include temperature profiles and several normal faults, enriched with water, to finally investigate the effect on the resulting fluid flow within subduction zones.

Zusammenfassung

Plattentektonik auf der Erde bildet die Grundlage für verschiedene Materialzyklen, welche chemische Komponenten, wie beispielsweise Wasser, zwischen der Erdoberfläche und dem Erdmantel austauschen. An Subduktionszonen sinkt die ozeanische Lithosphäre in den Erdmantel und transportiert in Mineralen gebundenes und freies Porenwasser ins Erdinnere. Während Porenwasser bereits in geringen Tiefen durch Kompaktion freigesetzt wird, kann das in Mineralen gespeicherte Wasser in größere Tiefen transportiert werden. Mit zunehmendem Druck und Temperatur jedoch zerfallen ebenso jene wasserhaltigen Minerale, und Wasser gelangt in den darüberliegenden Mantelkeil. Diese Zerfallsreaktionen bilden die Hauptquelle für Wasser im Erdmantel, welche sowohl partielles Schmelzen im Mantelkeil als auch Vulkanismus an der Erdoberfläche verursachen. Da bereits eine geringe Menge an Wasser einen signifikanten Einfluss auf die chemischen und physikalischen Eigenschaften des Mantels hat, ist die Ermittlung der Menge an Wasser im Mantel von erheblicher Relevanz. Bis heute ist die genaue Menge und Verteilung des im Erdmantel vorhandenen Wassers umstritten und Schätzungen reichen von Werten zwischen 0.25 und 4 Ozeanmassen. Daher ist es von entscheidender Bedeutung für unterschiedliche geologische Disziplinen – wie der Hydrogeologie, Petrophysik und Vulkanologie – Flüssigkeitsströmungen und damit verbundene Prozesse auf verschiedenen Größenskalen zu untersuchen.

Ein Schlüsselparameter, der die Flüssigkeitsströmungen kontrolliert, ist die Permeabilität der Gesteine. Da diese jedoch eine Funktion der Mikrostruktur darstellt, ist deren präzise Bestimmung und Prognose auf der Mikroskala notwendig. Permeabilitätsbestimmungen werden meist experimentell durchgeführt, wobei diese oftmals eine Vielzahl an Einschränkungen aufweisen. Um diesen entgegenzuwirken, können numerische Berechnungen ergänzend hinzugezogen werden. Da diese sehr rechenintensiv sind, ist die Entwicklung neuer Techniken und Methoden zur Verbesserung der Präzision und Effizienz der Messwerte notwendig. Aufgrund dessen wurde die *Stencil-rescaling-Methode* in den Finite Differenzen-Code *LaMEM (Lithosphere and Mantle Evolution Model)* genutzt. Die *Stencil-rescaling-Methode* verbessert

die Beschreibung der Trennfläche zwischen Flüssigkeit und Gestein und erlaubt mit Hilfe des Gesetzes von Darcy eine präzisere Bestimmung der Permeabilität in porösen Medien bei niedrigen Reynoldszahlen. Zur Verifizierung der Methodenpräzision werden anhand verschiedener einfacher Modelle numerische mit analytischen Lösungen verglichen. Die Ergebnisse zeigen, dass das *Stencil-rescaling* die Präzision ohne zusätzlichen Rechenaufwand signifikant erhöht. Ergänzend dazu wird in diesem Rahmen die Permeabilität eines Fontainebleau Sandsteins modelliert und hierbei numerische Konvergenz gezeigt. Die Resultate sind in sehr guter Übereinstimmung mit experimentellen Messungen und vorherigen Studien. Aufgrund des sichtbar steigenden Interesses an Strömungen nicht-Newtonischer Flüssigkeiten, wie beispielsweise der Benutzung von Nanofluiden zur tertiären Ölgewinnung, wird die Fähigkeit des Codes gezeigt, Strömungen durch poröse Materialien mit nichtlinearen Rheologien zu simulieren. Wie im vorherigen Fall, stehen ebenso hierbei die Ergebnisse im guten Einklang mit analytischen Lösungen.

Da jedoch die meisten dynamischen Prozesse in der Erde, wie beispielsweise die Magmamigration sowie die Grundwasserströmungen, auf großen Skalen stattfinden, ist eine Parametrisierung der Permeabilität von der Mikroskala auf die Makroskala notwendig. Aufgrund dessen werden verschiedene Natron-Kalk-Glasproben mit unterschiedlichen Porositäten gesintert. Daraufhin werden die Mikrostrukturparameter - wie effektive Porosität und effektive spezifische Oberfläche -mit Hilfe von Bilddatenverarbeitung bestimmt. Des Weiteren werden Strömungsparameter - wie hydraulische Tortuosität und Permeabilität - mit *LaMEM* berechnet. Durch das Fitten einer analytischen Gleichung für diese Parameter an die Porosität kann eine modifizierte Kozeny-Carman-Gleichung für isotrope Materialen mit geringen Porositäten erhalten werden. Diese Parametrisierung kann im Weiteren dazu benutzt werden, Permeabilität in großskaligen Modellen zu simulieren. Um diese Parametrisierung zu überprüfen, wird diese mit experimentell gemessenen und numerisch berechneten Werten der Permeabilität vergleichen. Hierbei lassen sich innerhalb der generierten Ergebnisse gute Übereinstimmungen feststellen.

Um ebenso die Flüssigkeitsströmungen auf der Makroskala untersuchen zu können, werden Flüssigkeitsströmungen in Subduktionszonen modelliert. In einem ersten Schritt wird ein Corner-flow-benchmark erfolgreich reproduziert sowie eine Wasser-Migrations-Routine in drei Schritten in den Finite Elemente-Code *MVEP2* implementiert. Diese Routine besteht aus folgenden Schritten:

1) Die Menge an freiem und gebundenem Wasser sowie die maximale Wasserspeicherkapazität jedes Markers wird bestimmt.

2) Um Darcy-Geschwindigkeiten zu berechnen werden die Druckgradienten im Gestein extrahiert.

3) Das freie Wasser wird mit den berechneten Darcy-Geschwindigkeiten advektiert.

Marker, in denen die Menge des chemisch gebundenen Wassers über der Speicherkapazität liegt, sind übersättigt und dehydrieren, wobei freies Wasser entsteht. Marker, die weniger chemisch gebundenes Wasser enthalten als die Speicherkapazität erlaubt, sind untersättigt und hydrieren, falls Umgebungswasser zur Verfügung steht. Simulationen mit verschiedenen Gitterauflösungen zeigen, dass innerhalb der Routine die Gesamtmenge des Wassers erhalten bleibt. Zukünftige Studien sollten ein Temperaturfelde sowie mehrere Abschiebungen, welche mit Wasser gefüllt sind, beinhalten, um schlussendlich den Effekt auf die resultierende Flüssigkeitsströmung in einer Subduktionszone zu untersuchen.

Contents

List of Figures

List of Tables

Chapter 1 | Introduction

1.1 Deep Earth Volatile Cycle

Earth's dynamic nature influenced and shaped the history of humankind since its beginning. In 1912 Alfred Wegener introduced the theory of continental drift (Wegener, 1912), which was further developed into the theory of plate tectonics (Morgan, 1968; Wilson et al., 2014) that is supposed to drive most of Earth's dynamics. Today it is well-known that oceanic and continental plates float atop the mechanically weaker asthenospheric mantle (Clauser, 2014). Where plates meet, different types of boundaries relative to their motion develop, namely convergent, divergent and transform fault. Along convergent boundaries between oceanic and continental plates, the oceanic plate subducts below the continental one due to density differences and is dragged into the mantle. At these subduction zones major expressions of Earth's dynamics like earthquakes, volcanic activity and mountain-building occur (Crowley et al., 2011; Hacker, 2008; van Keken et al., 2002).

Additionally, subduction zones provide the input mechanism for deep material cycles. Within the Deep Earth Volatile Cycle, volatiles like water, sulfur, nitrogen and carbon are exchanged between Earth's surface and the deeper mantle (Hirschmann and Dasgupta, 2009; Dasgupta and Hirschmann, 2010; Hirschmann, 2018). One of the key players, taking an important role in Earth's evolution and dynamics, is H_2O as it affects the chemical (Bercovici and Karato, 2003) and physical properties (Hirth and Kohlstedt, 1995; Mei and Kohlstedt, 2000) of the mantle. H_2O can be transported into Earth's mantle via (i) pore water, (ii) hydrous minerals and (iii) Nominally Anhydrous Minerals (NAMs). At the seafloor, oceanic plates are transported from mid ocean ridges towards subduction zones by plate tectonics. Throughout the plate's residence on the seafloor sediments are added continously onto it, storing both pore water and chemically bound water. Additionally by cooling and bending the oceanic crust becomes fractured (Faccenda et al., 2009; Hatakeyama et al., 2017), hydrating the uppermost few kilometers of the oceanic plate (Peacock, 2001; Ranero et al., 2003). The pore water is expelled by compaction at shallow depths (4-11 km) into the mantle (Abers et al., 2017; van Keken et al., 2011; Korenaga, 2017), whereas chemically bound water may be transported deeper into the mantle. Finally, due to hydrothermal activity the basaltic crust and underlying peridotite react with seawater to form hydrous minerals such as amphibole, chlorite, and serpentine (Watts et al., 1980; McAdoo and Martin, 1984; Schmidt and Poli, 1998; Iwamori, 2004; Rüpke et al., 2004). However, most of the hydrous minerals break down during subduction releasing H_2O through dehydration reactions. The released aqueous fluids migrate into the overlying mantle wedge, where they may trigger partial melting to form volcanic arcs (Syracuse et al., 2010; van Keken et al., 2008). In cold subduc-

tion zones, hydrous minerals can carry H_2O down to depths in excess of 200 km (Schmidt and Poli, 1998). The transition zone is marked by two distinct seismic discontinuities, the 410 km, where olivine transforms into wadsleyite and the 660 km where wadsleyite turns into ringwoodite (Frost and McCammon, 2008; Jacobsen and Smyth, 2013). As both minerals can host significant amounts of H_2O, Earth's transition zone is supposed to serve as a major H_2O reservoir, fed by continously sinking slabs (Smyth and Jacobsen, 2013).

However, the distribution and total amount of water stored in Earth's mante is poorly understood. Experimental and theoretical studies suggest that upper mantle rocks, especially transition zone rocks, have the ability to store significant amounts of water within their crystal structure (Smyth, 1987; Ohtani, 2005), while the water storage capacity decreases in the lower mantle (Bercovici and Karato, 2003). Estimates for the amount of water within the entire mantle range from $\approx 0.25 - 4$ ocean masses (Ringwood, 1975; Ahrens, 1989; Jambon and Zimmermann, 1990; Hirschmann et al., 2005). Figure 1.1 highlights the main processes leading to dehydration of a subducting plate and therefore triggering fluid flows at various depths.

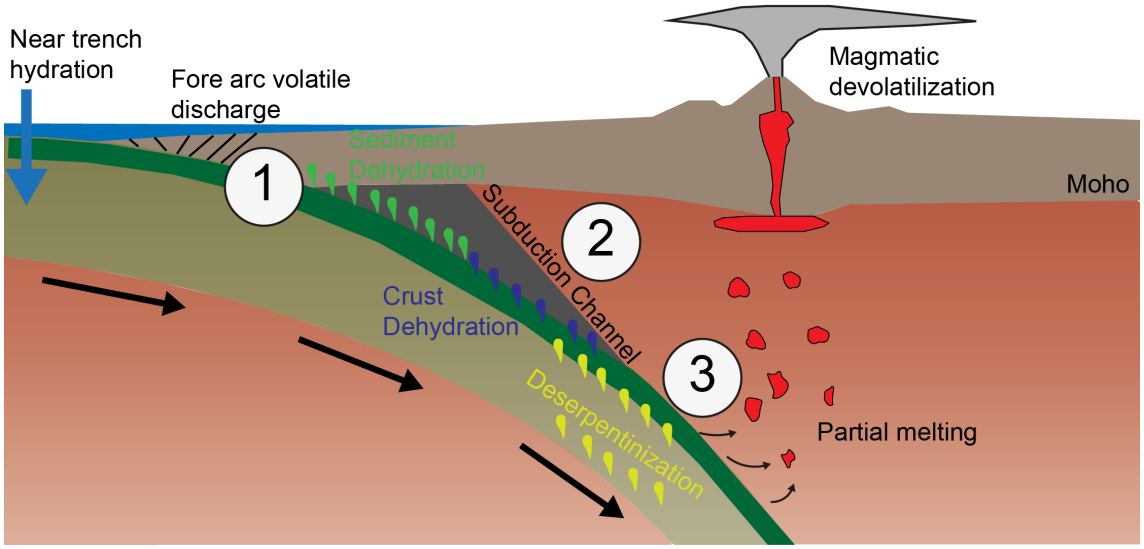

Figure 1.1: Schematic drawing of the deep earth water cycle based on Rüpke et al. (2004) highlighting major steps of dehydration within a subduction zone. (1) Shows the excess of fluids at shallow depth through compaction. (2) At intermediate depth water is released from oceanic crust and sediments. (3) Deep fluid release from the oceanic crust and through metamorphic dehydration reactions e.g. deserpentinization.

1.2 Fluid flow

In geosciences rocks consist of pore space and a solid matrix. If the pore space is connected, fluid flow and mass transfer can take place. In the Earth's crust rocks undergo compaction with increasing pressure at shallow depths of 4-11 km (Abers et al., 2017), leading to a decrease in the pore space to $\approx 1-4\%$ (Hyndman, 1988; Peacock et al., 2011). At depths between 25-240 km several metamorphic dehydration reactions take place, releasing chemically bound water and triggering partial melt, which maintain the porosity due to increasing fluid pressure and volume change (Peacock, 1990; Stern, 2002).

In general, flow of fluids and gases can be described by the well-known Navier-Stokes equations as follows (Landau and Lifshitz, 1987; Bear, 1988):

$$\frac{\partial \rho}{\partial t} + \nabla \cdot (\rho \mathbf{v}) = 0 \tag{1}$$

$$\rho \left[\frac{\partial v}{\partial t} + (\mathbf{v} \cdot \nabla) \mathbf{v} \right] = -\nabla P + \nabla \cdot \left[\eta \left(\nabla \mathbf{v} + \nabla \mathbf{v}^T \right) \right] + \nabla \left[\zeta \left(\nabla \cdot \mathbf{v} \right) \right] + \mathbf{F}, \tag{2}$$

where ρ is the density, t is the time, $\mathbf{v}$ is the velocity, P is the pressure, η is the shear viscosity coefficient, ζ is the volumetric viscosity coefficient and $\mathbf{F}$ represents gravitational body forces $\rho \mathbf{g}$. Assuming incompressibility of the fluid ($\nabla \cdot \mathbf{v} = 0$) yields:

$$\nabla \cdot \mathbf{v} = 0 \tag{3}$$

$$\rho \left[\frac{\partial v}{\partial t} + (\mathbf{v} \cdot \nabla) \mathbf{v} \right] = -\nabla P + \nabla \cdot \left[\eta \left(\nabla \mathbf{v} + \nabla \mathbf{v}^T \right) \right] + \mathbf{F}, \tag{4}$$

In porous media fluid flow can be characterized by the Reynolds number which relates inertial to viscous forces:

$$Re = \frac{\rho v L}{\eta}, \tag{5}$$

with L being the characteristic length of the domain. Due to the small pore size, flows in porous media commonly exhibit small Reynolds numbers and are thus considered to be laminar (Bear, 1988). Choosing the following characteristic variables

$$x' = \frac{x}{L}, \tag{6}$$

$$y' = \frac{y}{L}, \tag{7}$$

$$z' = \frac{z}{L}, \tag{8}$$

$$\nabla' = \frac{\nabla}{1/L}, \tag{9}$$

$$\mathbf{v}' = \frac{\mathbf{v}}{v}, \tag{10}$$

$$t' = \frac{t}{L/v}, \tag{11}$$

$$P' = \frac{P}{\eta v/L}, \tag{12}$$

one can non-dimensionalize eq. (3)+(4) to:

$$\nabla \cdot \mathbf{v} = 0 \tag{13}$$

$$\frac{Re}{St}\frac{\partial v'}{\partial t'} + Re\mathbf{v}' \cdot \nabla'\mathbf{v}' = -\nabla' P' + \nabla' \cdot \left[\eta\left(\nabla'\mathbf{v}' + \nabla\mathbf{v}'^{T}\right)\right] + \mathbf{F}, \tag{14}$$

Considering a steady flow (for which the Strouhal number $St = \frac{rL}{v}$, with r being the frequency of vortex shedding, is unity) and laminar flow conditions ($Re << 1$) inertial forces can be neglected, leading to the Stokes equations (dimensional form):

$$\nabla \cdot \mathbf{v} = 0 \tag{15}$$

$$-\nabla P + \nabla \cdot \left[\eta\left(\nabla\mathbf{v} + \nabla\mathbf{v}^{T}\right)\right] + \mathbf{F} = 0 \tag{16}$$

When viscosity can be assumed to be constant the Stokes equations further simplify to:

$$\nabla \cdot \mathbf{v} = 0 \tag{17}$$

$$-\nabla P + \eta\nabla^2\mathbf{v} + \mathbf{F} = 0 \tag{18}$$

Solving these equations provides solutions for velocity $\mathbf{u}$ and pressure P for a given pressure gradient across the computed domain.

To further take temperature into account the governing equation for conservation of energy is solved:

$$\rho C_p \frac{DT}{Dt} = \frac{\partial}{\partial x_i}\left(\kappa\frac{\partial T}{\partial x_i}\right) + H, \tag{19}$$

with ρ denoting the density, C_p the heat capacity, DT/Dt the total derivative of temperature T, κ the thermal conductivity and H the additional term for radiogenic heating.

An important parameter controlling fluid flow is permeability, describing the ability of fluids to pass through a porous material. Fluid flow and therefore permeability can be estimated on different scales, ranging from crustal (Fehn and Cathles, 1979; Norton and Taylor Jr, 1979) to pore scale (Brace, 1984). As permeability strongly

depends on microstructure (Mostaghimi et al., 2013; Keehm, 2003), an accurate determination on the microscale is necessary. A first empirical law on fluid flow through a bed of sand was derived experimentally by Henry Darcy (Darcy, 1856). In Darcy's law a permeability k is defined relating the flow rate Q to an applied pressure gradient $\Delta P/L$ as well as the fluid viscosity η:

$$k = -\frac{\eta L Q}{\Delta P A}, \tag{20}$$

where A is the cross-sectional area of the porous medium. Using the computed velocity field from eq. (3)+(4) in the z direction, the volume- averaged velocity component v_m is calculated (Osorno et al., 2015):

$$v_m = \frac{1}{V_f} \int_{V_f} |v_z| \, dv, \tag{21}$$

with V_f being the volume of the fluid phase. Making use of eq. (20) and $Q = v_m \cdot A$, the permeability k of the domain can be computed as

$$k = \frac{\eta v_m L}{\Delta P}. \tag{22}$$

In the literature various formulations relating permeability to several geometric properties of the void space exists. In 1933 a formulation for permeability, developed from dimensional considerations and verified experimentally was made by Fair and Hatch (1933) reading:

$$k = \frac{1}{\beta} \left[\frac{(1-\phi)^2}{\phi^3} \left(\frac{\gamma}{100} \sum_{(m)} \frac{P_m}{d_m} \right)^2 \right]^{-1}, \tag{23}$$

with β being a packing factor, found experimentally to be 5, ϕ being the porosity, γ being a sand shape factor, varying between 6 for spherical grains and 7.7 for angular ones, m being the number of sieves, P_m being the weight percentage of sand held in between adjacent sieves, and furthermore d_m being the geometric mean diameter of adjacent sieves.

Another formulation proposed by Krumbein and Monk (1943) using a purely empirical approach stated as follows:

$$k = C d^2, \tag{24}$$

where C is a dimensionless coefficient found to be 6.17×10^{-4} by Krumbein and Monk (1943) and d is the effective grain size.

An also often used formulation for permeability in porous media is the well-known Kozeny-Carman equation (Kozeny, 1927; Carman, 1937, 1956):

$$k = k_0 \frac{\phi^3}{S^2 \tau^2}, \tag{25}$$

where k_0 is the dimensionless Kozeny constant depending on the channel geometry (e.g. $k_0 = 0.5$ for cylindrical capillaries), S is the specific surface, defined as the total interfacial surface area of pores per unit bulk volume, and τ being the tortuosity. The tortuosity describes tortuous stream tubes filling up the entire void space and is defined as L_e/L, where L_e is the effective length of the tortuous stream tube and L is the length of the domain. Experimentally, Carman (1937) found that $\tau = \sqrt{2}$. This relation was derived assuming that the medium consists only of continuous, tortuous channels with constant cross-section (Carman, 1937; Bear, 1988).

However, in porous media tortuous pathways most likely do not obey these assumptions and therefore applying this equation to porous media remains challenging and in some cases fails for low porosities (Bernabe et al., 1982; Bourbie et al., 1992) or mixtures of different shapes and material sizes (Carman, 1937; Wyllie and Gregory, 1955) and small samples sizes. For this reason, the Kozeny-Carman equation has been modified and extended to account for various correlations between tortuosity, specific surface and porosity (Comiti and Renaud, 1989; Pech, 1984; Mavko and Nur, 1997; Mota et al., 2001; Pape et al., 2005).

For example, Comiti and Renaud (1989) proposed a tortuosity-porosity relation as follows:

$$\tau(\phi) = 1 - B ln(\phi), \tag{26}$$

where parameter B is determined experimentally for different kind of particles. Mota et al. (2001) found, by measuring the electrical conductivity of a medium filled with spherical particles, that tortuosity relates to porosity as denoted:

$$\tau(\phi) = \phi^{-0.4}. \tag{27}$$

Most of these relations used tortuosity as a fitting parameter and used materials having $\phi > 30\%$.

However, the determination of permeability and of microstructral parameters in three dimensions remains challenging. Especially for several geological processes, like magma migration, fluid flows play an important role on various scales. For example in subduction zones, fault zones and fractures are first order control mechanisms for fluid flow and drainage patterns (Carson and Screaton, 1998; Moore, 1989; Saffer and Tobin, 2011). Due to compaction of sediments with increasing

depth porosity drops from $\approx 50\%$ near the trench to $\lessapprox 10\%$ at 20-40 km landwards, which results in a decrease of permeability by 3-4 orders of magnitude (Saffer and McKiernan, 2005; Gamage and Screaton, 2006). This densification limits the ability of fluids to access permeable conduits and favors the development of stresses triggering earthquakes (Ellsworth, 2013; Terakawa et al., 2012). Furthermore certain processes like compaction and clogging by precipitation and dissolution of minerals may also feature the change of permeability with time (Bear, 2018).

References

Abers, G. A., van Keken, P. & Hacker, B. (2017). The cold and relatively dry nature of mantle forearcs in subduction zones. *Nature Geoscience*, *10*, 333–337. doi:10.1038/ngeo2922

Ahrens, T. J. (1989). Water storage in the mantle. *Nature*, *342*(6246), 122–123.

Bear, J. (1988). *Dynamics of fluids in porous media*. New York: Dover Publications Inc.

Bear, J. (2018). *Modeling Phenomena of Flow and Transport in Porous Media*. Cham: Springer. doi:10.1007/978-3-319-72826-1

Bercovici, D. & Karato, S.-i. (2003). Whole-mantle convection and the transition-zone water filter. *Nature*, *425*(6953), 39–44. doi:10.1038/nature01918

Bernabe, Y., Brace, W. & Evans, B. (1982). Permeability, porosity and pore geometry of hot-pressed calcite. *Mechanics of Materials*, *1*(3), 173–183. doi:https://doi.org/10.1016/0167-6636(82)90010-2

Bourbie, T., Coussy, O., Zinszner, B. & Junger, M. C. (1992). Acoustics of porous media. *The Journal of the Acoustical Society of America*, *91*(5), 3080–3080.

Brace, W. F. (1984). Permeability of crystalline rocks: New in situ measurements. *Journal of Geophysical Research: Solid Earth*, *89*(B6), 4327–4330. doi:10.1029/JB089iB06p04327

Carman, P. C. (1937). Fluid flow through granular beds. *Transactions, Institution of Chemical Engineers*, *15*, 150–166.

Carman, P. C. (1956). *Flow of gases through porous media*. New York: Academic Press.

Carson, B. & Screaton, E. J. (1998). Fluid flow in accretionary prisms: Evidence for focused, time-variable discharge. *Reviews of Geophysics*, *36*(3), 329–351. doi:10.1029/97RG03633

Clauser, C. (2014). *Einführung in die Geophysik*. Berlin, Heidelberg: Springer. doi:10.1007/978-3-662-46884-5

Comiti, J. & Renaud, M. (1989). A new model for determining mean structure parameters of fixed beds from pressure drop measurements: Application to

beds packed with parallelepipedal particles. *Chemical Engineering Science*, *44*(7), 1539–1545. doi:https://doi.org/10.1016/0009-2509(89)80031-4

Crowley, J. W., Gérault, M. & O'Connell, R. J. (2011). On the relative influence of heat and water transport on planetary dynamics. *Earth and Planetary Science Letters*, *310*(3-4), 380–388. doi:10.1016/j.epsl.2011.08.035

Darcy, H. P. G. (1856). *Les Fontaines publiques de la ville de Dijon: exposition et application des principes à suivre et des formules à employer dans les questions de distribution d'eau.* Paris: V. Dalamont.

Dasgupta, R. & Hirschmann, M. M. (2010). The deep carbon cycle and melting in Earth's interior. *Earth and Planetary Science Letters*, *298*(1), 1–13. doi:https://doi.org/10.1016/j.epsl.2010.06.039

Ellsworth, W. L. (2013). Injection-Induced Earthquakes. *Science*, *341*(6142), 1225942. doi:10.1126/science.1225942

Faccenda, M., Gerya, T. V. & Burlini, L. (2009). Deep slab hydration induced by bending-related variations in tectonic pressure. *Nature Geoscience*, *2*(11), 790–793. doi:10.1038/ngeo656

Fair, G. M. & Hatch, L. P. (1933). Fundamental Factors Governing the Streamline Flow of Water Through Sand. *Journal - AWWA*, *25*(11), 1551–1563. doi:10.1002/j.1551-8833.1933.tb18342.x

Fehn, U. & Cathles, L. M. (1979). Hydrothermal convection at slow-spreading mid-ocean ridges. *Tectonophysics*, *55*(1-2), 239–260. doi:10.1016/0040-1951(79)90343-3

Frost, D. J. & McCammon, C. A. (2008). The Redox State of Earth's Mantle. *Annual Review of Earth and Planetary Sciences*, *36*(1), 389–420. doi:10.1146/annurev.earth.36.031207.124322

Gamage, K. & Screaton, E. J. (2006). Characterization of excess pore pressures at the toe of the Nankai accretionary complex, Ocean Drilling Program sites 1173, 1174, and 808: Results of one-dimensional modeling. *Journal of Geophysical Research: Solid Earth*, *111*(B4). doi:10.1029/2004JB003572

Hacker, B. R. (2008). H_2O subduction beyond arcs. *Geochemistry, Geophysics, Geosystems*, *9*(3). doi:10.1029/2007GC001707

Hatakeyama, K., Katayama, I., Hirauchi, K.-i. & Michibayashi, K. (2017). Mantle hydration along outer-rise faults inferred from serpentinite permeability. *Scientific Reports*, *7*(1), 13870. doi:10.1038/s41598-017-14309-9

Hirschmann, M. M. (2018). Comparative deep Earth volatile cycles: The case for C recycling from exosphere/mantle fractionation of major (H_2O, C, N) volatiles and from H_2O/Ce, CO_2/Ba, and CO_2/Nb exosphere ratios. *Earth and Planetary Science Letters*, *502*, 262–273. doi:https://doi.org/10.1016/j.epsl.2018.08.023

Hirschmann, M. M., Aubaud, C. & Withers, A. C. (2005). Storage capacity of H_2O in nominally anhydrous minerals in the upper mantle. *Earth and Planetary Science Letters*, *236*(1-2), 167–181. doi:10.1016/j.epsl.2005.04.022

Hirschmann, M. M. & Dasgupta, R. (2009). The H/C ratios of Earth's near-surface and deep reservoirs, and consequences for deep Earth volatile cycles. *Chemical Geology*, *262*(1), 4–16. doi:https://doi.org/10.1016/j.chemgeo.2009.02.008

Hirth, G. & Kohlstedt, D. L. (1995). Experimental constraints on the dynamics of the partially molten upper mantle: 2. Deformation in the dislocation creep regime. *Journal of Geophysical Research: Solid Earth*, *100*(B8), 15441–15449. doi:10.1029/95JB01292

Hyndman, R. D. (1988). Dipping seismic reflectors, electrically conductive zones, and trapped water in the crust over a subducting plate. *Journal of Geophysical Research: Solid Earth*, *93*(B11), 13391–13405. doi:10.1029/JB093iB11p13391

Iwamori, H. (2004). Phase relations of peridotites under H_2O-saturated conditions and ability of subducting plates for transportation of H_2O. *Earth and Planetary Science Letters*, *227*(1-2), 57–71. doi:10.1016/j.epsl.2004.08.013

Jacobsen, S. D. & Smyth, J. R. (2013). Effect of water on the sound velocities of ringwoodite in the transition zone. In *Earth's deep water cycle* (pp. 131–145). American Geophysical Union (AGU). doi:10.1029/168GM10

Jambon, A. & Zimmermann, J. L. (1990). Water in oceanic basalts: evidence for dehydration of recycled crust. *Earth and Planetary Science Letters*, *101*(2-4), 323–331. doi:10.1016/0012-821X(90)90163-R

Keehm, Y. (2003). *Computational rock physics: Transport properties in porous media and applications* (Doctoral dissertation, Stanford University).

Korenaga, J. (2017). On the extent of mantle hydration caused by plate bending. *Earth and Planetary Science Letters*, *457*, 1–9. doi:10.1016/j.epsl.2016.10.011

Kozeny, J. (1927). Über kapillare Leitung des Wassers im Boden. *Royal Academy of Science, Vienna, Proc. Class I*, *136*, 271–306.

Krumbein, W. C. & Monk, G. D. (1943). Permeability as a Function of the Size Parameters of Unconsolidated Sand. *Transactions of the AIME*, *151*(01), 153–163.

Landau, L. D. & Lifshitz, E. M. (1987). *Course of theoretical physics. vol. 6: Fluid mechanics*. Pergamon Press.

Mavko, G. & Nur, A. (1997). The effect of a percolation threshold in the Kozeny-Carman relation. *Geophysics*, *62*(5), 1480–1482. doi:10.1190/1.1444251

McAdoo, D. C. & Martin, C. F. (1984). Seasat observations of lithospheric flexure seaward of trenches. *Journal of Geophysical Research: Solid Earth*, *89*(B5), 3201–3210. doi:10.1029/JB089iB05p03201

Mei, S. & Kohlstedt, D. L. (2000). Influence of water on plastic deformation of olivine aggregates: 1. Diffusion creep regime. *Journal of Geophysical Research: Solid Earth*, *105*(B9), 21457–21469. doi:10.1029/2000JB900179

Moore, J. C. (1989). Tectonics and hydrogeology of accretionary prisms: role of the décollement zone. *Journal of Structural Geology*, *11*(1-2), 95–106. doi:10.1016/0191-8141(89)90037-0

Morgan, W. J. (1968). Rises, trenches, great faults, and crustal blocks. *Journal of Geophysical Research*, *73*(6), 1959–1982. doi:10.1029/JB073i006p01959

Mostaghimi, P., Blunt, M. J. & Bijeljic, B. (2013). Computations of Absolute Permeability on Micro-CT Images. *Mathematical Geosciences*, *45*(1), 103–125. doi:10.1007/s11004-012-9431-4

Mota, M., Teixeira, J. A., Bowen, W. R. & Yelshin, A. (2001). Binary spherical particle mixed beds: porosity and permeability relationship measurement. *17*(1-4), 101–106.

Norton, D. & Taylor Jr, H. P. (1979). Quantitative Simulation of the Hydrothermal Systems of Crystallizing Magmas on the Basis of Transport Theory and Oxygen Isotope Data: An analysis of the Skaergaard intrusion. *Journal of Petrology*, *20*(3), 421–486. doi:10.1093/petrology/20.3.421

Ohtani, E. (2005). Water in the Mantle. *Elements*, *1*(1), 25–30. doi:10.2113/gselements.1.1.25

Osorno, M., Uribe, D., Ruiz, O. E. & Steeb, H. (2015). Finite difference calculations of permeability in large domains in a wide porosity range. *Archive of Applied Mechanics*, *85*(8), 1043–1054. doi:10.1007/s00419-015-1025-4

Pape, H., Clauser, C. & Iffland, J. (2005). Permeability prediction for reservoir sandstones and basement rocks based on fractal pore space geometry. In *Seg technical program expanded abstracts 1998* (pp. 1032–1035). Society of Exploration Geophysicists. doi:10.1190/1.1820060

Peacock, S. M. (1990). Fluid Processes in Subduction Zones. *Science*, *248*(4953), 329–337. doi:10.1126/science.248.4953.329

Peacock, S. M. (2001). Are the lower planes of double seismic zones caused by serpentine dehydration in subducting oceanic mantle? *Geology*, *29*(4), 299–302.

Peacock, S. M., Christensen, N. I., Bostock, M. G. & Audet, P. (2011). High pore pressures and porosity at 35 km depth in the Cascadia subduction zone. *Geology*, *39*(5), 471–474. doi:10.1130/G31649.1

Pech, D. (1984). *Etude de la perméabilité de lits compressibles constitués de copeaux de bois partiellement destructurés* (Doctoral dissertation, INP Grenoble).

Ranero, C. R., Morgan, J. P., McIntosh, K. & Reichert, C. (2003). Bending-related faulting and mantle serpentinization at the Middle America trench. *Nature*, *425*(6956), 367–373. doi:10.1038/nature01961

Ringwood, A. E. (1975). *Composition and Petrology of the Earth's Mantle*. London, New York & Sydney: McGraw-Hill.

Rüpke, L. H., Morgan, J. P., Hort, M. & Connolly, J. A. D. (2004). Serpentine and the subduction zone water cycle. *Earth and Planetary Science Letters*, *223*(1-2), 17–34. doi:10.1016/j.epsl.2004.04.018

Saffer, D. M. & McKiernan, A. W. (2005). Permeability of underthrust sediments at the Costa Rican subduction zone: Scale dependence and implications for dewatering. *Geophysical Research Letters*, *32*(2). doi:10.1029/2004GL021388

Saffer, D. M. & Tobin, H. J. (2011). Hydrogeology and Mechanics of Subduction Zone Forearcs: Fluid Flow and Pore Pressure. *Annual Review of Earth and Planetary Sciences*, *39*, 157–186. doi:10.1146/annurev-earth-040610-133408

Schmidt, M. W. & Poli, S. (1998). Experimentally based water budgets for dehydrating slabs and consequences for arc magma generation. *Earth and Planetary Science Letters*, *163*(1-4), 361–379.

Smyth, J. R. (1987). $\beta - Mg_2SiO_4$: A potential host for water in the mantle? *American Mineralogist*, *72*(11-12), 1051–1055.

Smyth, J. R. & Jacobsen, S. D. (2013). Nominally anhydrous minerals and earth's deep water cycle. In *Earth's deep water cycle* (pp. 1–11). American Geophysical Union (AGU). doi:10.1029/168GM02

Stern, R. J. (2002). Subduction zones. *Reviews of Geophysics*, *40*(4), 3-1-3-38. doi:10.1029/2001RG000108

Syracuse, E. M., van Keken, P. E. & Abers, G. A. (2010). The global range of subduction zone thermal models. *Physics of the Earth and Planetary Interiors*, *183*(1-2), 73–90. doi:10.1016/j.pepi.2010.02.004

Terakawa, T., Miller, S. A. & Deichmann, N. (2012). High fluid pressure and triggered earthquakes in the enhanced geothermal system in Basel, Switzerland. *Journal of Geophysical Research: Solid Earth*, *117*(B7). doi:10.1029/2011JB008980

van Keken, P. E., Currie, C., King, S. D., Behn, M. D., Cagnioncle, A., He, J., ... Spiegelman, M. et al. (2008). A community benchmark for subduction zone modeling. *Physics of the Earth and Planetary Interiors*, *171*(1), 187–197. doi:10.1016/j.pepi.2008.04.015

van Keken, P. E., Hacker, B. R., Syracuse, E. M. & Abers, G. A. (2011). Subduction factory: 4. Depth-dependent flux of H_2O from subducting slabs worldwide. *Journal of Geophysical Research: Solid Earth*, *116*(B1). doi:10.1029/2010JB007922

van Keken, P. E., Kiefer, B. & Peacock, S. M. (2002). High-resolution models of subduction zones: Implications for mineral dehydration reactions and the transport of water into the deep mantle. *Geochemistry, Geophysics, Geosystems*, *3*(10), 1 of 20-20 of 20. doi:10.1029/2001GC000256

Watts, A. B., Bodine, J. H. & Steckler, M. S. (1980). Observations of flexure and the state of stress in the oceanic lithosphere. *Journal of Geophysical Research: Solid Earth*, *85*(B11), 6369–6376. doi:10.1029/JB085iB11p06369

Wegener, A. (1912). Die Entstehung der Kontinente. *Geologische Rundschau*, *3*(4), 276–292. doi:10.1007/BF02202896

Wilson, C. R., Spiegelman, M., van Keken, P. E. & Hacker, B. R. (2014). Fluid flow in subduction zones: The role of solid rheology and compaction pressure. *Earth and Planetary Science Letters*, *401*, 261–274.

Wyllie, M. R. J. & Gregory, A. R. (1955). Fluid flow through unconsolidated porous aggregates. *Industrial & Engineering Chemistry*, *47*(7), 1379–1388. doi:10.1021/ie50547a037

Chapter 2 | Methods

2.1 Experimental permeability measurement

To model fluid flow in a specific tectonic or lithological setting, permeability is one of the most difficult parameters to estimate as it can vary by more than 10 orders of magnitude (Freeze and Cherry, 1979). Due to enhanced flow in mesoscopic features like fractures, laboratory measurements of permeabilities can differ from in situ permeabilities (Brace, 1980). Furthermore variations in temperature and pressure, which are related to metamorphic processes, may influence the permeability significantly. For this reason, several different experimental techniques have been developed over the decades, trying to estimate permeability accurately (Ferland et al., 1996; Takeuchi et al., 2008; David et al., 1994; Brace, 1984). Within the scope of this work the measurement method of Takeuchi et al. (2008) is described in more detail.

Permeameter: The permeameter (Fig. 2.1) is composed of an air compressor, a pressure regulator (RP1000-8-04, CKD Co.; Precision $\pm 0.1\,\%$), an analog pressure gauge, a digital pressure manometer (testo526-s, Testo Inc.; Precision $\pm 0.05\,\%$), a sample holder and a flow meter (Alicat, M-10SCCM; Precision $\pm 0.6\%$). The gas-flow line is connected from the bottom of the sample-holder (high-pressure side) to the top of the sample holder (low-pressure side) via the digital manometer. All parts are connected by pressure-proof tubes (5 mm in inner diameter). The measurement is performed under steady-state gas flow from the high-pressure side through the samples to the low-pressure side, at which the digital flow meter is attached.

Sample preparation: Before preparing the samples for permeability measurements, they are digitized using micro Computed Tomographic scans (micro-CT) performed at Tohoku University (ScanXmate-D180RSS270) with a resolution $\approx 6 - 10\,\mu$m, according to the method of Okumura and Sasaki (2014). To perform air flow measurements some preparations of the samples are necessary. In a first step, samples are wrapped by a commercially available high-viscous water-proof resin to prevent the intrusion of the less-viscous resin (Technovit 4071, Heraeus Kulzer GmbH & Co. or Presin, Nichika Inc.) into the pore space. Afterwards the upper and lower end surfaces of the embedded samples were exposed by grinding and polishing. In particular, the flatness of the resin part at both end surfaces is of crucial importance to prevent any leakage of the working gas at the contact area between the O-rings and the end surface of the samples, which are sandwiched between the acrylic plates.

Sample measurement: The air flow measurements take place at room temperature. During the measurement the resulting flow is evaluated at several pressure gradients. This procedure is performed to confirm both laminar flow conditions, represented

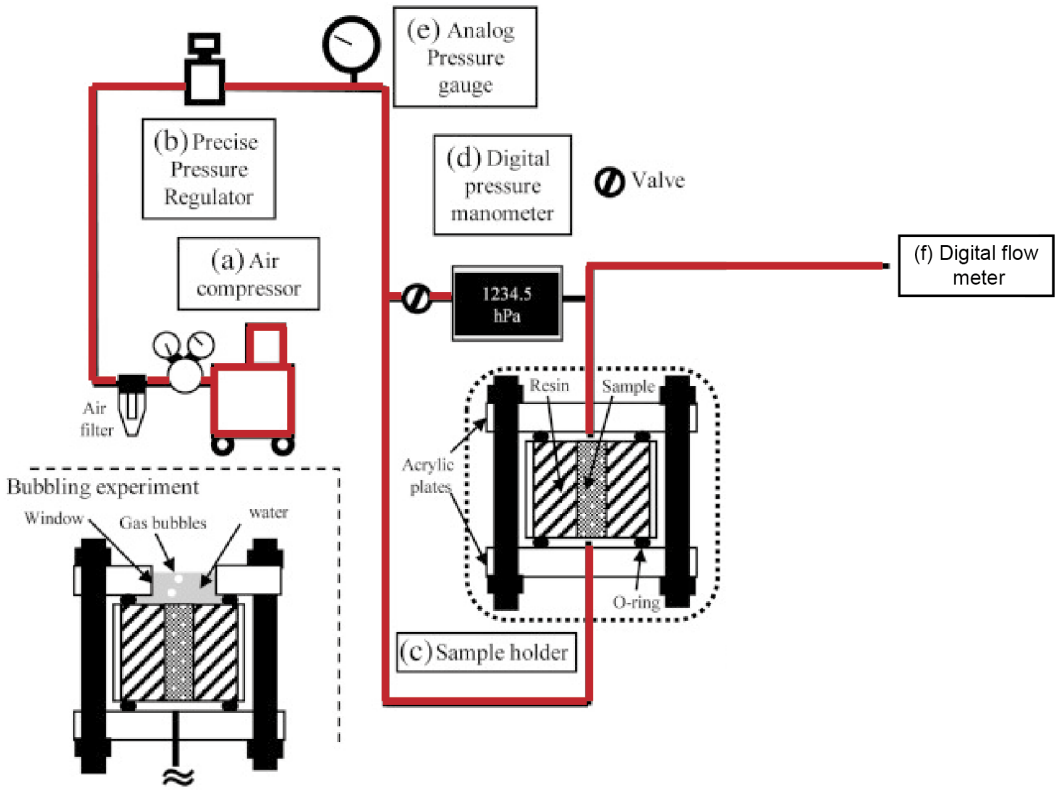

Figure 2.1: Schematic configuration of the experimental assembly used to measure permeability (modified from Takeuchi et al. (2008)).

by a linear increase of the flow rate with increasing pressure, and reproducibility of the measurements.

Determination of permeability: Darcy's law is applied to the measurement results (eq. (20)) to determine permeability of the samples. Recently, several volcanology studies showed that at high flow rates the flow of the working gas is not always laminar and therefore with increasing flow rate, energy is lost through inertia (Rust and Cashman, 2004; Wright et al., 2006, 2007). Therefore, before using Darcy's law the effect of compressibility and inertia of the working gas need to be considered. For this reason, a modified version of Darcy's equation, the Forchheimer equation (Forchheimer, 1901) is used, which incorporates the nonlinear relationship between gas volume flux to a modified pressure gradient reading as:

$$\frac{P_2^2 - P_1^2}{2P_0H} = \frac{\eta}{k_1}\nu_0 + \frac{\rho}{k_2}\nu_0^2, \tag{28}$$

P_2 and P_1 denote the pressures at the inlet and outlet, P_0 the actual pressure at the point of measurement, H the distance between the inlet and outlet, ν_0 the gas volume flux which is calculated from the flow rate divided by cross-sectional area of the sample, k_1 the Darcian and k_2 the non-Darcian permeability. Density ρ and

viscosity η of air are assumed to be constant. To only compute the permeability considering compressibility of the working gas, a modified version of Darcy's law is used (Takeuchi et al., 2008), reading as follows :

$$\frac{P_2^2 - P_1^2}{2P_0H} = \frac{\eta\nu_0}{k}, \tag{29}$$

The left-hand side of eq. (29) represents the modified pressure gradient that includes the compressibility of the working gas. Within the scope of the study we checked for both inertia and compressibility, which were found to be negligible as the determined values for permeability differ by less than 10% from the values obtained using Darcy's law.

2.2 Digital Rock Physics

Permeability can be determined experimentally through a wide range of different techniques. Typical limitations for experimental permeability measurements on pore scale are: (i) change of the sample's microstructure and therefore its physical properties through cracking and self-filtration (Zeinijahromi et al., 2016; Dikinya et al., 2008), (ii) pressure changes due to the influence of wall effects (Ferland et al., 1996), (iii) difficulties to measure irregular grain shapes and small grain sizes of the porous medium (Cui et al., 2009; Gerke et al., 2015) and finally (iv) to measure small sample sizes. Moreover laboratory measurements do not provide information on the pathways and the microstructure, which have a crucial influence on the permeability.

At this point Digital Rock Physics (DRP) can help to complement laboratory experiments and enhance the understanding of the sample microstructure (Dvorkin et al., 2003). In detail DRP, which can be described as an "image-to-compute" approach (Fig. 2.2), uses numerical simulations to investigate transport and elastic properties at the pore scale level (Knackstedt et al., 2009; Andrä et al., 2013b; Saxena et al., 2017). The images of the pore space are obtained using different techniques e.g. X-ray Computed Tomography (micro-CT; Saxena et al. (2017) and Andrä et al. (2013a)) and Nuclear Magnetic Resonance (NMR; Arns et al. (2001) and Arns (2004)). In a next step these images are used to construct a three dimensional representation of the pore space. To compute transport and elastic properties different numerical techniques including Lattice-Boltzmann method (LBM) (Bosl et al., 1998; Guo and Zhao, 2002; Pan et al., 2004), Finite Differences method (FDM) (Gerke et al., 2018; Manwart et al., 2002; Shabro et al., 2014) and Finite Elements Methods (FEM) (Akanji and Matthai, 2010; Bird et al., 2014; Garcia et al., 2009) are used.

In recent years the approach of DRP has proved to significantly complement the physical laboratory as a non-destructive method to rigorously predict flow properties (e.g., tortuosity, relative/absolute permeability), elastic properties (e.g., formation factor, elastic moduli) and electrical properties (e.g., electric conductivity/resistivity). Recent studies also provided computations of multiphase flow, which is of crucial importance for some geological processes (e.g., magma migration) and furthermore for industrial applications including enhanced oil recovery (Koroteev et al., 2014; Berg et al., 2013; Berg et al., 2014; Liu et al., 2007). With the ascent of new technologies and increasing computational resources, DRP will be able to compute elastic, flow and electrical properties of larger, highly resolved images in the near future; thus, improving the precision and understanding of microstructural parameters.

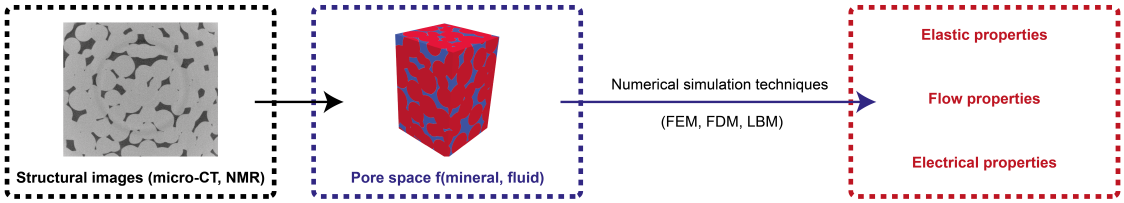

Figure 2.2: Schematic sketch of the Digital Rock Physics workframe.

2.3 Numerical techniques

Physical laws are often expressed in terms of Partial Differential Equations (PDEs). Depending on the geometry and problem, a vast majority of the physical problems can not be solved analytically. Instead, the equations can be solved numerically using different discretization methods. Several of these discretizations methods can be used, but within the scope of this thesis only the Finite Difference method (FDM) and the Finite Element method (FEM) are described briefly in the following section.

2.3.1 Finite Difference Method

The Finite Difference method (FDM) is a numerical method for solving differential equations and is used in nearly all natural science fields. These equations are approximated by replacing the derivative with differential quotients. For the sake of simplicity a one dimensional case is considered, where a derivative of a function u at a point x states as follows:

$$\frac{\partial u}{\partial x} \approx \frac{u(x + \Delta x) - u(x)}{\Delta x}. \tag{30}$$

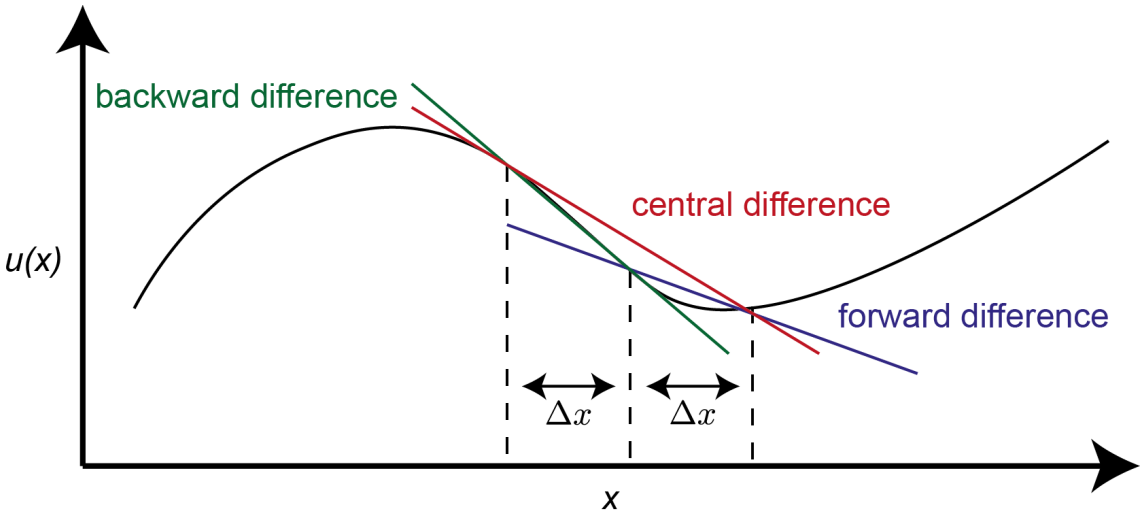

Figure 2.3: A sketch showing the different types of finite difference schemes.

For a sufficiently small Δx the right-hand side represents a good approximation of the derivative. Apart from eq. (30), which represents a first order forward finite difference, two additional forms of the approximations can be used, namely backwards and central finite difference as follows (Fig. 2.3):

$$\frac{\partial u}{\partial x} \approx \frac{u(x) - u(x - \Delta x)}{\Delta x}, \tag{31}$$

$$\frac{\partial u}{\partial x} \approx \frac{u(x + \Delta x) - u(x - \Delta x)}{2\Delta x}. \tag{32}$$

The accuracy of these approximations differs in terms of the local truncation errors $O(\Delta x)$, defined as the misfit between the exact value and the numerical approximation. The Taylor-Series expansion for $u(x + \Delta x)$ states that:

$$u(x + \Delta x) = u(x) + \Delta x \frac{\partial u(x)}{\partial x} + \frac{\Delta x^2}{2} \frac{\partial^2 u(x)}{\partial x^2} + \frac{\Delta x^3}{6} \frac{\partial^3 u(x)}{\partial x^3} + O(\Delta x^4). \tag{33}$$

Solving for $\frac{\partial u(x)}{\partial x}$ leads to:

$$\frac{u(x + \Delta x) - u(x)}{\Delta x} = \frac{\partial u(x)}{\partial x} + O(\Delta x), \tag{34}$$

with $\frac{u(x+\Delta x)-u(x)}{\Delta x}$ being the approximation for forward finite differences, $\frac{\partial u(x)}{\partial x}$ being the exact quantity of interest and $O(\Delta x)$ the truncation error. For $u(x - \Delta x)$ the Taylor-Series expansion reads as:

$$u(x - \Delta x) = u(x) - \Delta x \frac{\partial u(x)}{\partial x} + \frac{\Delta x^2}{2} \frac{\partial^2 u(x)}{\partial x^2} - \frac{\Delta x^3}{6} \frac{\partial^3 u(x)}{\partial x^3} + O(\Delta x^4) \tag{35}$$

Similarly, we obtain

$$\frac{u(x) - u(x - \Delta x)}{\Delta x} = \frac{\partial u(x)}{\partial x} + O(\Delta x), \tag{36}$$

with $\frac{u(x)-u(x+\Delta x)}{\Delta x}$ being the approximation for backward finite difference, $\frac{\partial u(x)}{\partial x}$ being the exact quantity of interest and $O(\Delta x)$ the truncation error.

A higher order approximation of $\partial u(x)/\partial x$ is obtained by substracting eq. (35) from eq. (33). The results is represented as:

$$u(x + \Delta x) - u(x - \Delta x) = 2\Delta x \frac{\partial u(x)}{\partial x} + \frac{\Delta x^3}{3} \frac{\partial^3 u(x)}{\partial x^3} + O(\Delta x^5). \tag{37}$$

Dividing by $2\Delta x$ leads to:

$$\frac{u(x + \Delta x) - u(x - \Delta x)}{2\Delta x} = \frac{\partial u(x)}{\partial x} + O(\Delta x^2), \tag{38}$$

where $\frac{u(x+\Delta x)-u(x-\Delta x)}{2\Delta x}$ is the central finite difference approximation, $\frac{\partial u(x)}{\partial x}$ is the exact quantity of interest and $O(\Delta x^2)$ is the truncation error. In contrast to eq. (33) and eq. (35), representing forward and backward finite differences, the truncation error for central finite differences (eq. (38)) is smaller for small Δx. Therefore a central finite difference scheme is more accurate than forward and backward finite difference schemes.

Accordingly, a second order partial differential equation therefore reads as follows:

$$\frac{\partial^2 u}{\partial x^2} \approx \frac{u(x + \Delta x) - 2u(x) + u(x - \Delta x)}{\Delta x^2} \tag{39}$$

In Finite Differences the discretized Stokes equations (assuming constant viscosity and density; eqs. (17) and (18)) in x, y, z direction denote as:

$$\frac{\partial v_x}{\partial x} + \frac{\partial v_y}{\partial y} + \frac{\partial v_z}{\partial z} = 0, \tag{40}$$

$$\eta \left(\frac{\partial^2 v_x}{\partial x^2} + \frac{\partial^2 v_x}{\partial y^2} + \frac{\partial^2 v_x}{\partial z^2} \right) - \frac{\partial P}{\partial x} + \rho g_x = 0, \tag{41}$$

$$\eta \left(\frac{\partial^2 v_y}{\partial x^2} + \frac{\partial^2 v_y}{\partial y^2} + \frac{\partial^2 v_y}{\partial z^2} \right) - \frac{\partial P}{\partial y} + \rho g_y = 0, \tag{42}$$

$$\eta \left(\frac{\partial^2 v_z}{\partial x^2} + \frac{\partial^2 v_z}{\partial y^2} + \frac{\partial^2 v_z}{\partial z^2} \right) - \frac{\partial P}{\partial z} + \rho g_z = 0. \tag{43}$$

2.3.2 Finite Element Method

The Finite Element method (FEM) is a numerical technique to obtain approximate solutions of partial differential equations and is widely used in scientific and engineering applications (e.g. Rieg et al., 2019). Instead of approximating the partial differential equations directly as with Finite Differences (section 2.3.1), FEM provides approximations of differential equations using an integral of the equation over the model domain, represented by an assembly of *finite elements*. The solution of a partial differential equation is approximated by a simple polynomial function on each element. In a next step, the polynomial functions are pieced together and the integral is evaluated as a sum of contributions from each *finite element*.

Before applying FEM to a partial differential equation it is necessary to transform the equation into a more suitable, so-called weak formulation. Initially the weak formulation was introduced to investigate the behaviour of the solution of partial differential equations. For this reason the Stokes equations (eqs. (17) and (18)) are multiplied with so-called test functions q and w, leading to:

$$(\nabla \cdot \mathbf{v})q = 0, \tag{44}$$

$$-\eta\Delta\mathbf{v} \cdot w + \nabla P \cdot w = \mathbf{f} \cdot w. \tag{45}$$

By integrating over the domain Ω we get

$$\int_\Omega (\nabla \cdot \mathbf{v})q \,\mathrm{d}x = 0, \tag{46}$$

$$\int_\Omega -\eta\Delta\mathbf{v} \cdot w \,\mathrm{d}x + \int_\Omega \nabla P \cdot w \,\mathrm{d}x = \int_\Omega \mathbf{f} \cdot w \,\mathrm{d}x. \tag{47}$$

Using integration by parts and the Gauss divergence theorem yields the weak formulation of the Stokes equation:

$$\int_\Omega (\nabla \cdot \mathbf{v})q \,\mathrm{d}x = 0, \tag{48}$$

$$\int_\Omega \eta\nabla\mathbf{v} : \nabla w \,\mathrm{d}x - \int_\Omega (\nabla \cdot w)P \,\mathrm{d}x = \int_\Omega \mathbf{f} \cdot w \,\mathrm{d}x, \tag{49}$$

which is then usually numerically discretized in two dimensions by (i) meshing the domain with quadrilateral or triangular elements and (ii) approximating the integrals with appropriate sums e.g. using Gaussian quadrature:

$$\int_{-1}^{1} f(\xi_n)\, d\xi \approx \sum_{n=1}^{nip} f(\xi_n) w_n, \tag{50}$$

where ξ are the local coordinates and w_i the weights for each integration point and nip the total number of intergration points per element. The resulting system of equations is then solved iteratively using e.g. Powell-Hestenes iterations (see section 2.3.5)

2.3.3 Marker-and-Cell method

In order to describe motion in an appropriate way, two principal and distinct approaches can be used: the *Lagrangian* and *Eulerian formulations*. Within the scope of this thesis both methods - Finite Difference and Finite Element - are used.

In the *Lagrangian* description each node of the computational mesh follows the particle motion resulting in deformation of the grid, often used in structural geology and solid geomechanics (Ismail-Zadeh and Tackley, 2010). A difficulty in the application of this description is the loss of accuracy due to large strains within the computational mesh and therefore in most cases it is necessary to use remeshing techniques.

In the *Eulerian* description, mainly used in fluid mechanics and geodynamics, the computational mesh is fixed and the continuum moves and deforms with respect to the computational grid (Gerya, 2010). Therefore using the *Eulerian formulation* remeshing is not required, but this method struggles to follow free surfaces and material interfaces.

Whereas in Finite Differences, due to the fixed grid, only the Eulerian description can be used, Finite Elements are capable of using both approaches. However, when using the Lagrangian approach, remeshing is necessary due to distorted elements, introducing numerical diffusion. To minimize numerical diffusion and track material properties, a so-called *Marker-and-Cell-method (MAC)* can be used. An often used approach is to combine the use of Lagrangian advecting points (particles or markers) with an fixed Eulerian grid (Christensen, 1982; Woidt, 1978). In this method, properties are initially distributed on Lagrangian markers, which are advected through the domain according to a computed velocity field. In the following, the advected markers, carrying material properties like density and viscosity, are interpolated onto the Eulerian grid by using, for example, weighted-distance averaging. In order to move Lagrangian points, different advection schemes ranging from simple first-order advection scheme to higher order *Runge-Kutta advection schemes* can be used.

2.3.4 LaMEM

In the present work we will use the Finite Difference code LaMEM (Lithosphere and Mantle Evolution Model (Kaus et al., 2016)) solving the Stokes equations as stated above (see section 2.3.1). To discretize the governing equations (eqs. (17) and (18)), LaMEM employs a staggered grid finite difference scheme (Harlow and Welch, 1965). Within the staggered grid pressures are defined in the middle of the staggered grid cell, whereas velocities are defined on cell faces (Fig. 2.4).

The discretized system is then solved using an iterative multigrid scheme to obtain values for velocities $\mathbf{v}$ and pressure P. To this end, we employ a V-cycle geometric multiplicative multigrid solver (Fedorenko, 1964; Wesseling, 1995) which is part of the PETSc library (Balay et al., 2010). As LaMEM is written to simulate large-scale deformation of the Earth's lithosphere and mantle, it is therefore also able to handle complex rheologies, including dislocation, diffusion and Peierls creep and is furthermore highly scalable for the use on high performance parallel computers.

In this thesis LaMEM is used in Chapters 4 and 5. In Chapter 4 LaMEM, employing the technique of stencil rescaling, is benchmarked against several numerical settings, whereas in Chapter 5 it is used to compute fluid flow and permeability of granular glass bead samples. As the modelled domains of porous media samples are three-dimensional with sizes of 512^3 voxels, the ability of LaMEM to compute fluid flow in parallel on large computational clusters is necessary.

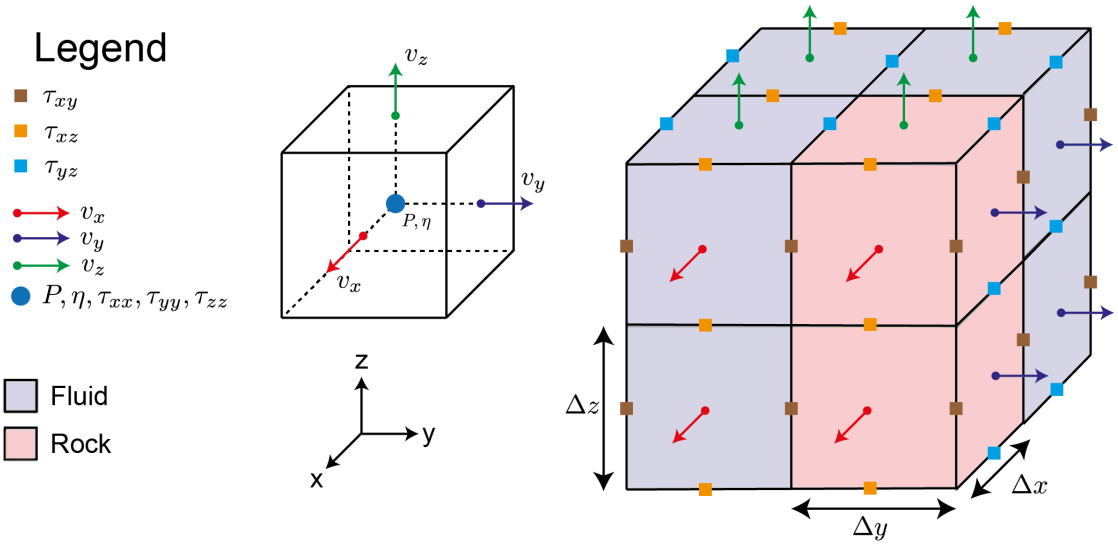

Figure 2.4: Staggered grid and location of computed variables.

2.3.5 MVEP2

In this thesis the 2D Lagrangian thermo-mechanical Finite Element code MVEP2, developed at the University of Mainz, is used to simulate fluid flow within a subduction zone (Chapter 6). MVEP2 uses an efficient matrix assembly method developed by Dabrowski et al. (2008) combined with a marker-and-cell approach to track material parameters. Several geodynamic processes can be simulated and phase transitions, sedimentation and erosion as well as melt extraction are included. MVEP2 solves eqs. (17) and (18) using a finite element discretization resulting in a discrete saddle point problem $Ax = b$:

$$\begin{pmatrix} K & G \\ G^T & -\Lambda M \end{pmatrix} \begin{pmatrix} \mathbf{v} \\ P \end{pmatrix} = \begin{pmatrix} \rho \mathbf{g} \\ 0 \end{pmatrix}, \tag{51}$$

where K is the discretized Laplace operator, G is the discretized gradient operator, Λ is the penalty factor and M is the mass matrix. Within the calculation the second row of eq. (51) is solved for P. In the following, the solution for P is then substituted into the first row of eq. (51). This system of equation can then be solved using Powell-Hestenes iterations (Cuvelier et al., 1986).

References

Akanji, L. T. & Matthai, S. K. (2010). Finite element-based characterization of pore-scale geometry and its impact on fluid flow. *Transport in Porous Media*, *81*(2), 241–259. doi:10.1007/s11242-009-9400-7

Andrä, H., Combaret, N., Dvorkin, J., Glatt, E., Han, J., Kabel, M., ... Zhan, X. (2013a). Digital rock physics benchmarks—Part I: Imaging and segmentation. *Computers & Geosciences*, *50*, 25–32. doi:https://doi.org/10.1016/j.cageo.2012.09.005

Andrä, H., Combaret, N., Dvorkin, J., Glatt, E., Han, J., Kabel, M., ... Zhan, X. (2013b). Digital rock physics benchmarks—Part II: Computing effective properties. *Computers & Geosciences*, *50*, 33–43. doi:https://doi.org/10.1016/j.cageo.2012.09.008

Arns, C. H. (2004). A comparison of pore size distributions derived by NMR and X-ray-CT techniques. *Physica A: Statistical Mechanics and its Applications*, *339*(1-2), 159–165. doi:10.1016/j.physa.2004.03.033

Arns, C. H., Knackstedt, M. A., Pinczewski, M. V. & Lindquist, W. (2001). Accurate estimation of transport properties from microtomographic images. *Geophysical Research Letters*, *28*(17), 3361–3364. doi:10.1029/2001GL012987

Balay, S., Buschelman, K., Eijkhout, V., Gropp, W., Kaushik, D., Knepley, M., ... Zhang, H. (2010). PETSc Users Manual. *ReVision*, *2*, 1–211.

Berg, S., Armstrong, R., Ott, H., Georgiadis, A., Klapp, S. A., Schwing, A., ... Stampanoni, M. (2014). Multiphase Flow in Porous Rock Imaged Under Dynamic Flow Conditions with Fast X-Ray Computed Microtomography. *Petrophysics*, *55*(4), 304–312.

Berg, S., Ott, H., Klapp, S. A., Schwing, A., Neiteler, R., Brussee, N., ... Stampanoni, M. (2013). Real-time 3D imaging of Haines jumps in porous media flow. *Proceedings of the National Academy of Sciences of the United States of America*, *110*(10), 3755–3759. doi:10.1073/pnas.1221373110

Bird, M., Butler, S. L., Hawkes, C. & Kotzer, T. (2014). Numerical modeling of fluid and electrical currents through geometries based on synchrotron X-ray

tomographic images of reservoir rocks using Avizo and COMSOL. *Computers & Geosciences*, *73*, 6–16. doi:10.1016/j.cageo.2014.08.009

Bosl, W. J., Dvorkin, J. & Nur, A. (1998). A study of porosity and permeability using a lattice Boltzmann simulation. *Geophysical Research Letters*, *25*(9), 1475–1478. doi:10.1029/98GL00859

Brace, W. F. (1980). Permeability of crystalline and argillaceous rocks. *International Journal of Rock Mechanics and Mining Sciences & Geomechanics Abstracts*, *17*(5), 241–251. doi:10.1016/0148-9062(80)90807-4

Brace, W. F. (1984). Permeability of crystalline rocks: New in situ measurements. *Journal of Geophysical Research: Solid Earth*, *89*(B6), 4327–4330. doi:10.1029/JB089iB06p04327

Christensen, U. (1982). Phase boundaries in finite amplitude mantle convection. *Geophysical Journal International*, *68*(2), 487–497. doi:10.1111/j.1365-246X.1982.tb04911.x

Cui, X., Bustin, A. & Bustin, R. M. (2009). Measurements of gas permeability and diffusivity of tight reservoir rocks: different approaches and their applications. *Geofluids*, *9*(3), 208–223. doi:10.1111/j.1468-8123.2009.00244.x

Cuvelier, C., Segal, A. & van Steenhoven, A. (1986). *Finite Element Methods and Navier-Stokes Equations*. Mathematics and its applications. Dordrecht: Reidel.

Dabrowski, M., Krotkiewski, M. & Schmid, D. W. (2008). MILAMIN: MATLAB-based finite element method solver for large problems. *Geochemistry, Geophysics, Geosystems*, *9*(4). doi:10.1029/2007GC001719

David, C., Wong, T.-F., Zhu, W. & Zhang, J. (1994). Laboratory measurement of compaction-induced permeability change in porous rocks: Implications for the generation and maintenance of pore pressure excess in the crust. *Pure and Applied Geophysics*, *143*(1-3), 425–456. doi:10.1007/BF00874337

Dikinya, O., Hinz, C. & Aylmore, G. (2008). Decrease in hydraulic conductivity and particle release associated with self-filtration in saturated soil columns. *Geoderma*, *146*(1-2), 192–200. doi:10.1016/j.geoderma.2008.05.014

Dvorkin, J., Walls, J., Tutuncu, A., Prasad, M., Nur, A. & Mese, A. (2003). Rock Property Determination Using Digital Rock Physics. *SEG Technical Program Expanded Abstracts 2003*, 1660–1663. doi:10.1190/1.1817624

Fedorenko, R. P. (1964). The speed of convergence of one iterative process. *Journal of Computational Mathematics and Mathematical Physics*, *4*, 227–35.

Ferland, P., Guittard, D. & Trochu, F. (1996). Concurrent methods for permeability measurement in resin transfer molding. *Polymer Composites*, *17*(1), 149–158. doi:10.1002/pc.10600

Forchheimer, P. (1901). Wasserbewegung durch Boden. *Düsseldorf: Zeitschrift des Vereins deutscher Ingenieure*, *45*, 1782–1788.

Freeze, R. A. & Cherry, J. A. (1979). *Groundwater*. London: Prentice-Hall.

Garcia, X., Akanji, L. T., Blunt, M. J., Matthai, S. K. & Latham, J. P. (2009). Numerical study of the effects of particle shape and polydispersity on permeability. *Physical Review E*, *80*(2), 021304. doi:10.1103/PhysRevE.80.021304

Gerke, K. M., Sidle, R. C. & Mallants, D. (2015). Preferential flow mechanisms identified from staining experiments in forested hillslopes. *Hydrological Processes*, *29*(21), 4562–4578. doi:10.1002/hyp.10468

Gerke, K. M., Vasilyev, R. V., Khirevich, S., Collins, D., Karsanina, M. V., Sizonenko, T. O., ... Mallants, D. (2018). Finite-difference method Stokes solver (FDMSS) for 3D pore geometries: Software development, validation and case studies. *Computers & Geosciences*, *114*, 41–58. doi:10.1016/j.cageo.2018.01.005

Gerya, T. (2010). *Introduction to Numerical Geodynamic Modelling*. Cambridge: Cambridge University Press. doi:10.1017/S0016756811000604

Guo, Z. & Zhao, T. S. (2002). Lattice Boltzmann model for incompressible flows through porous media. *Physical Review E*, *66*(3), 036304. doi:10.1103/PhysRevE.66.036304

Harlow, F. H. & Welch, J. E. (1965). Numerical Calculation of Time-Dependent Viscous Incompressible Flow of Fluid with Free Surface. *The Physics of Fluids*, *8*(12), 2182–2189. doi:10.1063/1.1761178

Ismail-Zadeh, A. & Tackley, P. (2010). *Computational Methods for Geodynamics*. Cambridge: Cambridge University Press. doi:10.1017/CBO9780511780820

Kaus, B. J. P., Popov, A. A., Baumann, T. S., Püsök, A. E., Bauville, A., Fernandez, N. & Collignon, M. (2016). Forward and Inverse Modelling of Lithospheric Deformation on Geological Timescales. *NIC Series*, *48*, 299–307.

Knackstedt, M. A., Latham, S., Madadi, M., Sheppard, A., Varslot, T. & Arns, C. (2009). Digital rock physics: 3D imaging of core material and correlations to acoustic and flow properties. *The Leading Edge*, *28*(1), 28–33. doi:10.1190/1.3064143

Koroteev, D., Dinariev, O., Evseev, N., Klemin, D., Nadeev, A., Safonov, S., ... de Jong, H. (2014). Direct Hydrodynamic Simulation of Multiphase Flow in Porous Rock. *Petrophysics*, *55*(04), 294–303.

Liu, M., Meakin, P. & Huang, H. (2007). Dissipative particle dynamics simulation of pore-scale multiphase fluid flow. *Water Resources Research*, *43*(4). doi:10.1029/2006WR004856

Manwart, C., Aaltosalmi, U., Koponen, A., Hilfer, R. & Timonen, J. (2002). Lattice-Boltzmann and finite-difference simulations for the permeability for three-dimensional porous media. *Physical Review E*, *66*(1), 016702. doi:10.1103/PhysRevE.66.016702

Okumura, S. & Sasaki, O. (2014). Permeability reduction of fractured rhyolite in volcanic conduits and its control on eruption cyclicity. *Geology*, *42*(10), 843–846. doi:10.1130/G35855.1

Pan, C., Hilpert, M. & Miller, C. T. (2004). Lattice-Boltzmann simulation of two-phase flow in porous media. *Water Resources Research*, *40*(1). doi:10.1029/2003WR002120

Rieg, F., Hackenschmidt, R. & Alber-Laukant, B. (2019). *Finite Elemente Analyse für Ingenieure: Grundlagen und praktische Anwendungen mit Z88Aurora*. München: Carl Hanser Verlag.

Rust, A. C. & Cashman, K. V. (2004). Permeability of vesicular silicic magma: inertial and hysteresis effects. *Earth and Planetary Science Letters*, *228*(1-2), 93–107. doi:10.1016/j.epsl.2004.09.025

Saxena, N., Hofmann, R., Alpak, F. O., Dietderich, J., Hunter, S. & Day-Stirrat, R. J. (2017). Effect of image segmentation & voxel size on micro-CT computed effective transport & elastic properties. *Marine and Petroleum Geology*, *86*, 972–990. doi:10.1016/j.marpetgeo.2017.07.004

Shabro, V., Kelly, S., Torres-Verdín, C., Sepehrnoori, K. & Revil, A. (2014). Pore-scale modeling of electrical resistivity and permeability in FIB-SEM images of organic mudrock. *Geophysics*, *79*(5), D289–D299. doi:10.1190/geo2014-0141.1

Takeuchi, S., Nakashima, S. & Tomiya, A. (2008). Permeability measurements of natural and experimental volcanic materials with a simple permeameter: Toward an understanding of magmatic degassing processes. *Journal of Volcanology and Geothermal Research*, *177*(2), 329–339. doi:10.1016/j.jvolgeores.2008.05.010

Wesseling, P. (1995). *Introduction to multigrid methods*. New York: John Wiley & Sons.

Woidt, W.-D. (1978). Finite element calculations applied to salt dome analysis. *Tectonophysics*, *50*(2), 369–386. doi:https://doi.org/10.1016/0040-1951(78)90143-9

Wright, H. M. N., Cashman, K. V., Rosi, M. & Cioni, R. (2007). Breadcrust bombs as indicators of Vulcanian eruption dynamics at Guagua Pichincha volcano, Ecuador. *Bulletin of Volcanology*, *69*(3), 281–300. doi:10.1007/s00445-006-0073-6

Wright, H. M. N., Roberts, J. J. & Cashman, K. V. (2006). Permeability of anisotropic tube pumice: Model calculations and measurements. *Geophysical Research Letters*, *33*(17). doi:10.1029/2006GL027224

Zeinijahromi, A., Farajzadeh, R., Bruining, J. H. & Bedrikovetsky, P. (2016). Effect of fines migration on oil–water relative permeability during two-phase flow in porous media. *Fuel*, *176*, 222–236. doi:10.1016/j.fuel.2016.02.066

Chapter 3 | Synopsis

In geosciences the flow of fluids is a key process for magma migration and ground water flows on multiple scales. A parameter controlling fluid flow on the micro- and macroscale is permeability. As permeability itself is controlled by its microstructure an accurate determination on the microscale is necessary (Mostaghimi et al., 2013). For this reason various studies measured permeability experimentally using different methods (Keehm, 2003; Bernabe et al., 1982; Bourbie et al., 1992; Brace, 1984). Most of laboratory measurements exhibit some limitations (Zeinijahromi et al., 2016; Gerke et al., 2018; Ferland et al., 1996; Dikinya et al., 2008; Cui et al., 2009) and do not provide information on flow and microstructural parameters. Therefore, the approach of Digital Rock Physics (DRP) gained significant importance to complement and enhance laboratory measurements. Digital Rock Physics (DRP) uses structural images (e.g., micro computed tomography (CT), Nuclear Magnetic Resonance (NMR) images) (Dvorkin et al., 2003; Arns et al., 2001; Arns, 2004) and different numerical techniques (e.g. Finite Difference (Manwart et al., 2002; Shabro et al., 2014; Gerke et al., 2018), Finite Element (Garcia et al., 2009a; Akanji and Matthai, 2010; Bird et al., 2014), Lattice-Boltzmann method (Bosl et al., 1998; Pan et al., 2004; Guo and Zhao, 2002)) to compute flow, elastic (Saxena and Mavko, 2016; Saxena et al., 2017a) and microstructural parameters (Knackstedt and Zhang, 1994). With the ascent of new technologies it has become possible to use DRP on large computational clusters and therefore provide new insights on 3D flow patterns and high resolution microstructural features.

The aim of the work presented in this cumulative thesis is to use DRP to investigate fluid flow and processes involved in the Deep Earth Volatile Cycle on multiple scales ranging from the micro- to the macroscale.

The first project (Chapter 4) uses the stencil rescaling method to improve the computation of fluid flow and therefore permeability on the pore scale. We benchmark the Finite Difference code LaMEM against various analytical solutions including simple Hagen-Poiseuille tubes and simple cubic packing. We furthermore can reproduce the experimentally measured permeability for a Fontainebleau sandstone sample and additionally show numerical convergence.

The second project (Chapter 5) uses an interdisciplinary approach to provide a permeability parameterization to use as input parameter in large-scale numerical models. For this reason we sinter glass bead sample with various porosities and determine permeability experimentally and numerically. We furthermore investigate the microstructure in terms of effective porosity, effective specific surface and hydraulic tortuosity using image processing. By using the well-known Kozeny-Carman relation a parameterization for permeability is proposed, representing sedimentary rocks down to $\approx 20\,\mathrm{km}$.

Finally, the last project (Chapter 6) investigates fluid flow on the large-scale in a subduction zone. We use the Finite Element code MVEP2 to compute the solid velocity within the mantle wedge by reproducing the analytical solution for a cornerflow, whereas the fluid velocity is computed by implementing a water migration scheme.

3.1 Pore-scale permeability prediction

This section summarizes the following published paper included in Chapter 4:

Eichheimer, P., Thielmann, M., Popov, A., Golabek, G. J., Fujita, W., Kottwitz, M. O. and Kaus, B. J. P. (2019): Pore-scale permeability prediction for Newtonian and non-Newtonian fluids, *Solid Earth*, 10, 1717–1731, doi: 10.5194/se-10-1717-2019.

Author contributions: PE did the bulk of the work, including writing, visualization, methodology and running simulations. MT and GJG designed the study and contributed to manuscript writing. AP implemented stencil rescaling into LaMEM. WF assisted in code benchmarking. MOK performed the resolution test for Fontainebleau subsamples. BJPK contributed to data interpretation and manuscript writing.

In recent years several authors used the approach of Digital Rock Physics to compute fluid flow and permeability including Finite Difference-, Finite Element- and Lattice-Boltzmann method (e.g. Gerke et al., 2018; Akanji and Matthai, 2010; Mostaghimi et al., 2013; Saxena et al., 2017b). Some of these studies still show large errors compared to experimental measurements, which can be related to the influence of segmentation and resolution (Andrä et al., 2013; Keehm, 2003). In case of high resolution structural images, it is still challenging to compute fluid flow even with the use of large computational clusters. To increase efficiency and precision for these computations, the method of stencil rescaling can be applied which has been used in different manners (Mostaghimi et al., 2013; Manwart et al., 2002; Vasilyev et al., 2016).

When computing fluid flow of a porous medium using Finite Differences attention needs to be drawn on the interface between the solid and fluid phase (see Section 4.4). The stencil rescaling approach, implemented by Anton Popov, improves the computation at these boundaries. To demonstrate the increased precision LaMEM is benchmarked against several numerical settings for which analytical solutions are known, showing very good agreement. For a Fontainebleau sandstone sample we reproduce an experimentally measured permeability and furthermore show numerical convergence (see Fig. 3.1).

In recent years, the flow of non-Newtonian fluids as of nanofluids and magma has gained significant interest in several scientific fields (Johnston et al., 2004; Suleimanov et al., 2011; Mader et al., 2013; Choi, 2009). For this reason we show the ability of LaMEM to handle complex fluid rheologies by computing fluid flow within

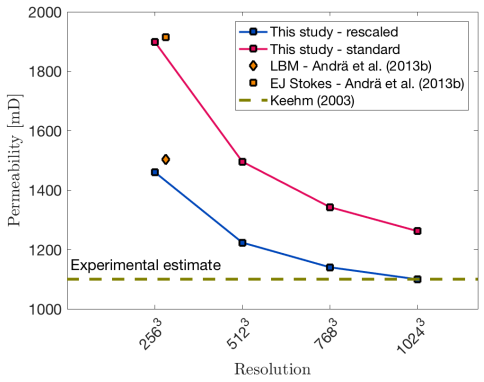

Figure 3.1: Computed permeability values against grid resolution. Orange symbols denote simulations using Lattice-Boltzmann method (LBM) and explicit jump stokes (EJ Stokes), both methods are used in Andrä et al. (2013b). Blue data points represent simulations using stencil rescaling while simulations represented by red dots use the standard method. Brown dotted line symbolizes the experimental estimate from Keehm (2003). Similar convergence has been also observed in Lattice-Boltzmann simulations (Khirevich et al., 2015; Khirevich and Patzek, 2018).

a Fontainebleau sandstone sample using a non-Newtonian fluid rheology. In Fig. 3.2 the applied pressure ΔP at the top boundary is plotted against the volume average velocity v_m. The computed slopes are in good agreement with the used power-law coefficients of 0.5 and 1.

In conclusion, the method of stencil rescaling shows:

- Stencil rescaling can compute fluid flow and permeability more precisely at no additional computational costs.
- We reproduce the experimentally and numerically determined permeability for a Fontainebleau sandstone sample. Furthermore we show numerical convergence for the first time.
- The ability of LaMEM to compute fluid flow with non-Newtonian rheology is demonstrated for a Fontainebleau sandstone sample.

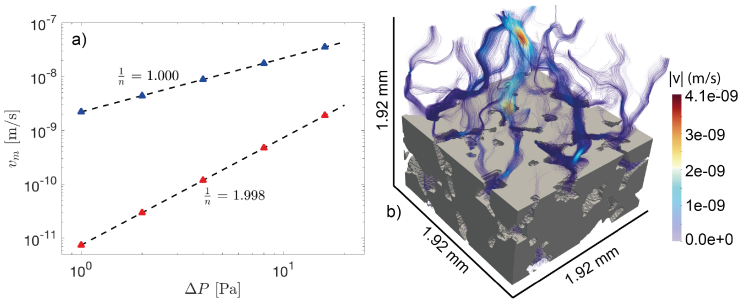

Figure 3.2: Computed results for the Fontainebleau sample using non-Newtonian rheology. **a)** shows the mean velocity against the applied pressure at the top boundary. Red and blue triangles symbolize each simulation and the corresponding dotted black line represents the fitted curve through the obtained data with slope $\frac{1}{n}$. **b)** illustrates computed streamlines of the Fontainebleau subsample using a power law coefficient of 0.5. Solid material is displayed in grey and the streamlines are colored according to computed velocities.

3.2 Numerical and experimental permeability determination

This section summarizes the following submitted manuscript included in Chapter 5:

Eichheimer, P., Thielmann, M., Fujita, W., Golabek, G. J., Nakamura, M., Okumura, S., Nakatani, T. and Kottwitz, M. O. (2020): Combined numerical and experimental study of microstructure and permeability in porous granular media, *Solid Earth*, 11, 1079-1095, doi: 10.5194/se-11-1079-2020.

Author contributions: PE contributed in designing the study, sample preparation and permeability measurements. Futhermore PE did visualization, writing, methodology and running simulations. MT contributed in data interpretation, methodology, designing the study and manuscript writing. WF performed sample preparation and permeability measurements. GJG contributed in designing the study, data interpretation and manuscript writing. MN designed the study and contributed in data interpretation. SO contributed in sample preparation and measurement. TK sintered the glass bead porous media. MOK performed the resolution test.

Fluid flow within sedimentary rocks is of major importance in subduction zone modelling. Most of the large-scale numerical models assume permeability to be constant or to change according to porosity-permeability relations estimated from arbitrary samples (Bryant et al., 1975; Neuzil, 1994; Gamage et al., 2011). Therefore, parameterizing permeability requires systematic datasets. Yet, very few data sets exist investigating the microstructure and related flow parameters using systematic data sets. Using an interdisciplinary approach, we parameterize permeability using both numerical and experimental methods providing permeability parameterizations only dependent on porosity, which an be used as input parameter for large-scale numerical simulations.

In the following, various glass bead samples are sintered ranging from 2 - 22% porosity. The permeability of the glass bead samples is measured experimentally using the permeameter of Takeuchi et al. (2008) and numerically using LaMEM (Kaus, 2010; Eichheimer et al., 2019). A summary of the entire workflow is shown in Fig. 3.3.

To predict permeability accurately we determine necessary microstructural parameters using image processing. The resulting relations for specific surface and hydraulic tortuosity, using the relations of Koponen et al. (1996) and Koponen et al. (1997) as a function of porosity, read as follows:

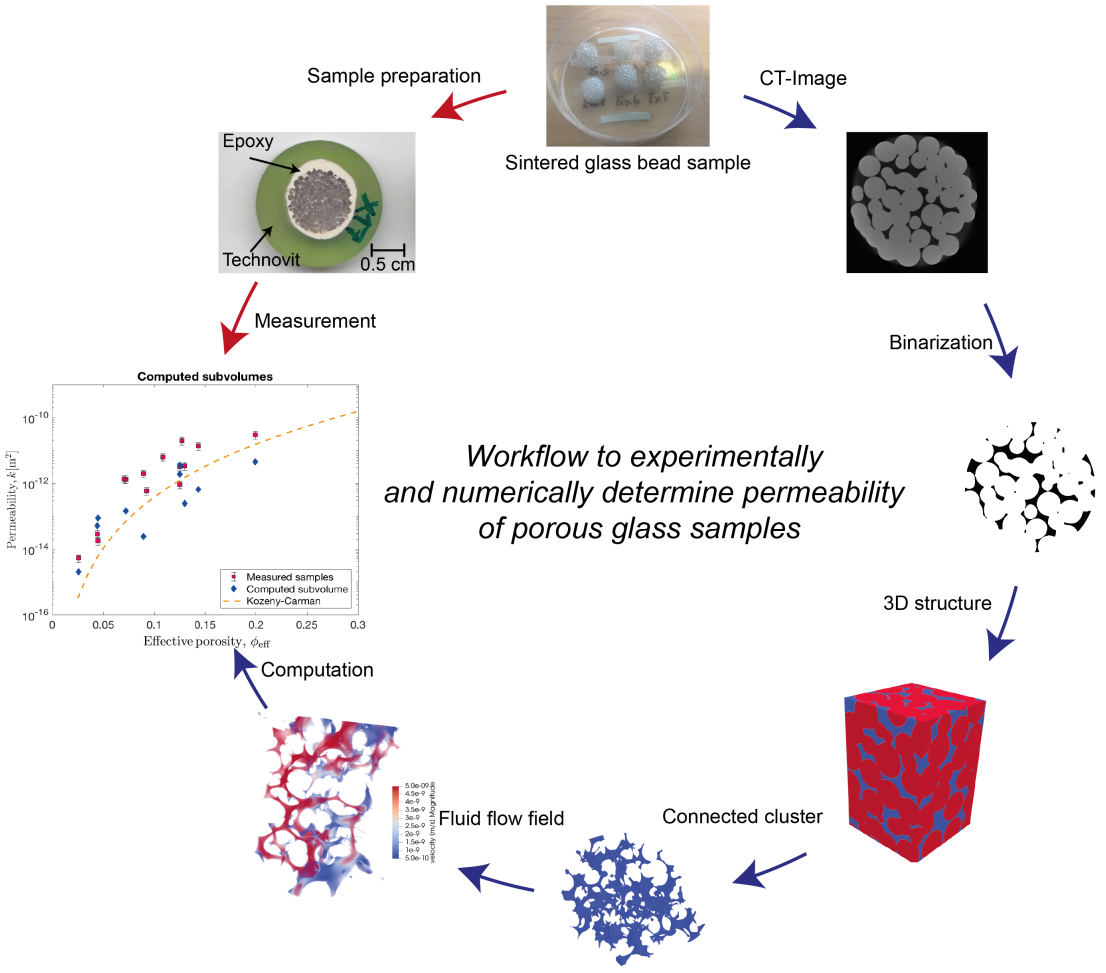

Figure 3.3: Workflow process map - red arrows mark the experimental workflow, whereas blue arrows indicate the numerical workflow.

$$S(\phi_{\text{eff}}) = -\frac{3}{3.8509 \times 10^{-4}\, m}\phi_{\text{eff}}, ln(\phi_{\text{eff}}) \tag{52}$$

$$\tau(\phi_{\text{eff}}) = -0.8712\phi_{\text{eff}} + 3.021. \tag{53}$$

By plugging the microstructural relations (eq. (52) and (53)) into several permeability parameterization we are able to compare the experimentally and numerically determined values to the predictions (see Fig. 3.4). The well-known Kozeny-Carman relation and the permeability parameterization used in Martys et al. (1994) are capable to predict the numerically and experimentally determined permeabilities obtainedin our study. We therefore provide modified versions of these parameterizations reading as:

$$k = k_0 \frac{(\phi_{\text{eff}} - \phi_c)^3}{[-0.8712\phi_{\text{eff}} + 3.021]^2 \cdot \left[-\frac{3}{3.8509\times10^{-4}\, m}\phi_{\text{eff}} ln(\phi_{\text{eff}})\right]^2}, \tag{54}$$

$$k = \frac{2[1 - min(\phi_{\text{eff}}) - \phi_c]}{\left[-\frac{3}{3.8509\times10^{-4}\,m}\phi_{\text{eff}} ln(\phi_{\text{eff}})\right]^2}[min(\phi_{\text{eff}}) - \phi_c]^{4.2}, \tag{55}$$

with ϕ_c being the critical porosity below which not continous path through the sample exists. This critical porosity is determined from the sintered glass bead samples. Eqs. (54) and (55) represent permeability of sedimentary rocks, like sandstones, down to $\approx$ 20 km. Using this workflow the permeability for different grain shapes and rock types, typically for subduction zones can be parameterized.

In conclusion, this study shows:

- Microstructural parameters (effective porosity, effective specific surface and hydraulic tortuosity) are successfully determined using image processing.
- A modified version of the Kozeny-Carman relation is provided, which can be used as input parameter for large-scale geodynamic simulations.
- The permeability parameterization is tested against experimentally measured and numerically calculated permeability values, showing good agreement.

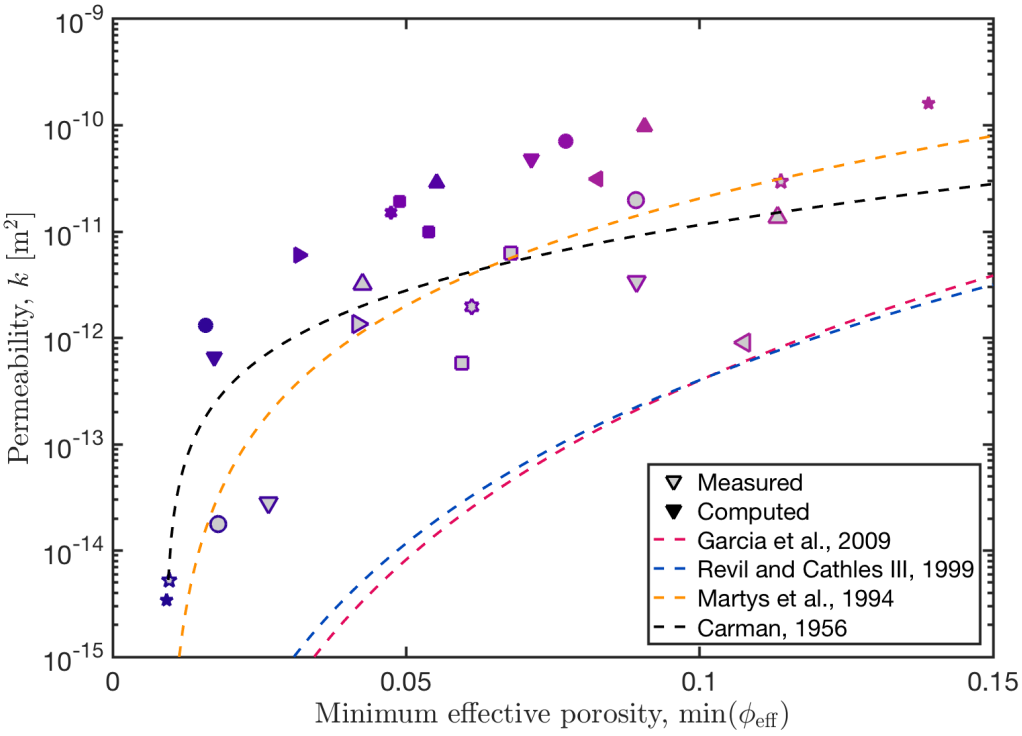

Figure 3.4: Computed and measured permeability against minimum effective porosity. Symbols of the same shape and color represent the same sample. Samples with grey face color represent measured values, whereas color only symbols stand for computed subsamples. The computed permeabilities represent the geometric mean values of all subsamples. To verify existing permeability parameterizations, we plotted the relations of Revil and Cathles III (1999), Garcia et al. (2009b) and Carman (1956) and Martys et al. (1994) against the experimental and numerical permeabilities. Note that estimated errors for the experimental permeability measurements (tab.5.1a) are smaller than the displayed symbols. Some subsamples with low effective porosity did not show a continuous pathway throughout the subsample, thus we assumed a very low permeability of $10^{-20}\,\mathrm{m}^2$.

3.3 Fluid flow in subduction zones

This section summarizes the manuscript in preparation included in Chapter 6:

Eichheimer, P., Thielmann, M. & Golabek, G. J. : Modelling of volatiles in Earth's mantle, *in prep.*

Author contributions: PE performed the benchmarks on corner flow and water migration as well as visualization, data interpretation and writing. The water migration scheme was implemented by MT and PE. Furthermore MT and GJG contributed in data interpretation, manuscript writing and designing this study.

For decades, the input of volatiles, especially H_2O, through subduction zones into the deep mantle has been investigated by several studies, leading to a wide variety of estimated values (see Fig. 3.5; von Huene and Scholl, 1991; Wallmann, 2001; Rüpke et al., 2004; Iwamori, 2007; Johnson and Pruis, 2003; van Keken et al., 2011; Magni et al., 2014; Korenaga et al., 2017; Abers et al., 2017; Cai et al., 2018). Water is transported into the mantle as pore or mineralogically bound water. The pore water is mostly released at shallow depth (< 20 km) through expulsion (Miller et al., 2003; Hensen et al., 2004; Abers, 2005). At depth between $20 - 100$ km additional water is released from both sediments and altered oceanic crust, which could lead to 'cold upwellings' (Gerya et al., 2002). At depths larger than > 100 km, deep fluids are released due to metamorphic dehydration reactions such as those of serpentine and amphibole. These fluids rise upwards into the mantle wedge leading to arc volcanism (Schmidt and Poli, 1998; Davies, 1999; Stern, 2002; Rüpke et al., 2004; Ohtani, 2005).

To investigate fluid flow within a subduction zone the Finite-Element code MVEP2 is used to simulate fluid flow in the mantle wedge. Modelling fluid flow within a subduction zone requires to compute the solid velocity of the mantle wedge and fluid velocity of the percolating water. Movement of the solid mantle wedge is successfully benchmarked against an analytical solution for corner flow taken from Batchelor (1967). Additionally the fluid velocity of H_2O is computed using a three step water migration scheme from Quinquis and Buiter (2014): (1) the amount of free and bound water as well as the maximum storage capacity of each marker is determined. (2) the pressure gradients of the solid phase flow are extracted to compute Darcy velocities. (3) the free water is advected along the pressure gradients with the computed Darcy velocities.

The interpolation of free water between markers and mesh is done using a k-nearest neighbour algorithm. If the amount of mineralogically bound water of the marker

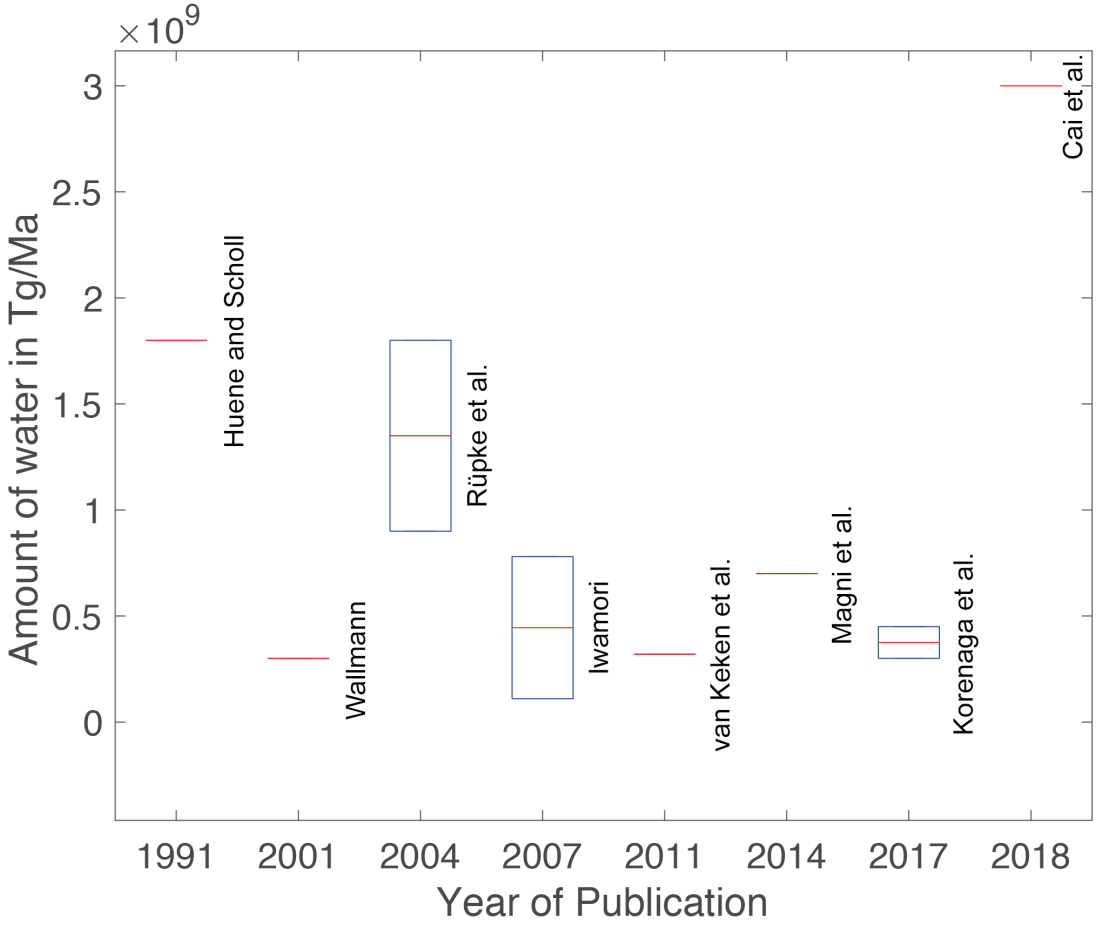

Figure 3.5: Estimated values of water influx into the mantle suggested by various authors. As explained above predictions differ since authors focused on different influx mechanisms and therefore used various assumptions. Red lines indicate the mean estimate, whereas blue boxes represent the minimum and maximum estimated values from each study.

exceeds the water storage capacity, the marker is oversaturated in water and dehydrates. The released free water moves through the model along the corresponding pressure gradients. If the mineralogically bound water of the marker is below the storage capacity, the marker is undersaturated in water and no free water is released. Instead it can incorporate free water, which was released through dehydration of oversaturated particles.

Figure 3.6 shows a benchmark setup employing a hydrated sphere. The hydrated sphere moves along the given pressure gradient, hydrating the surrounding dry rock material with increasing time. In the last timestep the entire amount of free water is incorporated by the previously undersaturated markers.

In summary, this study shows:

- The analytical solution from Batchelor (1967) is successfully reproduced, which describes the solid velocity in the mantle wedge.
- A three step water migration scheme is successfully implemented and tested. The scheme conserves the total amount of water throughout the simulations.

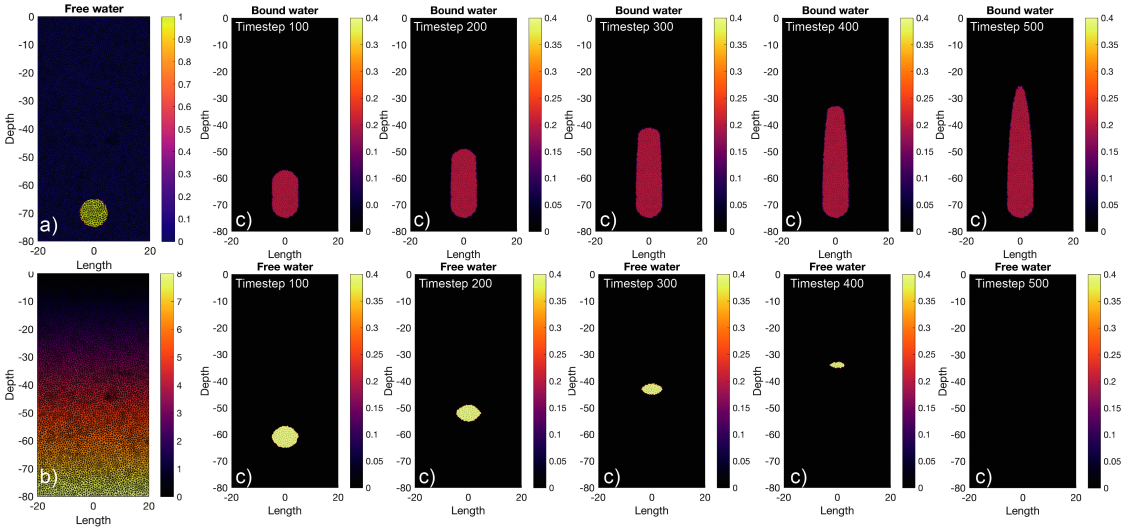

Figure 3.6: Benchmark setup using an hydrated sphere. **a)** shows the initial setup. An oversaturated sphere is placed within an undersaturated material. **b)** represents the applied pressure gradient in non-dimensional units. **c)** shows the model evolution over time. The free water moves upwards and is consumed by the undersaturated rock material. In the last timestep free water is completely incorporated into the surrounding rocks. All parameters in this model are non-dimensional.

References

Abers, G. A., van Keken, P. & Hacker, B. (2017). The cold and relatively dry nature of mantle forearcs in subduction zones. *Nature Geoscience*, *10*, 333–337. doi:10.1038/ngeo2922

Abers, G. A. (2005). Seismic low-velocity layer at the top of subducting slabs: observations, predictions, and systematics. *Physics of the Earth and Planetary Interiors*, *149*(1), 7–29. doi:10.1016/j.pepi.2004.10.002

Akanji, L. T. & Matthai, S. K. (2010). Finite element-based characterization of pore-scale geometry and its impact on fluid flow. *Transport in Porous Media*, *81*(2), 241–259. doi:10.1007/s11242-009-9400-7

Andrä, H., Combaret, N., Dvorkin, J., Glatt, E., Han, J., Kabel, M., ... Zhan, X. (2013). Digital rock physics benchmarks—Part II: Computing effective properties. *Computers & Geosciences*, *50*, 33–43. doi:https://doi.org/10.1016/j.cageo.2012.09.008

Arns, C. H. (2004). A comparison of pore size distributions derived by NMR and X-ray-CT techniques. *Physica A: Statistical Mechanics and its Applications*, *339*(1-2), 159–165. doi:10.1016/j.physa.2004.03.033

Arns, C. H., Knackstedt, M. A., Pinczewski, M. V. & Lindquist, W. (2001). Accurate estimation of transport properties from microtomographic images. *Geophysical Research Letters*, *28*(17), 3361–3364. doi:10.1029/2001GL012987

Batchelor, G. K. (1967). *An Introduction to Fluid Mechanics*. Cambridge: Cambridge University Press.

Bernabe, Y., Brace, W. & Evans, B. (1982). Permeability, porosity and pore geometry of hot-pressed calcite. *Mechanics of Materials*, *1*(3), 173–183. doi:https://doi.org/10.1016/0167-6636(82)90010-2

Bird, M., Butler, S. L., Hawkes, C. & Kotzer, T. (2014). Numerical modeling of fluid and electrical currents through geometries based on synchrotron X-ray tomographic images of reservoir rocks using Avizo and COMSOL. *Computers & Geosciences*, *73*, 6–16. doi:10.1016/j.cageo.2014.08.009

Bosl, W. J., Dvorkin, J. & Nur, A. (1998). A study of porosity and permeability using a lattice Boltzmann simulation. *Geophysical Research Letters*, *25*(9), 1475–1478. doi:10.1029/98GL00859

Bourbie, T., Coussy, O., Zinszner, B. & Junger, M. C. (1992). Acoustics of porous media. *The Journal of the Acoustical Society of America*, *91*(5), 3080–3080.

Brace, W. F. (1984). Permeability of crystalline rocks: New in situ measurements. *Journal of Geophysical Research: Solid Earth*, *89*(B6), 4327–4330. doi:10.1029/JB089iB06p04327

Bryant, W. R., Hottman, W. & Trabant, P. (1975). Permeability of unconsolidated and consolidated marine sediments, Gulf of Mexico. *Marine Geotechnology*, *1*(1), 1–14. doi:10.1080/10641197509388149

Cai, C., Wiens, D. A., Shen, W. & Eimer, M. (2018). Water input into the Mariana subduction zone estimated from ocean-bottom seismic data. *Nature*, *563*(7731), 389–392.

Carman, P. C. (1956). *Flow of gases through porous media*. New York: Academic Press.

Choi, S. U. (2009). Nanofluids: From vision to reality through research. *Journal of Heat Transfer*, *131*(3), 033106. doi:10.1115/1.3056479

Cui, X., Bustin, A. & Bustin, R. M. (2009). Measurements of gas permeability and diffusivity of tight reservoir rocks: different approaches and their applications. *Geofluids*, *9*(3), 208–223. doi:10.1111/j.1468-8123.2009.00244.x

Davies, J. H. (1999). The role of hydraulic fractures and intermediate-depth earthquakes in generating subduction-zone magmatism. *Nature*, *398*(6723), 142–145. doi:10.1038/18202

Dikinya, O., Hinz, C. & Aylmore, G. (2008). Decrease in hydraulic conductivity and particle release associated with self-filtration in saturated soil columns. *Geoderma*, *146*(1-2), 192–200. doi:10.1016/j.geoderma.2008.05.014

Dvorkin, J., Walls, J., Tutuncu, A., Prasad, M., Nur, A. & Mese, A. (2003). Rock Property Determination Using Digital Rock Physics. *SEG Technical Program Expanded Abstracts 2003*, 1660–1663. doi:10.1190/1.1817624

Eichheimer, P., Thielmann, M., Popov, A., Golabek, G. J., Fujita, W., Kottwitz, M. O. & Kaus, B. J. P. (2019). Pore-scale permeability prediction for newtonian and non-newtonian fluids. *Solid Earth*, *10*(5), 1717–1731. doi:10.5194/se-10-1717-2019

Ferland, P., Guittard, D. & Trochu, F. (1996). Concurrent methods for permeability measurement in resin transfer molding. *Polymer Composites*, *17*(1), 149–158. doi:10.1002/pc.10600

Gamage, K., Screaton, E., Bekins, B. & Aiello, I. (2011). Permeability–porosity relationships of subduction zone sediments. *Marine Geology*, *279*(1), 19–36. doi:10.1016/j.margeo.2010.10.010

Garcia, X., Akanji, L. T., Blunt, M. J., Matthai, S. K. & Latham, J. P. (2009a). Numerical study of the effects of particle shape and polydispersity on permeability. *Physical Review E*, *80*(2), 021304. doi:10.1103/PhysRevE.80.021304

Garcia, X., Akanji, L. T., Blunt, M. J., Matthai, S. K. & Latham, J. P. (2009b). Numerical study of the effects of particle shape and polydispersity on permeability. *Phys. Rev. E*, *80*, 021304. doi:10.1103/PhysRevE.80.021304

Gerke, K. M., Vasilyev, R. V., Khirevich, S., Collins, D., Karsanina, M. V., Sizonenko, T. O., ... Mallants, D. (2018). Finite-difference method Stokes solver (FDMSS) for 3D pore geometries: Software development, validation and case studies. *Computers & Geosciences*, *114*, 41–58. doi:10.1016/j.cageo.2018.01.005

Gerya, T. V., Stöckhert, B. & Perchuk, A. L. (2002). Exhumation of high-pressure metamorphic rocks in a subduction channel: A numerical simulation. *Tectonics*, *21*(6), 6-1-6-19. doi:10.1029/2002TC001406

Guo, Z. & Zhao, T. S. (2002). Lattice Boltzmann model for incompressible flows through porous media. *Physical Review E*, *66*(3), 036304. doi:10.1103/PhysRevE.66.036304

Hensen, C., Wallmann, K., Schmidt, M., Ranero, C. R. & Suess, E. (2004). Fluid expulsion related to mud extrusion off Costa Rica—A window to the subducting slab. *Geology*, *32*(3), 201–204. doi:10.1130/G20119.1

Iwamori, H. (2007). Transportation of H_2O beneath the Japan arcs and its implications for global water circulation. *Chemical Geology*, *239*(3-4), 182–198. doi:10.1016/j.chemgeo.2006.08.011

Johnson, H. & Pruis, M. J. (2003). Fluxes of fluid and heat from the oceanic crustal reservoir. *Earth and Planetary Science Letters*, *216*(4), 565–574. doi:https://doi.org/10.1016/S0012-821X(03)00545-4

Johnston, B. M., Johnston, P. R., Corney, S. & Kilpatrick, D. (2004). Non-Newtonian blood flow in human right coronary arteries: steady state simulations. *Journal of Biomechanics*, *37*(5), 709–720. doi:10.1016/j.jbiomech.2003.09.016

Kaus, B. J. P. (2010). Factors that control the angle of shear bands in geodynamic numerical models of brittle deformation. *Tectonophysics*, *484*(1-4), 36–47. doi:10.1016/j.tecto.2009.08.042

Keehm, Y. (2003). *Computational rock physics: Transport properties in porous media and applications* (Doctoral dissertation, Stanford University).

Khirevich, S., Ginzburg, I. & Tallarek, U. (2015). Coarse- and fine-grid numerical behavior of MRT/TRT lattice-Boltzmann schemes in regular and random sphere

packings. *Journal of Computational Physics*, *281*, 708–742. doi:10.1016/j.jcp.2014.10.038

Khirevich, S. & Patzek, T. W. (2018). Behavior of numerical error in pore-scale lattice Boltzmann simulations with simple bounce-back rule: Analysis and highly accurate extrapolation. *Physics of Fluids*, *30*(9), 093604. doi:10.1063/1.5042229

Knackstedt, M. A. & Zhang, X. (1994). Direct evaluation of length scales and structural parameters associated with flow in porous media. *Physical Review E*, *50*(3), 2134–2138. doi:10.1103/PhysRevE.50.2134

Koponen, A., Kataja, M. & Timonen, J. (1997). Permeability and effective porosity of porous media. *Phys. Rev. E*, *56*, 3319–3325. doi:10.1103/PhysRevE.56.3319

Koponen, A., Kataja, M. & Timonen, J. v. (1996). Tortuous flow in porous media. *Physical Review E*, *54*(1), 406–410. doi:10.1103/PhysRevE.54.406

Korenaga, J., Planavsky, N. J. & Evans, D. A. D. (2017). Global water cycle and the coevolution of Earth's interior and surface environment. *Philosophical Transactions of the Royal Society A: Mathematical, Physical and Engineering Sciences*, *375*(2094), 20150393. doi:10.1098/rsta.2015.0393

Mader, H. M., Llewellin, E. W. & Mueller, S. P. (2013). The rheology of two-phase magmas: A review and analysis. *Journal of Volcanology and Geothermal Research*, *257*, 135–158. doi:10.1016/j.jvolgeores.2013.02.014

Magni, V., Bouilhol, P. & van Hunen, J. (2014). Deep water recycling through time. *Geochemistry, Geophysics, Geosystems*, *15*(11), 4203–4216. doi:10.1002/2014GC005525

Manwart, C., Aaltosalmi, U., Koponen, A., Hilfer, R. & Timonen, J. (2002). Lattice-Boltzmann and finite-difference simulations for the permeability for three-dimensional porous media. *Physical Review E*, *66*(1), 016702. doi:10.1103/PhysRevE.66.016702

Martys, N. S., Torquato, S. & Bentz, D. P. (1994). Universal scaling of fluid permeability for sphere packings. *Phys. Rev. E*, *50*, 403–408. doi:10.1103/PhysRevE.50.403

Miller, S. A., van der Zee, W., Olgaard, D. L. & Connolly, J. A. D. (2003). A fluid-pressure feedback model of dehydration reactions: experiments, modelling, and application to subduction zones. *Tectonophysics*, *370*(1-4), 241–251. doi:10.1016/S0040-1951(03)00189-6

Mostaghimi, P., Blunt, M. J. & Bijeljic, B. (2013). Computations of Absolute Permeability on Micro-CT Images. *Mathematical Geosciences*, *45*(1), 103–125. doi:10.1007/s11004-012-9431-4

Neuzil, C. E. (1994). How permeable are clays and shales? *Water Resources Research*, *30*(2), 145–150. doi:10.1029/93WR02930

Ohtani, E. (2005). Water in the Mantle. *Elements*, *1*(1), 25–30. doi:10.2113/gselements.1.1.25

Pan, C., Hilpert, M. & Miller, C. T. (2004). Lattice-Boltzmann simulation of two-phase flow in porous media. *Water Resources Research*, *40*(1). doi:10.1029/2003WR002120

Quinquis, M. E. T. & Buiter, S. J. H. (2014). Testing the effects of basic numerical implementations of water migration on models of subduction dynamics. *Solid Earth*, *5*(1), 537–555. doi:10.5194/se-5-537-2014

Revil, A. & Cathles III, L. M. (1999). Permeability of shaly sands. *Water Resources Research*, *35*(3), 651–662. doi:10.1029/98WR02700

Rüpke, L. H., Morgan, J. P., Hort, M. & Connolly, J. A. D. (2004). Serpentine and the subduction zone water cycle. *Earth and Planetary Science Letters*, *223*(1-2), 17–34. doi:10.1016/j.epsl.2004.04.018

Saxena, N., Hofmann, R., Alpak, F. O., Dietderich, J., Hunter, S. & Day-Stirrat, R. J. (2017a). Effect of image segmentation & voxel size on micro-CT computed effective transport & elastic properties. *Marine and Petroleum Geology*, *86*, 972–990. doi:10.1016/j.marpetgeo.2017.07.004

Saxena, N. & Mavko, G. (2016). Estimating elastic moduli of rocks from thin sections: Digital rock study of 3D properties from 2D images. *Computers & Geosciences*, *88*, 9–21. doi:10.1016/j.cageo.2015.12.008

Saxena, N., Mavko, G., Hofmann, R. & Srisutthiyakorn, N. (2017b). Estimating permeability from thin sections without reconstruction: Digital rock study of 3D properties from 2D images. *Computers & Geosciences*, *102*, 79–99. doi:10.1016/j.cageo.2017.02.014

Schmidt, M. W. & Poli, S. (1998). Experimentally based water budgets for dehydrating slabs and consequences for arc magma generation. *Earth and Planetary Science Letters*, *163*(1-4), 361–379.

Shabro, V., Kelly, S., Torres-Verdín, C., Sepehrnoori, K. & Revil, A. (2014). Pore-scale modeling of electrical resistivity and permeability in FIB-SEM images of organic mudrock. *Geophysics*, *79*(5), D289–D299. doi:10.1190/geo2014-0141.1

Stern, R. J. (2002). Subduction zones. *Reviews of Geophysics*, *40*(4), 3-1-3-38. doi:10.1029/2001RG000108

Suleimanov, B. A., Ismailov, F. S. & Veliyev, E. F. (2011). Nanofluid for enhanced oil recovery. *Journal of Petroleum Science and Engineering*, *78*(2), 431–437. doi:10.1016/j.petrol.2011.06.014

Takeuchi, S., Nakashima, S. & Tomiya, A. (2008). Permeability measurements of natural and experimental volcanic materials with a simple permeameter: Toward an understanding of magmatic degassing processes. *Journal of Volcanology and Geothermal Research*, *177*(2), 329–339. doi:10.1016/j.jvolgeores.2008.05.010

van Keken, P. E., Hacker, B. R., Syracuse, E. M. & Abers, G. A. (2011). Subduction factory: 4. Depth-dependent flux of H_2O from subducting slabs worldwide. *Journal of Geophysical Research: Solid Earth*, *116*(B1). doi:10.1029/2010JB007922

Vasilyev, R. V., Gerke, K. M., Karsanina, M. V. & Korost, D. V. (2016). Solution of the Stokes equation in three-dimensional geometry by the finite-difference method. *Mathematical Models and Computer Simulations*, *8*(1), 63–72. doi:10.1134/S2070048216010105

von Huene, R. E. & Scholl, D. W. (1991). Observations at convergent margins concerning sediment subduction, subduction erosion, and the growth of continental crust. *Reviews of Geophysics*, *29*(3), 279–316.

Wallmann, K. (2001). The geological water cycle and the evolution of marine $\delta^{18}O$ values. *Geochimica et Cosmochimica Acta*, *65*(15), 2469–2485. doi:10.1016/S0016-7037(01)00603-2

Zeinijahromi, A., Farajzadeh, R., Bruining, J. H. & Bedrikovetsky, P. (2016). Effect of fines migration on oil–water relative permeability during two-phase flow in porous media. *Fuel*, *176*, 222–236. doi:10.1016/j.fuel.2016.02.066

Chapter 4 | Pore-scale permeability prediction using Newtonian and non-Newtonian fluid flow

Modified version of the paper published in *Solid Earth*: Eichheimer, P., Thielmann, M., Popov, A., Golabek, G. J., Fujita, W., Kottwitz, M. O. and Kaus, B. J. P. (2019): Pore-scale permeability prediction for Newtonian and non-Newtonian fluids, *Solid Earth*, 10, 1717–1731, doi: 10.5194/se-10-1717-2019

4.1 Abstract

The flow of fluids through porous media such as groundwater flow or magma migration are key processes in geological sciences. Flow is controlled by the permeability of the rock, thus an accurate determination and prediction of its value is of crucial importance. For this reason, permeability has been measured across different scales. As laboratory measurements exhibit a range of limitations, the numerical prediction of permeability at conditions where laboratory experiments struggle has become an important method to complement laboratory approaches. At high resolutions, this prediction becomes computationally very expensive, which makes it crucial to develop methods that maximize accuracy. In recent years, the flow of non-Newtonian fluids through porous media has gained additional importance due to e.g., the use of nanofluids for enhanced oil recovery. Numerical methods to predict fluid flow in these cases are therefore required.

Here, we employ the open-source finite difference solver LaMEM to numerically predict the permeability of porous media at low Reynolds numbers for both Newtonian as well as non-Newtonian fluids. We employ a stencil rescaling method to better describe the solid-fluid interface. The accuracy of the code is verified by comparing numerical solutions to analytical ones for a set of simplified model setups. Results show that stencil rescaling significantly increases the accuracy at no additional computational cost. Finally, we use our modeling framework to predict the permeability of a Fontainebleau sandstone, and demonstrate numerical convergence. Results show very good agreement with experimental estimates as well as with previous studies. We also demonstrate the ability of the code to simulate the flow of power law fluids through porous media. As in the Newtonian case, results show good agreement with analytical solutions.

4.2 Introduction

Fluid flow within rocks is of interest for several Earth Science disciplines including petrology, hydrogeology and petroleum geoscience, as fluid flow is relevant to the understanding of magma flow, groundwater flow, and oil flow respectively (Manwart et al., 2002). Permeability estimates can be inferred on several scales ranging from macroscale (crust) (Fehn and Cathles, 1979; Norton and Taylor Jr, 1979) over mesoscale (e.g. bore hole) (Brace, 1984) to pore scale (e.g. laboratory) (Brace, 1980). Permeability at crustal scale is of great importance as crustal scale permeability is a function of its complex microstructure, therefore an accurate prediction of permeab-

ility on the pore scale is necessary (Mostaghimi et al., 2013). Typical limitations for laboratory measurements on pore scale are: (i) change of the sample's microstructure and therefore its physical properties through cracking and self-filtration (Zeinijahromi et al., 2016; Dikinya et al., 2008) (ii) pressure changes due to the influence of wall effects (Ferland et al., 1996) and finally (iii) difficulties to measure irregular grain shapes and small grain sizes of the porous medium (Cui et al., 2009; Gerke et al., 2015).

At this point numerical modelling can help to compute permeabilities and understand the microstructures as well as flow patterns in three dimensional pore structures. To compute fluid flow directly within 3D pore structures it is necessary to determine the morphology of the investigated sample. This can be achieved by digital rock physics (DRP). It is a powerful tool which allows to improve the understanding of both pore scale processes and rock properties. DRP approaches use 2D or 3D microstructural images to compute fluid flows (Fredrich et al., 1993; Ferréol and Rothman, 1995; Keehm, 2003; Bosl et al., 1998), which are obtained using modern techniques including x-ray computer tomography and magnetic resonance imaging (Dvorkin et al., 2011; Arns et al., 2001; Arns, 2004). In a first step the obtained microstructural images undergo several stages of segmentation (binarization, smoothing etc.) necessary to create a three dimensional pore space. The subsequent computation of fluid flow through the reconstructed three dimensional pore space is tackled with either Lattice- Boltzmann (Bosl et al., 1998; Pan et al., 2004; Guo and Zhao, 2002) , Finite Difference (Manwart et al., 2002; Shabro et al., 2014; Gerke et al., 2018) or Finite Element methods (Garcia et al., 2009; Akanji and Matthai, 2010; M. Bird et al., 2014). The computed velocity field is then used to estimate permeability (Keehm, 2003; Saxena et al., 2017) and other physical properties (Saxena and Mavko, 2016; Knackstedt et al., 2009).

In recent years, the flow of non-Newtonian fluids has gained significant interest due to their use in a wide range of applications including geology, medicine and other industrial processes (e.g. Johnston et al., 2004; Choi, 2009; Suleimanov et al., 2011; Mader et al., 2013). Nanofluids contain nanometer-sized particles and have been shown to significantly enhance the efficiency of oil recovery (Wasan and Nikolov, 2003; Huang et al., 2013), whereas the bubbles and/or crystal content of magmas controls their rheology and thus ultimately their eruption style (Mader et al., 2013; Cassidy et al., 2018). If the suspended particles are much smaller than the system to be modeled, the behaviour of these suspensions is commonly described using an effective rheology, exhibiting non-Newtonian behaviour in most cases. For magmas it is not quite clear which physical process is responsible for the non-Newtonian behaviour (Deubelbeiss et al., 2011) as the non-Newtonian behaviour

usually originates from the interaction of suspended particles with each other and the surrounding fluid. Therefore, it is necessary to develop numerical models that can simulate non-Newtonian flow through porous media.

In this paper we enhance the open-source finite difference solver LaMEM to model fluid flow on pore-scale with both Newtonian as well as non-Newtonian rheologies. We show that rescaling the staggered grid stencil to better describe velocity components parallel to the fluid-solid interface significantly improves the accuracy. The code is verified using analytical solutions and then used to perform the permeability computations for a digital Fontainebleau sandstone sample (Andrä et al., 2013b).

4.3 Fluid flow in porous media

Fluid flow in porous media can be characterized with the Reynolds number which relates inertial to viscous forces:

$$Re = \frac{\rho v L}{\eta}, \tag{56}$$

where ρ is fluid density, v is velocity in direction of the flow, L is the characteristic length and η the fluid viscosity. Due to the small pore size, flows in porous media commonly exhibit small Reynolds numbers and are thus considered to be laminar (Bear, 1988). For geological applications, Reynolds numbers typically are around $10^{-9} - 10^{-10}$ for magmas (Glazner, 2014) and range from 10^{-8} to 10^{-5} for ground water flow. This allows to simplify the incompressible Navier-Stokes equations to the Stokes equations (ignoring gravity):

$$\frac{\partial v_i}{\partial x_i} = 0, \tag{57}$$

$$\frac{\partial}{\partial x_j}\left[\eta\left(\frac{\partial v_i}{\partial x_j} + \frac{\partial v_j}{\partial x_i}\right)\right] - \frac{\partial P}{\partial x_i} = 0, \tag{58}$$

where P denotes pressure, v the velocity component and x the spatial coordinate.

If the pore structure of a porous medium is known, eq. (57) and eq. (58) can be used to directly model laminar fluid flow within this medium. However, at larger scales direct numerical simulation of porous flow is not feasible. In the case of Newtonian fluids, it is common to define a permeability k which relates the flow rate Q to the

applied pressure gradient $\Delta P/L$ as well as fluid viscosity η:

$$k = -\frac{\eta L Q}{\Delta P A}, \tag{59}$$

where A is the cross-sectional area of the porous medium. Eq. (59) is also known as Darcy's law and forms the basis of an effective description of Newtonian fluid flow in porous media (Andrä et al., 2013b; Saxena et al., 2017; Bosl et al., 1998). As stated above, this permeability is commonly determined by experimental methods on all scales. With the advent of numerical models for subsurface fluid flow (e.g., FEFLOW (Diersch, 2013)), it has become possible to predict large scale subsurface fluid flow using micro permeabilities as input parameter. Therefore an accurate prediction of micro permeabilies is necessary.

One possibility to do this is to relate the porosity ϕ of the medium to its permeability k. Deriving the exact nature of this relationship is not trivial and has been subject to a significant amount of research (Kozeny, 1927; Carman, 1937, 1956; Mavko and Nur, 1997). Due to the strong dependency of the permeability not only on porosity, but also on the 3D structure of the pore space, these approaches still suffer from inaccuracies. Due to the development of pore-scale numerical models, it has become possible to determine and refine the porosity-permeability relationship using direct numerical simulation on the basis of computed tomography (CT). These simulations typically provide solutions for fluid velocity v and pressure P for a given pressure gradient across the sample. From the velocity field in z- direction the volume-averaged velocity component v_m is calculated (e.g. Osorno et al., 2015):

$$v_m = \frac{1}{V_f} \int_{V_f} |v_z| \, dv, \tag{60}$$

where V_f is the volume of the fluid phase. Making use of eq. (59) and $Q = v_m \cdot A$, the intrinsic permeability k_s of the sample can then be computed as:

$$k_s = \frac{\eta v_m L}{\Delta P}. \tag{61}$$

As described above, the flow of non-Newtonian fluids through porous media has gained considerable attention in recent years. Here, we use a power law rheology given by:

$$\eta = \begin{cases} \eta_1, & \text{if } \dot{\varepsilon} < \dot{\varepsilon}_1 \\ \eta_0 \left(\frac{\dot{\varepsilon}}{\dot{\varepsilon}_0}\right)^{n-1} & \\ \eta_2, & \text{if } \dot{\varepsilon} > \dot{\varepsilon}_2 \end{cases} \tag{62}$$

where η_1 and η_2 are the upper and lower cutoff viscosities at the corresponding strain-rates $\dot{\varepsilon}_1$ and $\dot{\varepsilon}_2$. η_0 is the fluid viscosity at the reference strain-rate $\dot{\varepsilon}_0$ and $\dot{\varepsilon} = \sqrt{\frac{1}{2}\dot{\varepsilon}_{ij}\dot{\varepsilon}_{ij}}$ the effective strain-rate. n is the power law exponent. With the definition adopted here, fluids with $n < 1$ are called shear-thinning, while fluids with $n = 1$ behave as Newtonian fluids and $n > 1$ are considered shear-thickening fluids. Note that this definition of n differs from the common definition used in geodynamical modelling (called n' here), where $n' = n^{-1}$.

In the case of non-Newtonian fluids, the definition of a permeability is not as straightforward as in the Newtonian case. Several studies have attempted to describe porous media permeability for non-Newtonian fluid rheologies. Until now a general description could not be found as used approaches differ. To develop a nonlinear variant of Darcy's law, R. Bird et al. (2006) assumed that porous media can be represented by parallel pipes and scaled up these capillary models to general porous media. By doing so, he suggested that the average velocity v_m scales as a function of the driving force F or the pressure gradient $\Delta P/L$ (R. Bird et al., 2006; Larson, 1981):

$$v_m = \left(\frac{k}{\eta_{eff}}\frac{\Delta P}{L}\right)^{\frac{1}{n}} = K_F \left(F\right)^{\frac{1}{n}} \tag{63}$$

where k is the permeability, η_{eff} an effective viscosity and K_F a related model parameter. If $n = 1$ and $\eta_{eff} = \eta$, eq. (59) is recovered. Both the fraction k/η_{eff} as well as K_F depend on porosity ϕ, stress exponent n, the reference viscosity η_0 and the pore scale geometry of the medium. Consequently, a simple expression for the permeability k has not been found yet. Attempts to generalize Darcy's law based on eq. (63) include effective medium theories (Sahimi and Yortsos, 1990), pore network models (Shah and Yortsos, 1995) and pore-scale numerical simulations (Aharonov and Rothman, 1993; Vakilha and Manzari, 2008). Irrespective of the chosen approach and the exact form of either k/η_{eff} or K_F, eq. (63) implies that a logarithmic plot of v_m vs. either $\Delta P/L$ or F should produce a straight line with slope $1/n$.

4.4 Method

We solve the system of governing equations (57) and (58) on a cubic lattice using the finite difference code LaMEM, which has originally been developed to simulate large scale deformation of the Earth's lithosphere and mantle (Kaus et al., 2016). Here, we will focus on modeling the flow of a fluid with both linear and non-linear viscosity η through a rigid porous matrix. LaMEM employs a staggered grid finite difference scheme (Harlow and Welch, 1965) to discretize the governing equations (Fig. 4.1). Pressures are defined in the middle of the staggered grid cell, whereas velocities are defined on cell faces. Based on the data from CT-scans, each cell is assigned either a fluid or a solid phase. The discretized system is then solved using an iterative multigrid scheme to obtain values for velocities v and pressure P. To this end, we employ multigrid solvers which are part of the PETSc library (Balay et al., 2010). As only cells belonging to the fluid phase exhibit non-zero values for the velocity, the velocity components belonging to solid cells are directly set to zero and only considered as boundary conditions. This greatly reduces the degrees of freedom of the system to be solved and hence also the computational cost. Pressures are fixed on the top and bottom boundaries and free slip boundary conditions are employed on the side boundaries. As described above, no slip boundary conditions apply at the solid-fluid interface. To solve the linear system of equations a V-cycle geometric multiplicative multigrid solver is used (Fedorenko, 1964; Wesseling, 1995). The multigrid solver operates on up to five multigrid levels depending on the given input model. Convergence criteria are given by a relative convergence tolerance of 10^{-8} and an absolute convergence tolerance of 10^{-10} (see appendix 4.8.1). The absolute

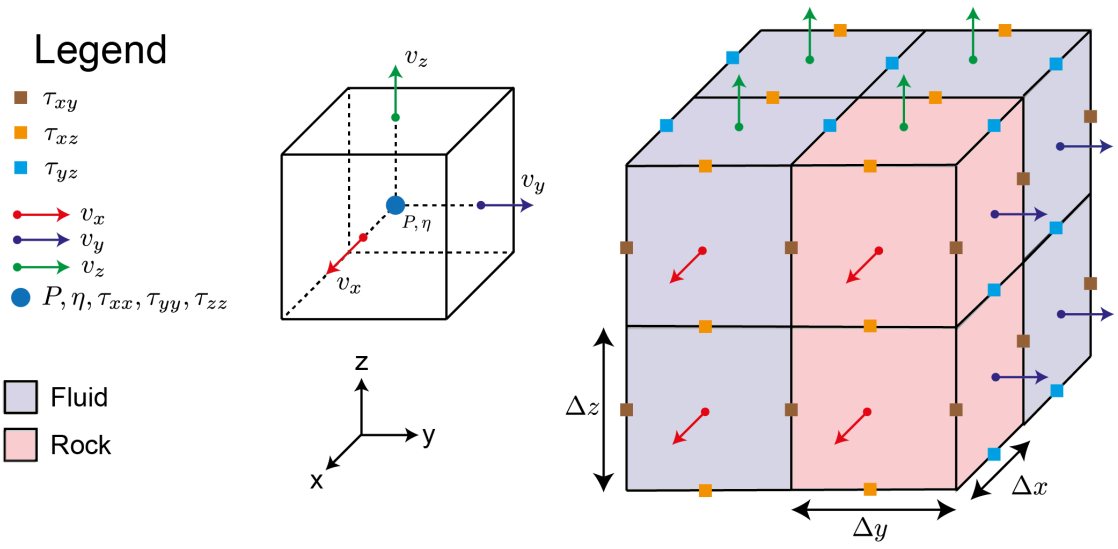

Figure 4.1: Staggered grid and location of variables.

convergence tolerance *atol* is defined as the absolute size of the residual norm and *rtol* the decrease of the residual norm relative to the norm of the right hand side. Therefore convergence at iteration k is reached for:

$$\|\mathrm{r_k}\|_2 < \max(\mathrm{rtol} \cdot \|\mathrm{b}\|_2, \mathrm{atol}), \tag{64}$$

where $r_k = b - Cx_k$ with b is the right-hand-side vector, x the solution vector of the current timestep k and C the matrix representation of a linear operator (Balay et al., 2010).

Assigning solid and fluid phases to different cells defines the location of the fluid-solid interface. In the case of a staggered grid, the location of the interface therefore does not correspond to the location of the interface-parallel velocity component. To illustrate this issue, the discretization stencil of a shear stress component τ_{xy} is shown in Fig. 4.2. When no interfaces are present (Fig. 4.2a) the finite different discretization results in the following expression (k-index is omitted for brevity):

$$\tau_{xy(i,j)} = \eta \frac{v_{x(i,j)} - v_{x(i,j-1)}}{\Delta y} + \eta \frac{v_{y(i,j)} - v_{y(i-1,j)}}{\Delta x} \tag{65}$$

When stencils contain rock cells (e.g. Fig. 4.2b) we can straightforwardly enforce the no-flow conditions at their boundaries:

$$\begin{aligned} v_{x(i,j-1)} &= 0, \\ v_{y(i-1,j)} &= 0, \end{aligned} \tag{66}$$

to obtain:

$$\tau_{xy(i,j)} = \eta \frac{v_{x(i,j)}}{\Delta y} + \eta \frac{v_{y(i,j)}}{\Delta x}. \tag{67}$$

This form, however, does not enforce interface-parallel velocities to be zero at the interface locations, which results in sub-optimal convergence. Alternatively, the exact constraints can be enforced:

$$\begin{aligned} \frac{v_{x(i,j)} + v_{x(i,j-1)}}{2} &= 0, \\ \frac{v_{y(i,j)} + v_{y(i-1,j)}}{2} &= 0, \end{aligned} \tag{68}$$

which will give:

$$\tau_{xy(i,j)} = 2\eta \frac{v_{x(i,j)}}{\Delta y} + 2\eta \frac{v_{y(i,j)}}{\Delta x}. \tag{69}$$

The specific expression will depend on the exact subset of cells occupied by rock. The discretization of the other components is performed in a similar manner. The above modification of the shear stress discretization stencil is called here "stencil res-

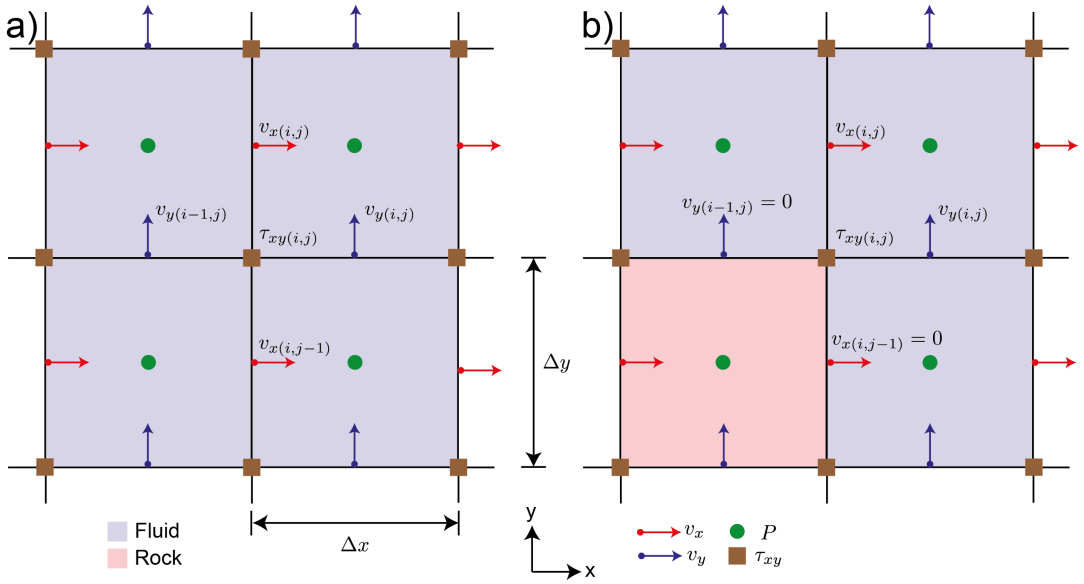

Figure 4.2: Staggered grid stencil rescaling. **a)** Stencil without interfaces and **b)** with solid interfaces. The sketch is based on a cross section of Fig. 4.1 in the $x - y$ plane.

caling". Similar approaches have already been presented in the literature (Vasilyev et al., 2016; Mostaghimi et al., 2013; Manwart et al., 2002). Both Manwart et al. (2002) and Mostaghimi et al. (2013) presented tests to validate their method. The test performed in Manwart et al. (2002) (permeability of a cubic array of spheres) exhibits nonmonotonous convergence of the numerical solution. Mostaghimi et al. (2013) validated their method by comparing the numerical solution to the analytical solution of flow between two parallel plates. They found that they were able to compute the velocity "to within machine accuracy" if they used more than two grid cells, but did not provide any information about convergence of the effective permeability.

4.5 Comparison with analytical solutions

To verify the method presented above, we performed a series of benchmark tests where we compared numerical solutions of simplified model setups to their respective analytical solutions. For simplicity, we non-dimensionalized the governing equations (57) and (58) as well as the rheology given in eq. (62) with characteristic values for

viscosity η_c, length l_c, stress τ_c and velocity v_c:

$$\eta = \eta_c \cdot \widetilde{\eta}, \tag{70}$$

$$x_i = l_c \cdot \widetilde{x}_i, \tag{71}$$

$$\tau = \tau_c \cdot \widetilde{\tau}, \tag{72}$$

$$v_i = v_c \cdot \widetilde{v}_i = \frac{l_c \tau_c}{\eta_c} \cdot \widetilde{v}_i, \tag{73}$$

where the characteristic value for v_c can be derived from the other characteristic values. Non-dimensional values are denoted with a $\widetilde{}$. For the remainder of this section, we will only use non-dimensional values and drop the $\widetilde{}$ for simplicity. Benchmark tests are organized as follows: first, we will present three benchmark tests for the flow of a Newtonian fluid through i) a single tube, ii) multiple tubes and iii) through a simple cubic sphere pack, which is followed by a benchmark test of power law fluid flow through a single tube. The difference between numerically and analytically computed permeabilities is then expressed using the L_2 norm of their relative misfit:

$$\|\delta_k\|_2 = \sqrt{\left(\frac{k_{comp} - k_{ana}}{k_{ana}}\right)^2}, \tag{74}$$

where k_{comp} is the computed and k_{ana} the analytically obtained permeability.

4.5.1 Newtonian flow through a single vertical tube

For a single vertical tube, the analytical solutions for both velocity v and flow rate Q are given as (e.g. Poiseuille, 1846; Landau and Lifshitz, 1987):

$$v = \frac{\Delta P}{4\eta L}(R^2 - r^2), \tag{75}$$

$$Q = \frac{\pi \Delta P}{8\eta L} R^4, \tag{76}$$

where $\frac{\Delta P}{L}$ is the pressure drop in z-direction, R is the radius of the pipe and r the integration variable. The characteristic scales in this case are given by $\eta_c = \eta_0$, $\tau_c = \Delta P$ and $l_c = R$ so that the pipe radius R, fluid viscosity η and pressure difference ΔP all take values of 1. The cubic model domain has an edge length of 4 units. Combining eq. (76) with eq. (59), the non-dimensional permeability is then given by:

$$k = \frac{L\frac{\pi\Delta P}{8\eta L}R^4}{\Delta PA} = \frac{\pi}{128}. \tag{77}$$

To assess the effect of different spatial resolutions, we conduct a resolution test where we increase resolution from 8^3 to 256^3 nodes with a constant grid spacing in each direction. Four sets of resolution tests were conducted. In the first two sets, permeability was computed using the standard finite difference approach without stencil rescaling. The two sets then differ due to the exact location of the pipe. In set 1, the location of the pipe was chosen in such a way that the pipe surface aligned with the numerical grid (standard, ON NODE) so that computational nodes were directly located on the fluid/solid interface in in x- and y-direction. In set 2 (standard, OFF NODE), the location of the pipe was shifted so that the fluid/solid interface was located between the respective computational nodes. The same procedure was applied to sets 3 and 4 where stencil rescaling was employed. The reason to do that was to determine the effect of well-aligned computational nodes, as this is often not the case in more complex geometries.

As expected, the numerical results generally show higher accuracy when stencil rescaling is employed and when node locations and interfaces of the tube are aligned (see Fig. 4.3). The order of convergence is linear for cases without rescaling or when the tube interface does not coincide with grid nodes, but superlinear if both rescaling is employed and interface and node location coincide.

4.5.2 Newtonian flow through multiple vertical tubes

In natural rocks larger channels tend to dominate the overall permeability. To assess this effect, we compute the flow through several straight tubes with different radii (Fig. 4.4). We use four pipes with non-dimensional radii given as $R_1 = 2$, $R_2 = 1$, $R_3 = 8$, $R_4 = 4$. The viscosity of the fluid is 1 and edge length of the cubic domain is 8. The simulations are performed in a similar manner as the single tube benchmark by increasing the number of grid points from 8^3 to 256^3. For each tube the analytical solution (eqs. (75) and (76)) is computed and the cumulative analytical permeability value is compared against computed values. The non-dimensional permeability in this case reads as:

$$k = \frac{LQ(R_1^4 + R_2^4 + R_3^4 + R_4^4)}{\Delta PA} \tag{78}$$

The individual tubes contribute to the absolute permeability as follows: P1 = 0.3662 %, P2 = 0.0229 %, P3 = 93.7514 %, P4 = 5.8595 %.

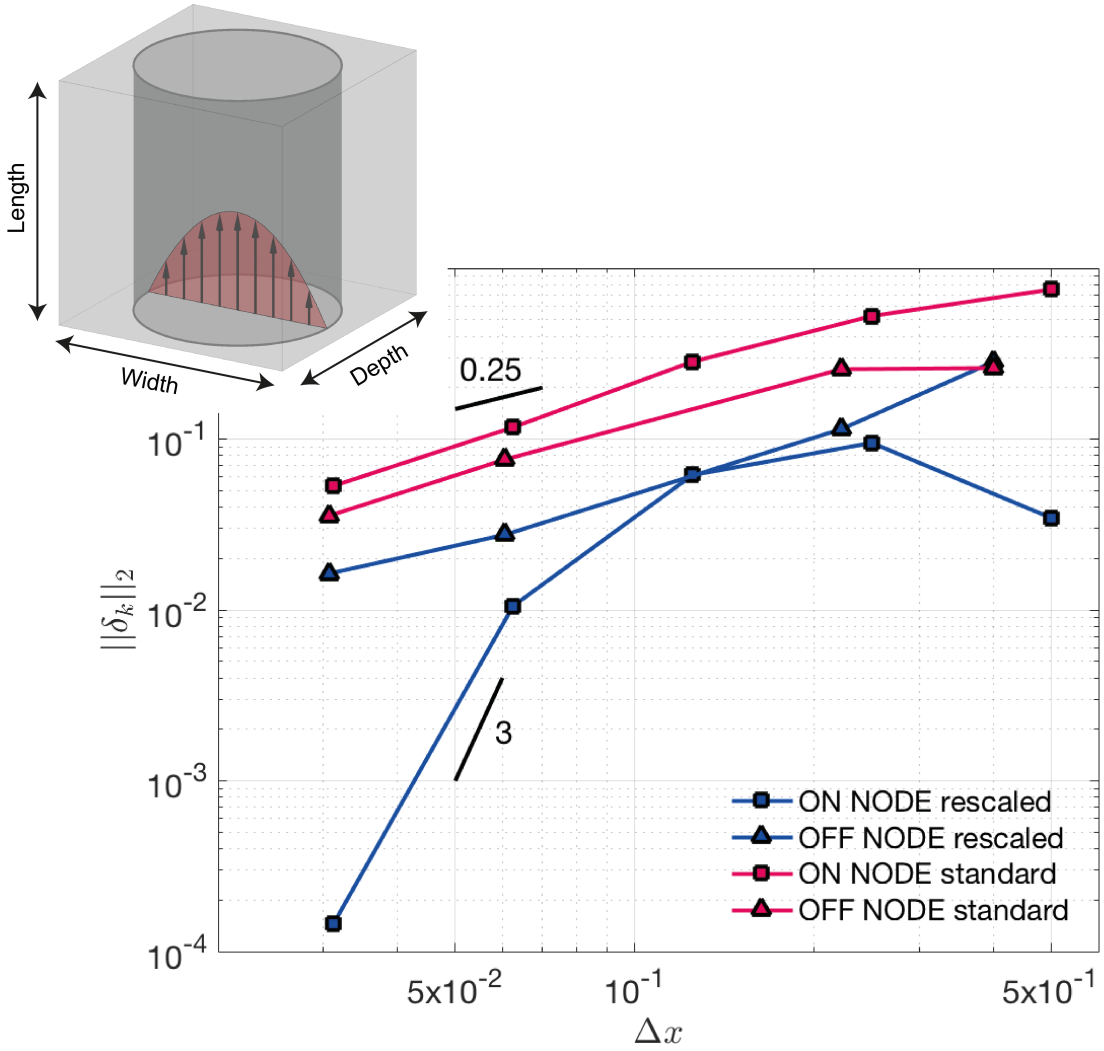

Figure 4.3: Hagen-Poiseuille benchmark results. Shown is the error norm $\|\delta_k\|_2$ vs. spatial resolution. The different curves show cases where the tube surface coincides with a nodal point (ON NODE) or not (OFF NODE). Blue lines represent simulations using stencil rescaling, whereas red lines denote simulations without stencil rescaling. To highlight convergence black lines with given slopes were added.

As observed for the single tube setup, the results show a lower relative error for calculations employing the stencil rescaling compared to those without. Furthermore as shown for the setups with single tube the results are more accurate in cases where the numerical grid aligns with the tube surface. As expected, the overall permeability is dominated by the largest tube, as we do not see any significant changes within the relative error of the computed permeability.

4.5.3 Newtonian flow through simple cubic (SC) sphere packs

In order to verify the code for more complex geometries as the vertical tube, we here consider simple cubic (SC) sphere packs. Sphere packs provide a geometry for

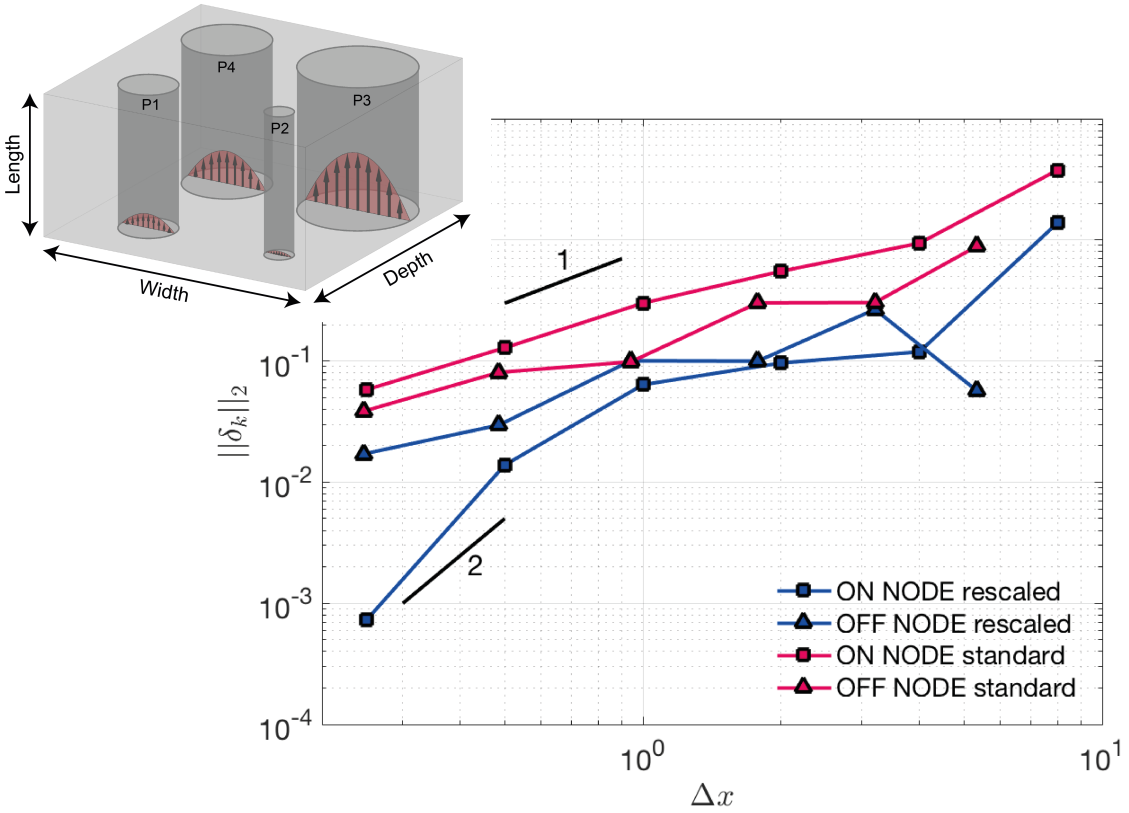

Figure 4.4: Multiple tube Hagen-Poiseuille benchmark. Lines and symbols correspond to the same cases as in Fig. 4.3. To highlight convergence black lines with given slopes were added.

different packings as the porous medium is homogeneous. The setup has dimensions of 2 in all directions.

The permeability of an SC sphere pack is given by (Sangani and Acrivos, 1982; Bear, 1988):

$$k = \frac{\phi^3 \cdot d_{sp}^2}{180 \cdot (1-\phi)^2}, \tag{79}$$

where d_{sp} is the sphere diameter and ϕ is the porosity for simple cubic packing of $1 - \frac{\pi}{6} \approx 0.476$, respectively.

Figure 4.5 shows the increase in accuracy with increasing number of grid points employed. The presented relative errors of the permeability value are computed in the same manner as shown in eq. (74). The simulations employing stencil rescaling show a better convergence and seem to saturate against an relative error of 10^{-1}, demonstrating the influence of boundary effects through applied no-slip boundary conditions (finite size effect).

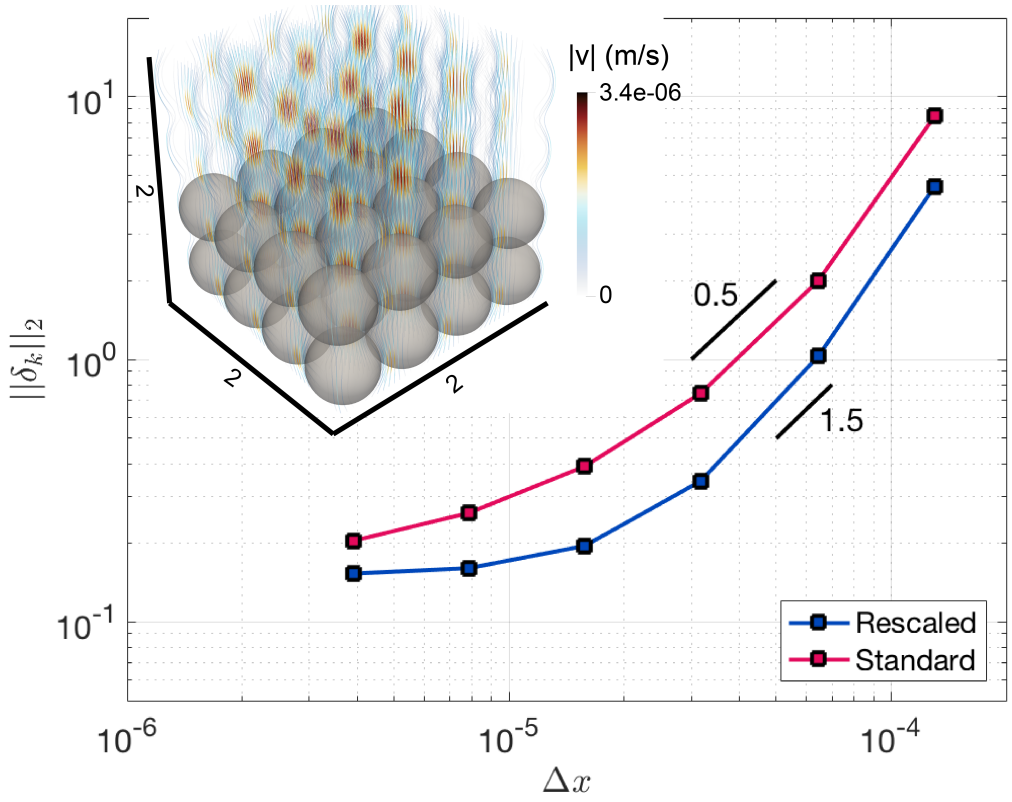

Figure 4.5: Computed $||\delta_k||_2$ norm of the misfit between analytically and numerically computed permeabilities. The inset shows the discretization using 4 spheres in each direction (64 spheres in total). Streamlines are computed around those spheres and colorized with the computed velocity. Blue dots show results using stencil rescaling and red dots results with the standard method. To highlight convergence black lines with given slopes were added.

4.5.4 Power law fluid flow through a single vertical tube

In order to verify the computed value we compare this setup against an analytical solution of Hagen-Poiseuille flow with power law fluid behaviour. For the single tube configuration described in Section 4.5.1 and a power law rheology, the velocity within the tube is given by (e.g. Turcotte and Schubert, 2002):

$$v_z(r) = \frac{C_1}{\frac{1}{n}+1} \cdot \left(\frac{\Delta P}{L}\right)^{\frac{1}{n}} \cdot \left(\left[\frac{R}{2}\right]^{\frac{1}{n}+1} - r^{\frac{1}{n}+1}\right), \tag{80}$$

where $C_1 = 2\eta_0^{-\frac{1}{n}}$ (see Appendix 4.8.2), R is the tube radius and r the width of the tube in Cartesian coordinates. Figure 4.6 shows a good agreement between the numerical and analytical velocities for non-Newtonian fluids when using 0.5 and 2 as values for the power law exponents, covering most fluids used for enhanced oil recovery (e.g. Najafi et al., 2017; Xie et al., 2018).

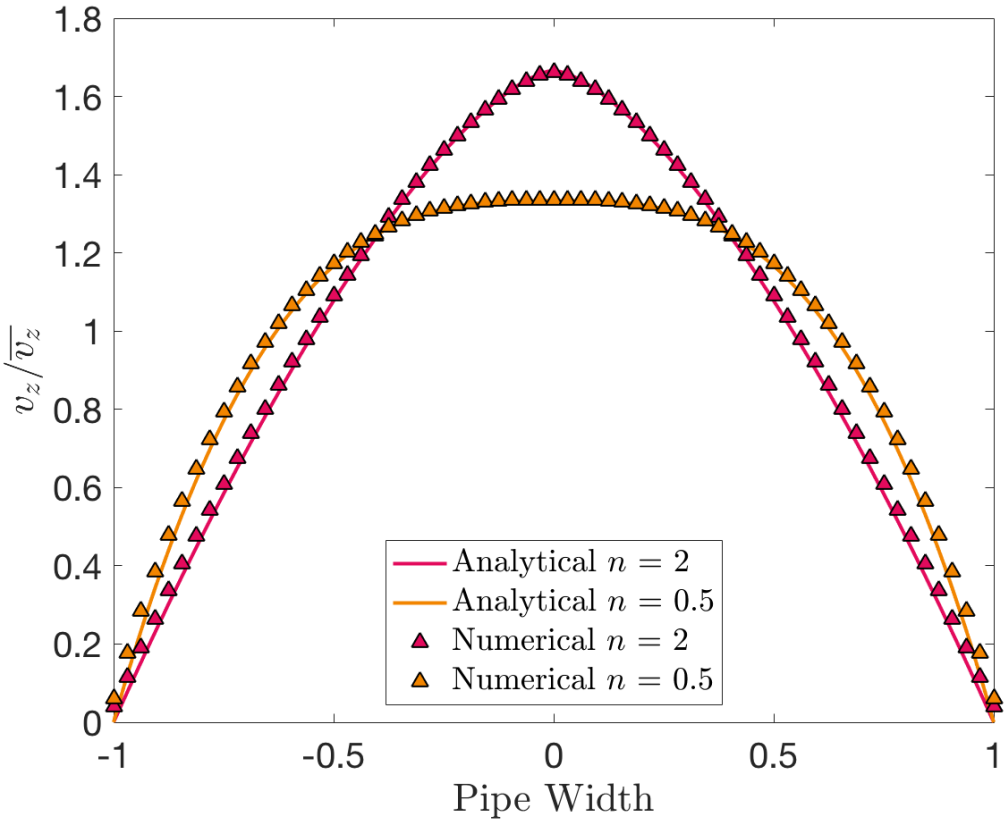

Figure 4.6: Comparison of analytical and numerical velocities for Hagen-Poiseuille flow with a power law fluid. Analytical velocities are represented as colored lines and numerical velocities as colored symbols.

4.6 Application to Fontainebleau sandstone

To verify the ability of the code to handle more complex flows through natural samples and to validate previously computed permeability values we used the CT data for a Fontainebleau sandstone sample provided by Andrä et al. (2013b) with dimensions 2.16 mm × 2.16 mm × 2.25 mm (resolved with 288×288×300 grid points). In order to optimize the computation and reduce computational resources a subsample with dimensions of 256^3 is used for further computations. The sample mainly consists of monodisperse quartz sand grains and is therefore a very popular sample for numerical and experimental permeability measurements. Furthermore sandstone is known to be an ideal reservoir rock and is of certain interest for several geological fields, especially in exploration geology. Laboratory measurements of the given sample with porosity ≈ 15.2 % result in a permeability value of ≈ 1100 mD (Keehm, 2003).

4.6.1 Newtonian flow

As in previous tests we compute the permeability of the extracted subsample using eqs. (59) and (60). Figure 4.7a shows streamlines colored using computed fluid velocities and Fig. 4.7b the local pressure. For a resolution of 256^3, we obtain permeabilities which are comparable to previously computed permeabilities of the same sample (Fig. 4.8, Andrä et al., 2013b), with the rescaled stencil method yielding significantly lower values at higher resolutions. As previous tests show, permeabilities may be overestimated at lower resolutions. To test this effect, we increased the resolution of the Fontainebleau subsample by a factor of 2, 3 and 4 (512^3,768^3,1024^3). The resolution increase is achieved by subdividing a voxel into 2,3 or 4 voxels. We do not apply any interpolation or stochastic reconstructions to conserve spacial statistics as discussed by Karsanina and Gerke (2018). Determining the effects of these more sophisticated methods on computed permeabilities will require further work in the future. Figure 4.8 shows a comparison between the computed and measured values for the given Fontainebleau dataset. With increasing resolution of the subsample the computed permeability value converges to the laboratory value. In comparison to the initial resolution of 256^3 the computed permeability values decreased by $\approx 24.6\,\%$ when using a grid resolution of 1024^3. Additionally the benefit of stencil rescaling can also be seen here, as e.g. the simulation with a resolution of 512^3 and stencil rescaling predicts nearly the same permeability as the case with doubled resolution and no stencil rescaling. Clearly, the models converge to a value that is close to the measured value. The numerical convergence is computed for several subsamples (see Appendix 4.8.3). Figure 4.8 shows the convergence of a single subsample. Previous studies have also observed this convergence with increasing resolution, albeit not always from above (e.g. Zakirov and Galeev, 2019). Similar

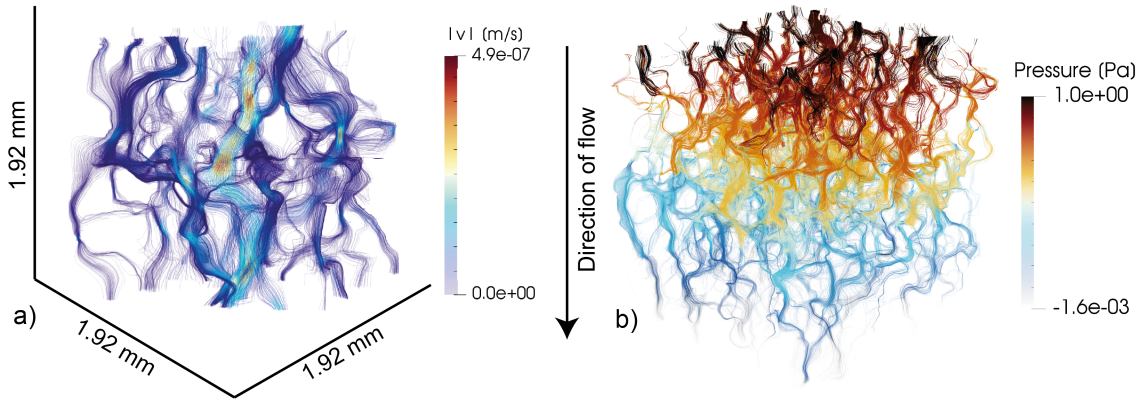

Figure 4.7: Newtonian fluid flow through the Fontainebleau sandstone sample. Streamlines colored using computed fluid velocities are shown in **a)** and streamlines colored using fluid pressures are shown in **b)**.

behaviour has also been observed in LBM simulations (e.g Khirevich et al., 2015; Khirevich and Patzek, 2018).

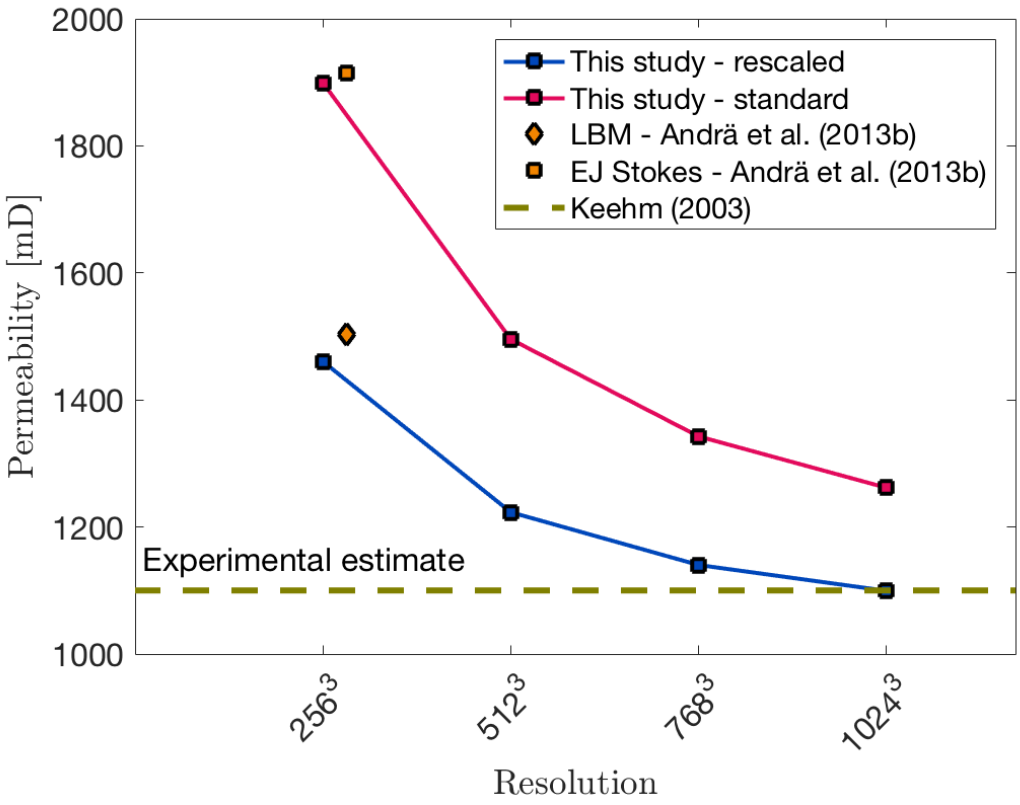

Figure 4.8: Computed permeability values against grid resolution. Orange symbols denote simulations using Lattice-Boltzmann method (LBM) and explicit jump stokes (EJ Stokes), both methods are used in (Andrä et al., 2013b). Blue data points represent simulations using stencil rescaling, while simulations represented by red dots use the standard method. Brown dotted line symbolizes the experimental estimate from Keehm (2003).

4.6.2 Power law fluid flow

To demonstrate the capability of the code to compute the flow of non-Newtonian fluids through porous media, we computed the average flow velocity v_m for a square subsample of the Fontainebleau sandstone sample described above using the power-law rheology given in eq. (62). The edge length of the subsample was 1.92 mm, which corresponds to a CT resolution of 256^3 voxels. To increase accuracy, we increased this resolution by a factor of 2 to a resolution 512^3. As seen in the Section 4.6.1, results at this resolution may overestimate the actual permeability value. The chosen resolution thus represents a compromise between accuracy and computational cost. The reference viscosity was set to $\eta_0 = 1$ Pas and η_1 and η_2 were set to 10^{-3} and 10^6 respectively. Two sets of simulations using a power law exponent of 0.5 and 1 were performed. In each set the applied pressure at the top boundary is

changed from 1 - 16 Pa. In Fig. 4.9 we plot the applied pressure at the top boundary against the computed average velocity. For both sets of simulations the computed slopes of $(19982 \pm 9) \times 10^{-4}$ and $(1000009 \pm 3) \times 10^{-6}$ are in good agreement with the imposed power law coefficients of 0.5 and 1 (eq. (63)).

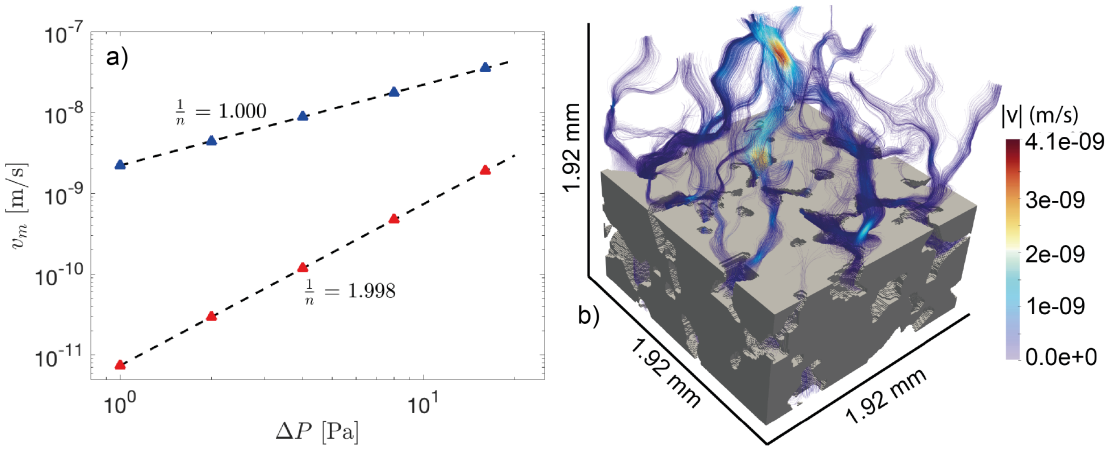

Figure 4.9: Computed results for the Fontainebleau sample using non-Newtonian rheology. **a)** shows the mean velocity against the applied pressure at the top boundary. Red and blue triangles symbolize each simulation and the corresponding dotted black line represents the fitted curve through the obtained data with slope $\frac{1}{n}$. **b)** illustrates computed streamlines of the Fontainebleau subsample using a power law coefficient of 0.5. Solid material is displayed in grey and the streamlines are colored according to computed velocities.

4.7 Discussion and conclusion

In this paper, we presented the capability of the open-source finite difference solver LaMEM to compute the permeability of given porous media. The code was verified using a set of benchmark problems with given analytical solutions ranging from Hagen-Poiseuille flow through vertical tubes to more complex flow through simple cubic sphere packs. Using CT Data of a Fontainebleau sandstone, we then demonstrated that the code is able to predict the permeability of natural porous media. In both benchmarks and application tests, the benefits of the stencil rescaling method can be observed, as this method provides significantly more accurate results at no additional computational cost.

Benchmarking results for single and multiple tubes demonstrate that the permeability calculation improves considerably in case the fluid-solid interface and the numerical grid are at least partially aligned. Cases using the stencil rescaling solutions with a velocity change on a computational node produce smaller relative errors.

Similar to studies using the Lattice-Boltzmann method (LBM) (Knackstedt and X. Zhang, 1994; D. Zhang et al., 2000; Keehm, 2003) our resolution test for the Fon-

tainebleau subsample shows that the computed permeability value also decreases with increasing grid resolution. For instance, computing the permeability of Fontainebleau sandstone sample with grid resolution of 1024^3, calculations employing stencil rescaling give approximately the same permeability value as suggested by laboratory measurements, while simulations without employing stencil rescaling overestimate the computed permeability by $\approx 14.72\,\%$. (Fig. 4.8). However, this behaviour may also be the opposite depending on the numerical implementation of the respective numerical method (e.g. Khirevich et al., 2015; Khirevich and Patzek, 2018; Zakirov and Galeev, 2019).

The computation of permeabilities in a three dimensional pore space using micro-CT data strongly depends on a reasonable quality of the micro-CT images followed by several steps of segmentation in order to resolve tiny fluid pathways. Although high quality input data is required in most cases, it is usually computationally expensive to use the entire micro-CT scan with full resolution; thus, representative subvolumes or a reduced numerical resolution has to be used as computational resources are limited.

Additionally, the segmentation of the CT data has a considerable effect on the computed permeability as discussed in Andrä et al. (2013a), since segmentation of the acquired micro-CT data has a major effect on the three dimensional pore space and therefore on the obtained value. In two phase systems (fluid/solid), segmentation is straightforward whereas it may become more difficult in multiphase systems. All of the above points are a source of uncertainty and need to be considered when comparing numerical calculations to laboratory measurements for rock samples. Furthermore we showed that LaMEM is able to compute non-Newtonian fluid flow in porous media, which is not only relevant for geosciences but also of importance for industrial applications (Saidur et al., 2011).

Furthermore it should be kept in mind that solver options like convergence criteria may influence the obtained permeability result. Figure 4.10 (see Appendix 4.8.1) highlights the effect of different relative tolerances on the computed permeability value. In order to avoid spurious results, we recommend to test the influence of the relative and absolute tolerance on the model outcome.

The simulations were performed on the clusters of University of Bayreuth and University of Mainz using different amount of CPUs depending on the size of the computed domain. As an example a simulation with 512^3 voxels uses 1024 CPUs, 185 GB RAM and requires 5790 s computation time. Apart from LaMEM finite difference codes like FDMSS (Gerke et al., 2018) compute permeability of porous media more

efficient, but these codes mostly are not able to compute fluid flow using non-linear viscosity.

In conclusion the capability of the open-source finite difference solver LaMEM to accurately simulate Newtonian and non-Newtonian fluid flow in porous media is successfully demonstrated for different setups with an increasing geometric complexity including pipe flow, ordered sphere packs and a micro-CT dataset of Fontainebleau sandstone.

Acknowledgements

This work has been funded by DFG project International Research Training Group 2156 (IRTG) Deep Earth Volatile Cycles and by BMBF GEON project PERMEA. M.T. has received funding from the Bayerisches Geoinstitut Visitors Program. Simulations were performed on the btrzx2 cluster, University of Bayreuth and the Mogon II cluster, Johannes Gutenberg University, Mainz. We would like to thank Kirill Gerke and Stéphane Beaussier for their constructive reviews that helped to improve the manuscript.

4.8 Appendix

4.8.1 Convergence criteria

To determine whether a numerical solution converges, two convergence criteria are used, which are absolute and relative convergence tolerance. To test the effect on the numerical solution we varied both while computing permeability of three different setups. Our results show that the obtained permeability value saturates for relative convergence tolerances $< 10^{-7}$. Thus for all further simulations a relative convergence tolerance of 10^{-8} is used (Fig. 4.10). A change in the absolute convergence tolerance did not have any effect on the computed solution, therefore we use a absolute convergence tolerance of 10^{-10}.

4.8.2 Definition of C_1

C_1 is an constant arising during the derivation of eq. (80), which is related to the nonlinear rheology used in Turcotte and Schubert (2002). This rheology is written as:

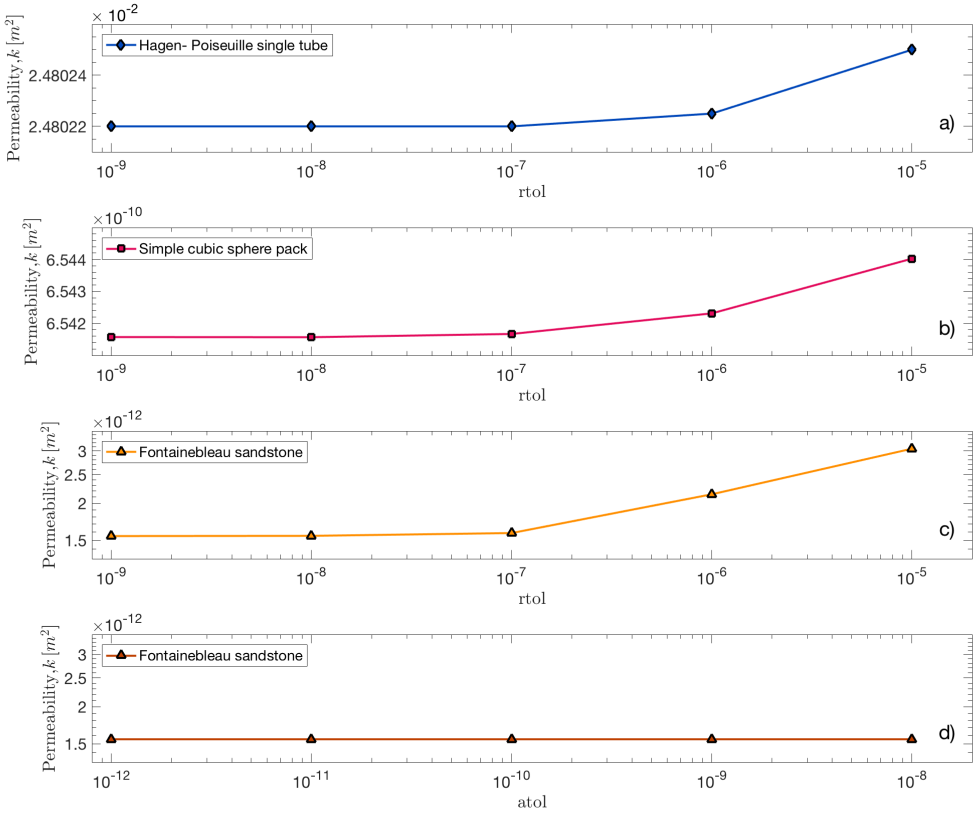

Figure 4.10: Results of simulations for **a)** Hagen-Poiseuille single tube, **b)** simple cubic sphere pack and **c)**+**d)** Fontainebleau sandstone using different relative/absolute convergence tolerances.

$$\dot{\epsilon} = C_1 \tau^{n'}, \tag{81}$$

where n' is the stress exponent as used for power law materials in geodynamics. Replacing τ with $\tau = 2\eta\dot{\epsilon}$ leads to:

$$\dot{\epsilon} = C_1 (2\eta\dot{\epsilon})^{n'}. \tag{82}$$

Solving eq. (82) for η results in:

$$\eta = \frac{1}{2} C_1^{-\frac{1}{n'}} \dot{\epsilon}^{\frac{1}{n'}-1}. \tag{83}$$

We can now define a reference viscosity η_0 at a reference strain rate $\dot{\varepsilon}_0$. This reference viscosity then reads as:

$$\eta_0 = \frac{1}{2} C_1^{-\frac{1}{n'}} \dot{\epsilon}_0^{\frac{1}{n'}-1}. \tag{84}$$

Assuming $\dot{\epsilon_0} = 1$ and solving for C_1 then provides us with the following expression:

$$C_1 = 2\eta_0^{-n'} = 2\eta_0^{-\frac{1}{n}}. \tag{85}$$

4.8.3 Permeabilities of different Fontainebleau subsamples

In order to show numerical convergence of the given Fontainebleau sample several subsamples were extracted and the resolution increased to 512^3, 768^3 and 1024^3 grid points. Figure 4.11 displays the convergence with increasing grid resolution. The different subsamples show a variance of around 12 % for the computed permeability value.

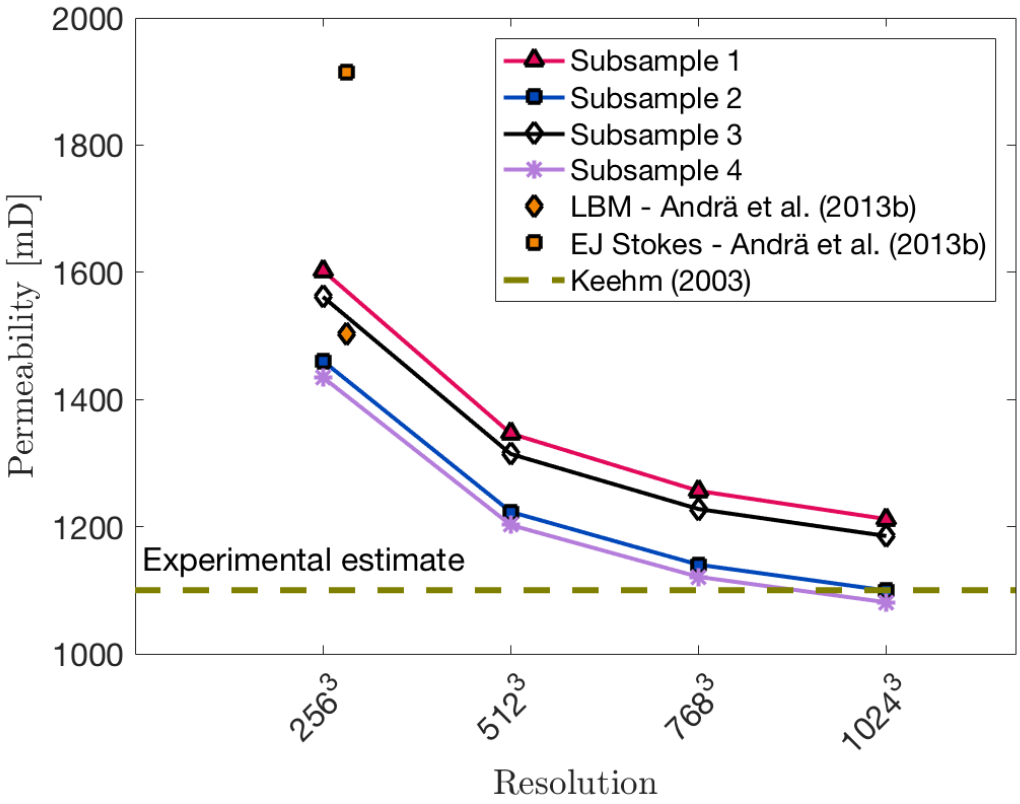

Figure 4.11: Numerical convergence of different Fontainebleau subsamples with increasing grid resolution. All subsamples displayed were computed using stencil rescaling. For comparison the computed permeabilities from Andrä et al. (2013b) are shown. The dotted brown line symbolizes the experimental estimate taken from Keehm (2003).

References

Aharonov, E. & Rothman, D. H. (1993). Non-Newtonian flow (through porous media): A lattice-Boltzmann method. *Geophysical Research Letters*, *20*(8), 679–682. doi:10.1007/s11242-009-9400-7

Akanji, L. T. & Matthai, S. K. (2010). Finite element-based characterization of pore-scale geometry and its impact on fluid flow. *Transport in Porous Media*, *81*(2), 241–259. doi:10.1007/s11242-009-9400-7

Andrä, H., Combaret, N., Dvorkin, J., Glatt, E., Han, J., Kabel, M., ... Zhan, X. (2013a). Digital rock physics benchmarks—Part I: Imaging and segmentation. *Computers & Geosciences*, *50*, 25–32. doi:https://doi.org/10.1016/j.cageo.2012.09.005

Andrä, H., Combaret, N., Dvorkin, J., Glatt, E., Han, J., Kabel, M., ... Zhan, X. (2013b). Digital rock physics benchmarks—Part II: Computing effective properties. *Computers & Geosciences*, *50*, 33–43. doi:https://doi.org/10.1016/j.cageo.2012.09.008

Arns, C. H. (2004). A comparison of pore size distributions derived by NMR and X-ray-CT techniques. *Physica A: Statistical Mechanics and its Applications*, *339*(1-2), 159–165. doi:10.1016/j.physa.2004.03.033

Arns, C. H., Knackstedt, M. A., Pinczewski, M. V. & Lindquist, W. (2001). Accurate estimation of transport properties from microtomographic images. *Geophysical Research Letters*, *28*(17), 3361–3364. doi:10.1029/2001GL012987

Balay, S., Buschelman, K., Eijkhout, V., Gropp, W., Kaushik, D., Knepley, M., ... Zhang, H. (2010). PETSc Users Manual. *ReVision*, *2*, 1–211.

Bear, J. (1988). *Dynamics of fluids in porous media*. New York: Dover Publications Inc.

Bird, M., Butler, S. L., Hawkes, C. & Kotzer, T. (2014). Numerical modeling of fluid and electrical currents through geometries based on synchrotron X-ray tomographic images of reservoir rocks using Avizo and COMSOL. *Computers & Geosciences*, *73*, 6–16. doi:10.1016/j.cageo.2014.08.009

Bird, R., Stewart, W. & Lightfoot, E. (2006). *Transport Phenomena*. Revised second Edition. New York, London: Wiley.

Bosl, W. J., Dvorkin, J. & Nur, A. (1998). A study of porosity and permeability using a lattice Boltzmann simulation. *Geophysical Research Letters*, *25*(9), 1475–1478. doi:10.1029/98GL00859

Brace, W. F. (1980). Permeability of crystalline and argillaceous rocks. *International Journal of Rock Mechanics and Mining Sciences & Geomechanics Abstracts*, *17*(5), 241–251. doi:10.1016/0148-9062(80)90807-4

Brace, W. F. (1984). Permeability of crystalline rocks: New in situ measurements. *Journal of Geophysical Research: Solid Earth*, *89*(B6), 4327–4330. doi:10.1029/JB089iB06p04327

Carman, P. C. (1937). Fluid flow through granular beds. *Transactions, Institution of Chemical Engineers*, *15*, 150–166.

Carman, P. C. (1956). *Flow of gases through porous media*. New York: Academic Press.

Cassidy, M., Manga, M., Cashman, K. & Bachmann, O. (2018). Controls on explosive-effusive volcanic eruption styles. *Nature Communications*, *9*(1), 1–16.

Choi, S. U. (2009). Nanofluids: From vision to reality through research. *Journal of Heat Transfer*, *131*(3), 033106. doi:10.1115/1.3056479

Cui, X., Bustin, A. & Bustin, R. M. (2009). Measurements of gas permeability and diffusivity of tight reservoir rocks: different approaches and their applications. *Geofluids*, *9*(3), 208–223. doi:10.1111/j.1468-8123.2009.00244.x

Deubelbeiss, Y., Kaus, B. J. P., Connolly, J. A. D. & Caricchi, L. (2011). Potential causes for the non-Newtonian rheology of crystal-bearing magmas. *Geochemistry, Geophysics, Geosystems*, *12*(5). doi:10.1029/2010GC003316

Diersch, H.-J. G. (2013). *FEFLOW: Finite Element Modeling of Flow, Mass and Heat Transport in Porous and Fractured Media*. Berlin, Heidelberg: Springer Verlag. doi:10.1007/978-3-642-38739-5

Dikinya, O., Hinz, C. & Aylmore, G. (2008). Decrease in hydraulic conductivity and particle release associated with self-filtration in saturated soil columns. *Geoderma*, *146*(1-2), 192–200. doi:10.1016/j.geoderma.2008.05.014

Dvorkin, J., Derzhi, N., Diaz, E. & Fang, Q. (2011). Relevance of computational rock physics. *Geophysics*, *76*(5), E141–E153. doi:10.1190/geo2010-0352.1

Fedorenko, R. P. (1964). The speed of convergence of one iterative process. *Journal of Computational Mathematics and Mathematical Physics*, *4*, 227–35.

Fehn, U. & Cathles, L. M. (1979). Hydrothermal convection at slow-spreading mid-ocean ridges. *Tectonophysics*, *55*(1-2), 239–260. doi:10.1016/0040-1951(79)90343-3

Ferland, P., Guittard, D. & Trochu, F. (1996). Concurrent methods for permeability measurement in resin transfer molding. *Polymer Composites*, *17*(1), 149–158. doi:10.1002/pc.10600

Ferréol, B. & Rothman, D. H. (1995). Lattice-Boltzmann simulations of flow through Fontainebleau sandstone. *Multiphase flow in porous media*, *20*(1-2), 3–20. doi:10.1007/BF00616923

Fredrich, J., Greaves, K. & Martin, J. (1993). Pore geometry and transport properties of Fontainebleau sandstone. *International Journal of Rock Mechanics and Mining Sciences & Geomechanics Abstracts*, *30*(7), 691–697.

Garcia, X., Akanji, L. T., Blunt, M. J., Matthai, S. K. & Latham, J. P. (2009). Numerical study of the effects of particle shape and polydispersity on permeability. *Physical Review E*, *80*(2), 021304. doi:10.1103/PhysRevE.80.021304

Gerke, K. M., Sidle, R. C. & Mallants, D. (2015). Preferential flow mechanisms identified from staining experiments in forested hillslopes. *Hydrological Processes*, *29*(21), 4562–4578. doi:10.1002/hyp.10468

Gerke, K. M., Vasilyev, R. V., Khirevich, S., Collins, D., Karsanina, M. V., Sizonenko, T. O., ... Mallants, D. (2018). Finite-difference method Stokes solver (FDMSS) for 3D pore geometries: Software development, validation and case studies. *Computers & Geosciences*, *114*, 41–58. doi:10.1016/j.cageo.2018.01.005

Glazner, A. F. (2014). Magmatic life at low Reynolds number. *Geology*, *42*(11), 935–938. doi:10.1130/G36078.1

Guo, Z. & Zhao, T. S. (2002). Lattice Boltzmann model for incompressible flows through porous media. *Physical Review E*, *66*(3), 036304. doi:10.1103/PhysRevE.66.036304

Harlow, F. H. & Welch, J. E. (1965). Numerical Calculation of Time-Dependent Viscous Incompressible Flow of Fluid with Free Surface. *The Physics of Fluids*, *8*(12), 2182–2189. doi:10.1063/1.1761178

Huang, Y., Yang, Z., He, Y. & Wang, X. (2013). An overview on nonlinear porous flow in low permeability porous media. *Theoretical and Applied Mechanics Letters*, *3*(2), 022001. doi:10.1063/2.1302201

Johnston, B. M., Johnston, P. R., Corney, S. & Kilpatrick, D. (2004). Non-Newtonian blood flow in human right coronary arteries: steady state simulations. *Journal of Biomechanics*, *37*(5), 709–720. doi:10.1016/j.jbiomech.2003.09.016

Karsanina, M. V. & Gerke, K. M. (2018). Hierarchical Optimization: Fast and Robust Multiscale Stochastic Reconstructions with Rescaled Correlation Functions. *Physical Review Letters*, *121*(26), 265501. doi:10.1103/PhysRevLett.121.265501

Kaus, B. J. P., Popov, A. A., Baumann, T. S., Püsök, A. E., Bauville, A., Fernandez, N. & Collignon, M. (2016). Forward and Inverse Modelling of Lithospheric Deformation on Geological Timescales. *NIC Series*, *48*, 299–307.

Keehm, Y. (2003). *Computational rock physics: Transport properties in porous media and applications* (Doctoral dissertation, Stanford University).

Khirevich, S., Ginzburg, I. & Tallarek, U. (2015). Coarse- and fine-grid numerical behavior of MRT/TRT lattice-Boltzmann schemes in regular and random sphere packings. *Journal of Computational Physics*, *281*, 708–742. doi:10.1016/j.jcp.2014.10.038

Khirevich, S. & Patzek, T. W. (2018). Behavior of numerical error in pore-scale lattice Boltzmann simulations with simple bounce-back rule: Analysis and highly accurate extrapolation. *Physics of Fluids*, *30*(9), 093604. doi:10.1063/1.5042229

Knackstedt, M. A. & Zhang, X. (1994). Direct evaluation of length scales and structural parameters associated with flow in porous media. *Physical Review E*, *50*(3), 2134–2138. doi:10.1103/PhysRevE.50.2134

Knackstedt, M. A., Latham, S., Madadi, M., Sheppard, A., Varslot, T. & Arns, C. (2009). Digital rock physics: 3D imaging of core material and correlations to acoustic and flow properties. *The Leading Edge*, *28*(1), 28–33. doi:10.1190/1.3064143

Kozeny, J. (1927). Über kapillare Leitung des Wassers im Boden. *Royal Academy of Science, Vienna, Proc. Class I*, *136*, 271–306.

Landau, L. D. & Lifshitz, E. M. (1987). *Course of theoretical physics. vol. 6: Fluid mechanics*. Pergamon Press.

Larson, R. G. (1981). Derivation of generalized Darcy equations for creeping flow in porous media. *Industrial & Engineering Chemistry Fundamentals*, *20*(2), 132–137. doi:10.1021/i100002a003

Mader, H. M., Llewellin, E. W. & Mueller, S. P. (2013). The rheology of two-phase magmas: A review and analysis. *Journal of Volcanology and Geothermal Research*, *257*, 135–158. doi:10.1016/j.jvolgeores.2013.02.014

Manwart, C., Aaltosalmi, U., Koponen, A., Hilfer, R. & Timonen, J. (2002). Lattice-Boltzmann and finite-difference simulations for the permeability for three-dimensional porous media. *Physical Review E*, *66*(1), 016702. doi:10.1103/PhysRevE.66.016702

Mavko, G. & Nur, A. (1997). The effect of a percolation threshold in the Kozeny-Carman relation. *Geophysics*, *62*(5), 1480–1482. doi:10.1190/1.1444251

Mostaghimi, P., Blunt, M. J. & Bijeljic, B. (2013). Computations of Absolute Permeability on Micro-CT Images. *Mathematical Geosciences*, *45*(1), 103–125. doi:10.1007/s11004-012-9431-4

Najafi, S. A. S., Kamranfar, P., Madani, M., Shadadeh, M. & Jamialahmadi, M. (2017). Experimental and theoretical investigation of CTAB microemulsion

viscosity in the chemical enhanced oil recovery process. *Journal of Molecular Liquids*, *232*, 382–389. doi:10.1016/j.molliq.2017.02.092

Norton, D. & Taylor Jr, H. P. (1979). Quantitative Simulation of the Hydrothermal Systems of Crystallizing Magmas on the Basis of Transport Theory and Oxygen Isotope Data: An analysis of the Skaergaard intrusion. *Journal of Petrology*, *20*(3), 421–486. doi:10.1093/petrology/20.3.421

Osorno, M., Uribe, D., Ruiz, O. E. & Steeb, H. (2015). Finite difference calculations of permeability in large domains in a wide porosity range. *Archive of Applied Mechanics*, *85*(8), 1043–1054. doi:10.1007/s00419-015-1025-4

Pan, C., Hilpert, M. & Miller, C. T. (2004). Lattice-Boltzmann simulation of two-phase flow in porous media. *Water Resources Research*, *40*(1). doi:10.1029/2003WR002120

Poiseuille, J. L. (1846). Experimental research on the movement of liquids in tubes of very small diameters. *Mémoires presentés par divers savants a l'Académie Royale des Sciences de l'Institut de France, IX*, 433–544.

Sahimi, M. & Yortsos, Y. C. (1990). Applications of Fractal Geometry to Porous Media: A Review.

Saidur, R., Leong, K. Y. & Mohammad, H. A. (2011). A review on applications and challenges of nanofluids. *Renewable and Sustainable Energy Reviews*, *15*(3), 1646–1668. doi:10.1016/j.rser.2010.11.035

Sangani, A. S. & Acrivos, A. (1982). Slow flow through a periodic array of spheres. *International Journal of Multiphase Flow*, *8*(4), 343–360. doi:10.1016/0301-9322(82)90047-7

Saxena, N. & Mavko, G. (2016). Estimating elastic moduli of rocks from thin sections: Digital rock study of 3D properties from 2D images. *Computers & Geosciences*, *88*, 9–21. doi:10.1016/j.cageo.2015.12.008

Saxena, N., Mavko, G., Hofmann, R. & Srisutthiyakorn, N. (2017). Estimating permeability from thin sections without reconstruction: Digital rock study of 3D properties from 2D images. *Computers & Geosciences*, *102*, 79–99. doi:10.1016/j.cageo.2017.02.014

Shabro, V., Kelly, S., Torres-Verdín, C., Sepehrnoori, K. & Revil, A. (2014). Pore-scale modeling of electrical resistivity and permeability in FIB-SEM images of organic mudrock. *Geophysics*, *79*(5), D289–D299. doi:10.1190/geo2014-0141.1

Shah, C. & Yortsos, Y. C. (1995). Aspects of flow of power-law fluids in porous media. *AIChE Journal*, *41*(5), 1099–1112. doi:10.1002/aic.690410506

Suleimanov, B. A., Ismailov, F. S. & Veliyev, E. F. (2011). Nanofluid for enhanced oil recovery. *Journal of Petroleum Science and Engineering*, *78*(2), 431–437. doi:10.1016/j.petrol.2011.06.014

Turcotte, D. L. & Schubert, G. (2002). *Geodynamics*. New York: Cambridge Univ. Press.

Vakilha, M. & Manzari, M. T. (2008). Modelling of Power-law Fluid Flow Through Porous Media using Smoothed Particle Hydrodynamics. *Transport in Porous Media*, *74*(3), 331–346. doi:10.1007/s11242-007-9199-z

Vasilyev, R. V., Gerke, K. M., Karsanina, M. V. & Korost, D. V. (2016). Solution of the Stokes equation in three-dimensional geometry by the finite-difference method. *Mathematical Models and Computer Simulations*, *8*(1), 63–72. doi:10.1134/S2070048216010105

Wasan, D. T. & Nikolov, A. D. (2003). Spreading of nanofluids on solids. *Nature*, *423*(6936), 156–159. doi:10.1038/nature01591

Wesseling, P. (1995). *Introduction to multigrid methods*. New York: John Wiley & Sons.

Xie, C., Lv, W. & Wang, M. (2018). Shear-thinning or shear-thickening fluid for better EOR?— A direct pore-scale study. *Journal of Petroleum Science and Engineering*, *161*, 683–691. doi:10.1016/j.petrol.2017.11.049

Zakirov, T. & Galeev, A. (2019). Absolute permeability calculations in micro-computed tomography models of sandstones by Navier-Stokes and lattice Boltzmann equations. *International Journal of Heat and Mass Transfer*, *129*, 415–426. doi:10.1016/j.ijheatmasstransfer.2018.09.119

Zeinijahromi, A., Farajzadeh, R., Bruining, J. H. & Bedrikovetsky, P. (2016). Effect of fines migration on oil–water relative permeability during two-phase flow in porous media. *Fuel*, *176*, 222–236. doi:10.1016/j.fuel.2016.02.066

Zhang, D., Zhang, R., Chen, S. & Soll, W. E. (2000). Pore scale study of flow in porous media: Scale dependency, REV, and statistical REV. *Geophysical Research Letters*, *27*(8), 1195–1198. doi:10.1029/1999GL011101

Chapter 5 | Combined numerical and experimental study of microstructure and permeability in porous granular media

Modified version of the paper published in *Solid Earth*: Eichheimer, P., Thielmann, M., Fujita, W., Golabek, G. J., Nakamura, M., Okumura, S., Nakatani, T., and Kottwitz, M. O. (2020): Combined numerical and experimental study of microstructure and permeability in porous granular media, *Solid Earth*, 11, 1079–1095, doi: 10.5194/se-11-1079-2020

5.1 Abstract

Fluid flow on different scales is of interest for several Earth science disciplines like petrophysics, hydrogeology and volcanology. To parameterize fluid flow in large-scale numerical simulations (e.g. groundwater and volcanic systems), flow properties on the microscale need to be considered. For this purpose experimental and numerical investigations of flow through porous media over a wide range of porosities are necessary. In the present study we sinter glass bead media with various porosities and measure the permeability experimentally. The microstructure, namely effective porosity and effective specific surface, is investigated using image processing. We determine flow properties like tortuosity and permeability using numerical simulations. We test different parameterizations for isotropic low porosity media on their potential to predict permeability by comparing their estimations to computed and experimentally measured values.

5.2 Introduction

The understanding of transport and storage of geological fluids in sediments, crust and mantle is of major importance for several Earth science disciplines including volcanology, hydrology and petroleum geoscience (e.g. Manwart et al., 2002; Ramandi et al., 2017; Honarpour, 2018). In volcanic settings melt segregation from partially molten rocks controls the magma chemistry, and outgassing of magmas influences both magma ascent and eruption explosivity (Collinson and Neuberg, 2012; Lamur et al., 2017; Mueller et al., 2005). In hydrogeology fluid flow affects ground water exploitation and protection (Domenico and Schwartz, 1998; Hölting and Coldewey, 2019), whereas in petroleum geoscience it controls oil recovery efficiency (Suleimanov et al., 2011; Hendraningrat et al., 2013; Zhang et al., 2014).

A key parameter for fluid flow is permeability. Permeability estimations have been performed on several scales ranging from pore scale (Brace, 1980) to macroscale (Fehn and Cathles, 1979; Norton and Taylor Jr, 1979; Gleeson and Ingebritsen, 2016). As the permeability on the macroscale is a function of its microstructure it is necessary to accurately predict permeability based on microscale properties (Mostaghimi et al., 2013). To achieve this goal, various experimental and numerical approaches have been developed over the years (e.g. Keehm, 2003; Andrä et al., 2013b; Gerke et al., 2018; Saxena et al., 2017).

Assuming laminar flow (Bear, 1988; Matyka et al., 2008), flow through porous media can be described using Darcy's law (Darcy, 1856), which relates the fluid flux Q to

an applied pressure difference ΔP

$$Q = -\frac{kA\Delta P}{\eta L}, \tag{86}$$

where k is the permeability, A is the cross sectional area, η is the fluid viscosity and L is the length of the domain.

Accurately determining and predicting permeability is thus of crucial importance to quantify fluid fluxes in porous media. Until today it remains challenging to relate permeability to the microstructure of porous media. This has resulted in numerous parameterizations developed for different materials and structures (Kozeny, 1927; Carman, 1937, 1956; Martys et al., 1994; Revil and Cathles III, 1999; Garcia et al., 2009).

A first simple capillary model to predict the permeability of a porous medium was proposed by Kozeny (1927)

$$k = k_0 \frac{\phi^3}{S^2}, \tag{87}$$

where k_0 is the dimensionless Kozeny constant depending on the channel geometry (e.g. $k_0 = 0.5$ for cylindrical capillaries), ϕ is the porosity and S is the specific surface area (ratio of exposed surface area to bulk volume). Later this relation was extended by Carman (1937, 1956), to predict fluid flow through a granular bed with a given microstructure. To account for the effect of the microstructure on fluid flow, Carman (1937, 1956) introduced the term tortuosity, which he defined as the ratio of effective flow path L_e to a straight path L.

$$\tau = \frac{L_e}{L} \tag{88}$$

Introducing this relation into eq. (87) leads to the well-known Kozeny-Carman equation:

$$k = k_0 \frac{\phi^3}{\tau^2 S^2}, \tag{89}$$

Using experimental data, Carman (1956) determined that tortuosity τ is $\approx \sqrt{2}$. Today, the Kozeny-Carman equation - or variants thereof - is widely used in volcanology (Klug and Cashman, 1996; Mueller et al., 2005; Miller et al., 2014), hydrogeology (Wang et al., 2017; Taheri et al., 2017), two-/multi-phase flow studies (Wu et al., 2012; Keller and Katz, 2016; Keller and Suckale, 2019) and soil sciences (Chapuis and Aubertin, 2003; Ren et al., 2016). The Kozeny-Carman equation was derived assuming that the medium consists only of continuous curved channels with constant cross-section (Carman, 1937; Bear, 1988). However, in porous media pathways most likely do not obey these assumptions. Applying this equation to

porous media therefore remains challenging and in some cases fails for low porosities (Bernabe et al., 1982; Bourbie et al., 1992) or mixtures of different shapes and material sizes (Carman, 1937; Wyllie and Gregory, 1955). Consequently, alternative permeability parameterizations have been developed by different authors (Martys et al., 1994; Revil and Cathles III, 1999; Garcia et al., 2009).

Using numerical modeling, Martys et al. (1994) derived a universal scaling law for various overlapping and non-overlapping sphere packings which reads as:

$$k = \frac{2(1-\phi-\phi_c)}{S^2}(\phi-\phi_c)^f, \tag{90}$$

with $f = 4.2$ and ϕ_c being the critical porosity, below which no connected pore space exists. They showed that eq. (90) is valid for a variety of porous media including mono-sized sphere packings, glass bead samples and experimentally measured sandstones. Despite the predictive power of this parameterization it might not give reasonable estimations for permeability in case the porous medium consists of rough surfaces and large isolated regions (voids).

The study of Revil and Cathles III (1999) used electrical parameters to derive the permeability of different types of shaly sands, i.e., the permeability of a clay-free sand and the permeability of a pure shale. By using electrical parameters which separate pore throat from total porosity and effective from total hydraulic radius, Revil and Cathles III (1999) were able to improve the Kozeny-Carman relation, being only dependent on grain size. In a first step the authors developed a model for the permeability of a clay-free sand as a function of the grain diameter, the porosity, and the electrical cementation exponent reading as:

$$\Lambda = \frac{R^2}{2m^2F^3}, \tag{91}$$

with Λ being the effective electrical pore radius, R being the grain radius, m being the cementation exponent and F being the formation factor. Using the relation of the formation factor to porosity by Archie's law $F = \phi^{-m}$ (Waxman and Smits, 1968), $m = 1.8$ (Waxman and Smits, 1968) and $d = 2R$ for the grain diameter the authors derived a permeability parameterization for natural sandstones:

$$k = \frac{d^2\phi^{5.1}}{24}, \tag{92}$$

which is in good agreement with experimentally measured data by Berg (1975).

Based on numerical simulations of fluid flow in polydisperse grain packings with irregular shapes, Garcia et al. (2009) proposed an alternative parameterization by

fitting the numerical results with the following equation:

$$k = \phi^{0.11} D^2, \tag{93}$$

where D^2 is the squared harmonic mean diameter of the grains. They also showed that this parameterization also fits experimental results quite well and concluded that grain shape and size polydispersity have a small but noticeable effect on permeability.

As can been seen from eq. (89),(90),(92),(93) the different parameterizations focus on specific types of porous media and relate different microstructural properties to permeability. While properties such as porosity and mean grain diameter are relatively straightforward to determine, others, such as specific surface and tortuosity, are much harder to access. This is why several parameterizations have been developed to quantify these properties (Comiti and Renaud, 1989; Pech, 1984; Mota et al., 2001; Pape et al., 2005). These studies either use experimental, analytical or numerical approaches for mostly two dimensional porous media with porosities $> 30\%$.

Since the ascent of Digital Rock Physics (DRP), it has become viable to study microstructures of porous media in more detail using micro Computed Tomography (micro-CT) and Nuclear Magnetic Resonance (NMR) images (Arns et al., 2001; Arns, 2004; Dvorkin et al., 2011). Together with numerical models, these images can then be used to compute fluid flow within porous media to determine their permeability. For this purpose several numerical methods including Finite Elements (FEM), Finite Differences (FDM) and Lattice Boltzmann method (LBM) (Saxena et al., 2017; Andrä et al., 2013b; Gerke et al., 2018; Shabro et al., 2014; Manwart et al., 2002; M. Bird et al., 2014) have been used.

Yet, very few data sets exist that systematically investigate microstucture (porosity and specific surface) and related flow parameters (tortuosity and permeability), in particular at porosities $< 30\%$. Most of the previous studies either measure permeability experimentally without investigating its microstructure or compute permeability and related microstructural parameters, that cannot be compared to experimental data sets. To remedy this issue, we here sinter porous glass bead samples with porosities ranging from $1.5\% - 21\%$ and investigate their microstructure using image processing. This porosity range is representative of sedimentary rocks up to a depth of ≈20 km (Bekins and Dreiss, 1992). Permeability is then measured experimentally using a permeameter (see section 5.3.2; Takeuchi et al. (2008) and Okumura et al. (2009)) and numerically using the finite difference code LaMEM (see section 5.3.7; Kaus et al. (2016) and Eichheimer et al. (2019)). The the-

oretical permeability predictions described above in eqs. (89),(90),(92),(93) require microstructural input parameters such as porosity, specific surface and tortuosity. Within this study these parameters are determined and related to porosity. We therefore provide permeability parameterizations depending on porosity only and verify against numerically and experimentally determined values.

5.3 Methods

Here we first describe the experimental workflow including sample sintering and permeability measurement, followed by the numerical workflow featuring image processing, computation of fluid velocities and determination of both tortuosity and permeability. Figure 5.1 shows an overview of the entire workflow which will be explained in detail in the following section.

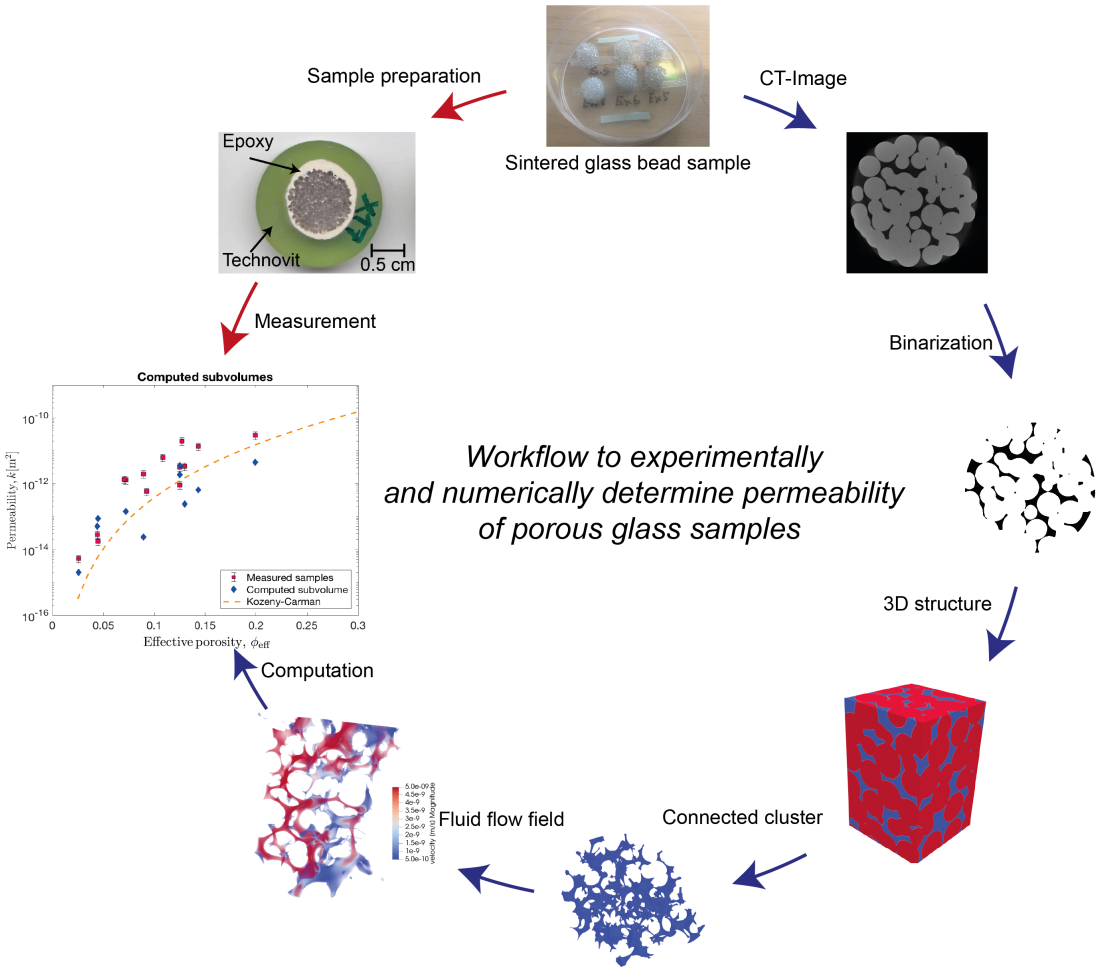

Figure 5.1: Workflow process map - red arrows mark the experimental workflow, whereas blue arrows indicate the numerical workflow.

5.3.1 Sample sintering

Glass bead cylinders with different porosities were sintered under experimental conditions as summarized in Table 5.1. For this purpose soda-lime glass beads with diameters ranging from 0.9 to 1.4 mm were utilized as starting material (see grain size distribution in appendix 5.6.4). For each sample, we prepared a graphite cylinder with 8.0 mm inner diameter and ≈10 mm height. Additional samples with diameters of 10 and 14 mm were prepared to check for size effects (see table 5.1a). At the bottom of the graphite cylinder a graphite disc (11.5 mm diameter and 3.0 mm thick) was attached using a cyanoacrylate adhesive (see Fig. 5.2 inset). The glass beads were poured into the graphite cylinder and compressed with steel rods (8-14 mm diameter) before heating.

The glass bead samples were then sintered in a muffle furnace at 710 °C under atmospheric pressure. The temperature of 710 °C was found to be suitable for sintering of the glass beads as it is slightly below the softening temperature of soda-lime glass around $720 - 730\,^{\circ}\mathrm{C}$ (Napolitano and Hawkins, 1964) and well above the glass transition temperature of soda-lime glass at ≈550 °C (Wadsworth et al., 2014). At 710 °C the viscosity of the employed soda-lime glass is on the order of $10^7\,\mathrm{Pa\,s}$ (Kuczynski, 1949; Napolitano and Hawkins, 1964; Wadsworth et al., 2014) allowing for viscous flow of the glass beads at their contact surface driven by surface tension. Using different time spans ranging from $60 - 600$ minutes the viscous flow at 710 °C controls the resulting porosity of the sample.

After sintering, the sample was cooled down to $550 - 600\,^{\circ}\mathrm{C}$ within ≈5 minutes. Afterwards the sample was taken out of the furnace to adjust to room temperature and prevent thermal cracking of the sample. In a next step the graphite container was removed from the sample. It should be noted that during the process of sintering gravity slightly affects the porosity distribution within the glass bead sample (see Fig. 5.2). However, the subsamples used to compute the numerical permeability do not cover the whole height of the sample, thus the effect of compaction on the results is limited.

5.3.2 Experimental permeability measurement

In a first preparation step we wrap a highly viscous commercial water resistant resin around the sample to avoid pore space infiltration. In a next step we embed the sample within a less viscous resin (Technovit 4071, Heraeus Kulzer GmbH & Co. or Presin, Nichika Inc.) to create an airproof casing. The upper and lower surface of the

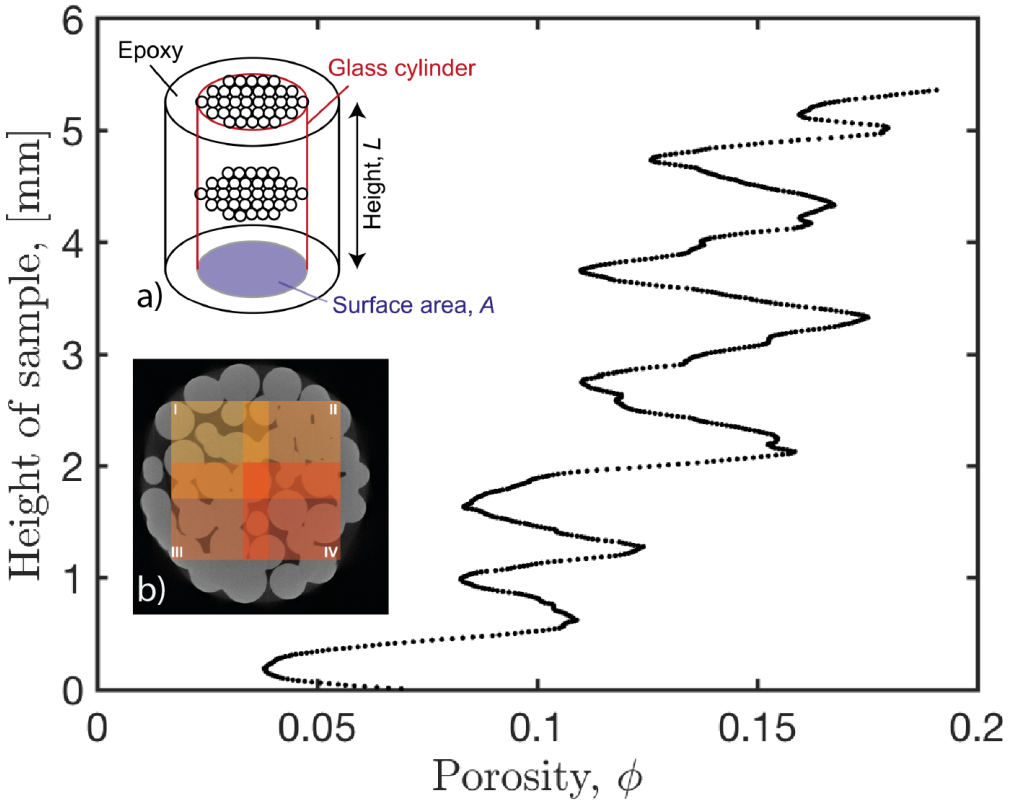

Figure 5.2: Computed porosity of each CT-slice from top to the bottom of a full sample (z-axis; sample Ex14). The diagram shows that gravity affects the porosity of the sample. Porosity minima correspond to distinct layers of glass bead within the sample. The inset **a)** provides a sketch of the sample structure. In the inset the red color outlines the cylindrical shape, blue the surface area A of the cylinder and L the height of the sample. **b)** shows chosen locations for the squared subsamples 1-4. Additional four subsamples (5-8) are placed similarly below subsamples 1-4 overlapping in z-direction.

sample were grinded and polished to prevent leaks during experimental permeability measurements (Fig. 5.1; Sample preparation).

The experimental permeability measurements were conducted at Tohoku University using a permeameter, described in Takeuchi et al. (2008) and Okumura et al. (2009). To determine the permeability the air flow through a sample is measured at room temperature. The pressure gradient between sample inlet and outlet is controlled by a pressure regulator (RP1000-8-04, CKD Co.; Precision $\pm 0.1\,\%$) at the inlet side. To monitor the pressure difference a digital manometer (testo526-s, Testo Inc.; Precision $\pm 0.05\,\%$) is used. Air flow through the sample is measured using a digital flow meter (Alicat, M-10SCCM; Precision $\pm 0.6\%$). As Darcy's law assumes a linear relationship between the pressure and flow rate, we measure the gas flow rate at several pressure gradients (see Fig. 5.8 in Appendix 5.6.3) to verify our assumption of laminar flow conditions. The permeability of all samples is calculated using Darcy's law (eq. (86)) based on measured values (table 5.1a).

a) Experimental parameters							b) Numerical parameters		
Sample	Area A (cm^2)	Height L (mm)	Capsule Ø D (mm)	Time t_{sint} (min)	Tot. weight m (g)	Permeability K_{meas} (m^2)	Porosity ϕ_{tot} (%)	Porosity ϕ_{eff} (%)	Porosity $min(\phi_{eff})$ (%)
X02	0.438	5.11	8	120	0.574	$(3.1 \pm 0.2) \times 10^{-11}$	20.94	20.94	11.38
X11	0.434	3.63	8	180	0.575	$(1.91 \pm 0.09) \times 10^{-14}$	6.72	4.75	1.80
X14	0.407	5.12	8	60	0.576	$(3.4 \pm 0.2) \times 10^{-12}$	13.28	13.22	4.26
X15	0.412	4.76	8	480	0.575	$(5.7 \pm 0.3) \times 10^{-15}$	2.54	1.21	0.96
X16	0.808	5.05	10	120	0.899	$(3.1 \pm 0.2) \times 10^{-14}$	6.07	4.50	2.66
X17	1.569	5.18	14	120	1.762	$(1.41 \pm 0.07) \times 10^{-12}$	12.90	12.85	10.77
X29	0.441	4.55	8	300	0.576	$(6.3 \pm 0.3) \times 10^{-13}$	9.01	8.97	5.95
X30	0.420	4.81	8	600	0.574	$(1.52 \pm 0.08) \times 10^{-12}$	7.12	7.03	4.18
X31	0.423	4.73	8	300	0.576	$(2.1 \pm 0.1) \times 10^{-12}$	9.92	9.87	6.12
X32	0.342	4.47	8	480	0.576	$(3.7 \pm 0.2) \times 10^{-12}$	13.52	13.44	8.93
X33	0.412	4.80	8	180	0.575	$(1.53 \pm 0.08) \times 10^{-11}$	15.97	15.96	11.33
X35	0.411	4.78	8	360	0.575	$(2.2 \pm 0.1) \times 10^{-11}$	14.17	14.15	8.92
X36	0.372	4.15	8	420	0.575	$(6.9 \pm 0.4) \times 10^{-12}$	10.71	10.67	6.78

Table 5.1: **a)** displays experimental parameters of sintering conditions and parameters used to compute permeability using Darcy's law. A denotes the sample surface area, L the height of the glass bead cylinders and D the inner diameter of each capsule. Additionally, the sintering time t_{sint}, the total weight of the glass beads m, and the experimentally measured permeability K_{meas} are given. In **b)**, we list the total, effective and minimum effective porosity ϕ_{tot}, ϕ_{eff}, $\min(\phi_{eff})$ of each sample. These porosities have been obtained with image processing (see section 5.3.4).

5.3.3 Micro-CT images and segmentation

Before preparing the samples for permeability measurements all samples are digitized using micro Computed Tomographic scans (micro-CT) performed at Tohoku University (ScanXmate-D180RSS270) with a resolution $\approx 6 - 10\,\mu$m according to the method of Okumura and Sasaki (2014). Andrä et al. (2013a) showed that the process of segmentation of the micro-CT images may have a significant effect on the three dimensional pore space and therefore the computed flow field. In two-phase systems (fluid + mineral), as in this study, the segmentation is straightforward due to the high contrast in absorption coefficients between glass beads and air, while it can become quite complex for multiphase systems featuring several mineral phases. In the present study the segmentation of the obtained micro-CT images was done using build-in MatLab functions. In a first step the images are binarized using Otsu's method (Otsu, 1979). Additional smoothing steps of the images are performed. In a next step the two dimensional micro-CT slices are stacked on top of each other, resulting in a three dimensional representation of the pore space (Fig. 5.1; 3D structure).

5.3.4 Porosity determination

Porosity is an important parameter describing microstructures. It is defined as the ratio of the total pore space V_V to the bulk volume of the sample V_b (R. Bird et al., 2006):

$$\phi_{\text{tot}} = \frac{V_V}{V_b} \tag{94}$$

In a first step, the total porosity of each sample is determined by counting the amount of solid and fluid voxels. In a second step, we determine the isolated pore space using a flooding algorithm implemented in MatLab (bwconncomp). This isolated pore space is then subtracted from the total pore space to obtain an effective pore space V_{eff}. As a bonus, this procedure reduces the computational cost for numerical permeability determinations by removing the parts of the pore space that do not contribute to fluid flow and thus permeability. The effective porosity ϕ_{eff} is then defined as the volume of all percolating pore space clusters $V_{V_{\text{eff}}}$ to the bulk volume of the sample:

$$\phi_{\text{eff}} = \frac{V_{V_{\text{eff}}}}{V_b} \tag{95}$$

It should be mentioned that in a simple capillary model $\phi_{\text{eff}} = \phi$ since no isolated pore space exists. It should also be noted that only the effective porosity is used to determine microstructural and flow properties later in this study.

As described in section 5.3.2, the porosity of the samples is not homogeneous, but increases towards the sample bottom due to gravity. As permeability may not necessarily be affected by the total porosity, but rather by the minimum effective porosity in a sample (in a slice perpendicular to the flow direction), we also determined the minimum effective porosity of each sample (see table 5.1b).

5.3.5 Effective specific surface

The specific surface is defined as the total interfacial surface area of pores A_s per unit bulk volume V_b of the porous medium (Bear, 1988):

$$S = \frac{A_s}{V_b} \tag{96}$$

As in the previous section we compute the effective specific surface of all percolating pore space clusters and neglect isolated pore space. To determine the effective specific surface we use the extracted connected clusters and compute an isosurface of the entire three dimensional binary matrix. In a next step the area of the resulting isosurface A_s is calculated.

5.3.6 Numerical method

The relationship between inertial and viscous forces in fluid flows is described by the Reynolds number:

$$Re = \frac{\rho v L}{\eta}, \tag{97}$$

where ρ is the density, v the velocity component, L denotes the length of the domain and η is the viscosity of the fluid. For laminar flow conditions ($Re < 1$, see Fig. 5.8 Appendix 5.6.3) and ignoring gravity, the flow in porous media can be described with the incompressible Stokes equations:

$$\frac{\partial v_i}{\partial x_i} = 0 \tag{98}$$

$$\frac{\partial}{\partial x_j}\left[\eta\left(\frac{\partial v_i}{\partial x_j} + \frac{\partial v_j}{\partial x_i}\right)\right] - \frac{\partial P}{\partial x_i} = 0 \tag{99}$$

with P being the pressure and x the spatial coordinate. For all simulations, we employed a fluid viscosity of 1 Pas.

The Stokes equations are solved using the finite difference code LaMEM (Kaus et al., 2016; Eichheimer et al., 2019). LaMEM employs a staggered grid Finite Difference scheme (Harlow and Welch, 1965), where pressures P are defined at the cell centers and velocities v at cell faces. Based on the data from the CT-scans, each cell is assigned either a fluid or a solid phase. The discretized system of equations is then solved using multigrid solvers of the PETSc library (Balay et al., 2019). As only cells within the fluid phase contribute to fluid flow the discretized governing equations are only solved for these cells. This greatly decreases the number of degrees of freedom and therefore significantly reduces the computational cost. Due to computational limitations and the densification at the bottom of the samples (see Fig. 5.2) we extract 8 overlapping subvolumes per full sample (see Fig. 5.2b), with sizes of 512^3 cells. For each subvolume we compute effective porosity, effective specific surface, hydraulic tortuosity and permeability.

5.3.7 Numerical permeability computation

From the calculated velocity field in z-direction the volume-averaged velocity component v_m is calculated (e.g. Osorno et al., 2015):

$$v_m = \frac{1}{V_f}\int_{V_f} |v_z|\, dv, \tag{100}$$

where V_f is the volume of the fluid phase. Using Darcy's law (eq. (86); Andrä et al., 2013b; Bosl et al., 1998; Morais et al., 2009; Saxena et al., 2017) an intrinsic permeability k_s is computed via:

$$k_s = \frac{\eta v_m}{\Delta P} \tag{101}$$

5.3.8 Hydraulic tortuosity

Tortuosity is not only highly relevant for the Kozeny-Carman relation, but is also used in various engineering and science applications (Nemati et al., 2020). It has a major influence on liquid-phase mass transport (e.g. in Li-ion batteries (Thorat et al., 2009) and membranes (Manickam et al., 2014)), the effectiveness of tertiary oil recovery (Azar et al., 2008) and evaporation of water in soils (Hernández-López et al., 2014). In recent years, several definitions for tortuosity have been suggested (Clennell, 1997; Bear, 1988; Ghanbarian et al., 2013). For the remainder of this study we will calculate and apply the so-called hydraulic tortuosity (Ghanbarian et al., 2013). Assuming that hydraulic tortuosity changes with porosity, both numerical and experimental studies published different relations of hydraulic tortuosity to porosity. In most of the cases the hydraulic tortuosity is assumed to be constant as it is difficult to determine experimentally, which is rarely done. It should be mentioned that the following hydraulic tortuosity-porosity relations have been obtained for porous media with $> 30\%$ porosity.

Matyka et al. (2008) numerically determined the hydraulic tortuosity by using an arithmetic mean given as:

$$\tau_h = \frac{1}{N} \sum_{i=1}^{N} \tau(r_i), \tag{102}$$

where $\tau = L_e/L$ is the hydraulic tortuosity of a flow line crossing through point r_i (eq. (88)) and N the total number of streamlines.

Koponen et al. (1996) computed the hydraulic tortuosity numerically using:

$$\tau_h = \frac{\sum_i \tau^n(r_i) v(r_i)}{\sum_i v(r_i)}, \tag{103}$$

where $v(r_i) = |v(r_i)|$ is the fluid velocity at point r_i and points r_i are chosen randomly from the pore space (Koponen et al., 1996).

One of the most common relations for hydraulic tortuosity is a logarithmic function of porosity reading as follows:

$$\tau_h(\phi) = 1 - Bln(\phi), \tag{104}$$

where B is a constant found experimentally for different particles (e.g. 1.6 for wood chips (Pech, 1984; Comiti and Renaud, 1989), 0.86 to 3.2 for plates (Comiti and Renaud, 1989)). By numerically computing hydraulic tortuosity for two dimensional squares, Matyka et al. (2008) obtained $B = 0.77$. A different experimental relation for hydraulic tortuosity measuring the electric conductivity of spherical particles was proposed by Mota et al. (2001):

$$\tau_h(\phi) = \phi^{-0.4} \tag{105}$$

Investigating numerically two-dimensional porous media with rectangular shaped particles Koponen et al. (1996) proposed a different relation:

$$\tau_h(\phi) = 1 + 0.8(1 - \phi) \tag{106}$$

In the present study the hydraulic tortuosity is determined according to eq. (102), which requires to compute the tortuosity τ of individual streamlines within each sample. Streamlines describe a curve traced out in time by a fluid particle with fixed mass and are described mathematically as:

$$\frac{\partial x_i}{\partial t} = v(x, t), \tag{107}$$

with v being the computed velocity field obtained from the numerical simulation and t being the time. Integrating eq. (107) yields

$$x_i = x_i(x^0, t), \tag{108}$$

where x^0 is the position of the prescribed particle at $t = 0$. Eq. (107) is solved using built-in MatLab ODE (Ordinary Differential Equation) solvers. To compute the streamline length all fluid cells at the inlet of the subsample are extracted and used as streamline starting points. Using the computed velocity field and eq. (107) the streamline length for each starting point is calculated. Hence, up to 40000 streamlines need to be computed for a subsample with ≈20% porosity, whereas for a subsample with ≈5% porosity up to 5000 streamlines are computed.

5.4 Results

In this section we analyze the different samples in terms of porosity, specific surface, hydraulic tortuosity and permeability. All data for each subsample presented here are given in the supplementary tables (see table 1 - 13). Effective porosity and effective specific surface are computed for both subsamples and full samples, whereas hydraulic tortuosities and permeabilities are only computed for subsamples due to computational limitations. In the present study we analysed 13 samples and 104 subsamples.

5.4.1 Porosity

The total porosity for each sample and subsample is analysed using image processing and ranges from $2.5 - 21\%$ (see table 5.1b and supplement table 1-13). The effective porosity is determined by extracting all connected clusters within the samples and ranges from $1.21 - 21\%$ (see also table 5.1b). The analysis of the micro CT images also showed that during sintering densification of the samples occurs (see Fig. 5.2). For this reason we furthermore report the minimum effective porosity $min(\phi_{\text{eff}})$. Assuming an effective porosity for the entire sample therefore does not seem to be representative as during the laboratory measurements a first order control mechanism of the fluid flow and therefore permeability is the lowest porosity within the entire sample.

5.4.2 Effective specific surface

Figure 5.3 shows the computed specific surfaces for all subsamples and all full samples with increasing effective porosity. Koponen et al. (1997) used the following relationship to predict the specific surface:

$$S = -\frac{n}{R_0}\phi_{\text{eff}} ln(\phi_{\text{eff}}), \tag{109}$$

where n is the dimensionality and R_0 is the hydraulic radius of the particles. The hydraulic radius is defined as $2V_p/M$ (e.g. Bernabé et al., 2010), with V_p being the pore volume and M being the pore surface area. For a regular simple cubic sphere packing with $\phi = 0.476$ the estimated hydraulic radius is $\approx 151\,\mu$m. To relate the computed values for the effective specific surface to the effective porosity the above

equation is fitted, resulting in a hydraulic radius of 385.09 μm:

$$S = -\frac{3}{3.8509 \times 10^{-4}\, m}\phi_{\text{eff}} ln(\phi_{\text{eff}}) \tag{110}$$

The fit between eq. (109) and our data shows good agreement which is also reflected in a value of R^2=0.975 (see Fig. 5.3).

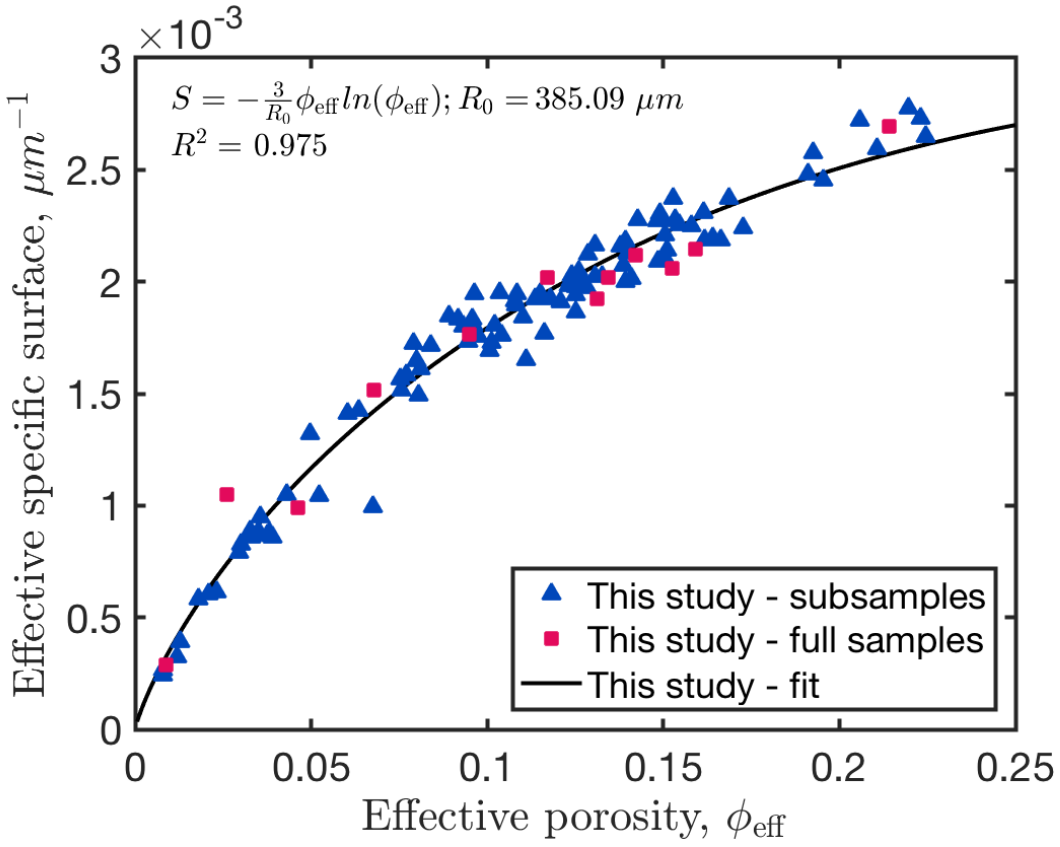

Figure 5.3: Effective specific surface as a function of effective porosity. Blue triangles represent subsample data from this study and red squares the effective specific surface of full samples. Full sample data points are plotted in order to show that in terms of effective specific surface subsamples represent full samples very well. The black curve represents the fitted curve according to eq. (110).

5.4.3 Hydraulic tortuosity

We computed hydraulic tortuosities for all subsamples which exhibit a percolating pore space. Results are shown in Fig. 5.4, where we compare different hydraulic tortuosity-porosity parameterizations presented in section 5.3.8 to our data. In Fig. 5.4a)-c), we compare our data (denoted by grey squares) with one of the three porosity-hydraulic tortuosity parameterizations (denoted by solid and dashed lines), whereas in Fig. 5.4d), we show a simple linear fit to our data. In general, computed hydraulic tortuosities are quite scattered and show variations ranging

from values of about 2 to values of around 4. In Fig. 5.4a) we compare our data to the hydraulic tortuosity parameterization from Matyka et al. (2008) (see eq. (104)), which is denoted by a dashed black line. We refitted this parameterization using our data, with the result shown by the red solid line with corresponding 95% confidence bounds with the coefficient of determination $R^2 = -1.6317$. In Fig. 5.4b) and c), similar comparisons are shown, but for the parameterizations by Koponen et al. (1996) (Fig. 5.4b) and Mota et al. (2001) (Fig. 5.4c). In both cases, we show the original parameterizations as a black dashed line and the fitted parameterizations as a colored solid line with colored dashed lines indicating the 95% confidence bounds. As for the parameterization by Matyka et al. (2008), these two parameterizations do not fit our data very well, as is also indicated by their low R^2 values ($R^2 = -5.6017$ and $R^2 = 0.0758$ respectively). Finally, in Fig. 5.4c), we show a linear fit to our data together with the 95% confidence bounds. As indicated by the low R^2 value of 0.0274, this fit does also not represent the data very well. For this reason we use the arithmetic mean of the computed hydraulic tortuosities for later permeability predictions. Nevertheless, we do observe that despite the large scatter, hydraulic tortuosity largely remains relatively constant with decreasing porosity, thus indicating that the pore distribution of our experimental products is homogeneous and the geometrical similarity of pore structure was kept during sintering. This is in contrast to the parameterizations of Matyka et al. (2008) and Mota et al. (2001), both predicting a significant increase in tortuosity as small porosities are approached, but agrees with the model of Koponen et al. (1996).

5.4.4 Permeability

In Fig. 5.5, measured permeabilities for all samples are shown as grey symbols (see also table 5.1a for measured values). We here chose to plot sample permeabilities vs. the minimum of the effective porosity, the reason being the intrinsic porosity variations in each sample (see section 5.3.4). Figure 5.6 in the appendix shows both the effective porosity and minimum effective porosity of each sample.

Measured permeabilites range from values of around 10^{-14} m^2 to about 10^{-11} m^2, depending on porosity. Although experimental measurements are scattered, a clear trend can be observed. At porosities close to the critical porosity, permeabilities are very low, but rapidly increase when porosities increase slightly. At larger porosities, permeabilities further increase, but this increase is significantly less rapid.

Numerically 98 subsamples have been computed successfully with permeabilities ranging from around 10^{-14} m^2 to about 10^{-10} m^2, depending on porosity (see table 1-13 in the supplement and Fig. 5.7 in the appendix). In comparison to the ex-

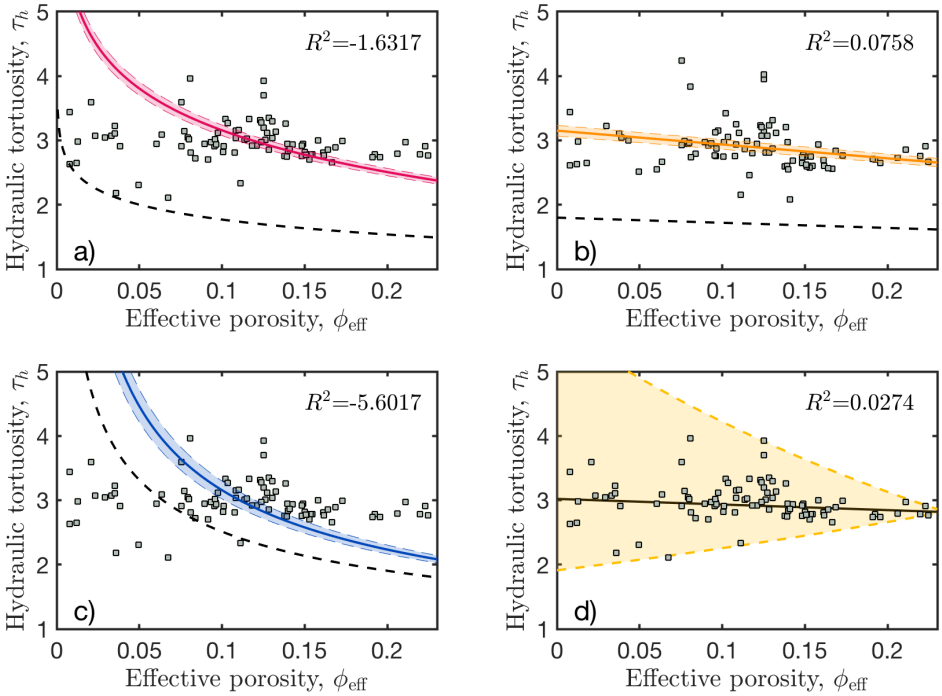

Figure 5.4: **(a)-(c)** show the proposed relations for the hydraulic tortuosity according to **(a)** Matyka et al. (2008), **(b)** Koponen et al. (1996) and **(c)** Mota et al. (2001) as black dashed lines. The colored solid lines represent the fit of the computed data to those relations within the 95% confidence bounds. Hydraulic tortuosities for all subsamples (grey squares) are computed according to the method used in each of these studies. **(d)** shows the fit obtained in the present study. The colored area in **(d)** illustrates the extending distribution of computed hydraulic tortuosities with decreasing effective porosity.

perimentally measured samples, the numerical permeabilities tend towards higher values, but show a clear trend.

As we split each sample in eight subsamples for numerical permeability computations, we need to average them to compute an effective sample permeability that can then be compared to measured values. This upscaling issue is not trivial to address and it is not clear yet which averaging method is appropriate. It is possible to put bounds on the effective permeability by using either the arithmetic or harmonic mean of subsample permeabilities. However, these bounds correspond to very specific geometrical sample structures. In the case of the arithmetic mean, the medium is assumed to consist of parallel layers oriented parallel to the flow direction whereas the harmonic mean is valid in the case of parallel layers orthogonal to the flow direction. This is most often not the case. Therefore, different averaging methods have been developed to obtain adequate upscaling procedures for heterogeneous porous media (e.g. Sahimi, 2006; Jang et al., 2011; Torquato, 2013). One of the simplest averaging schemes that has been shown to be an appropriate approximation for heterogeneous porous media is the geometric mean (e.g. Warren and Price,

1961; P. Selvadurai and A. Selvadurai, 2014; Jang et al., 2011), which reads as:

$$k_g = \left(\prod_{i=1}^{n} k_i \right)^{1/n} \tag{111}$$

where i is the number of the subsample and n the total number of subsamples (eight in this study). As several subsamples at low porosities did not exhibit a connected pore space (thus not allowing for any fluid flow), we assumed a permeability of 10^{-20} m^2 for these samples. The geometric averages of each subsample set are shown in Fig. 5.5.

To determine the predictive power of the different permeability parameterizations described in the introduction, we inserted the expressions for effective specific surface and hydraulic tortuosity into the respective equations (eq. (89) & (90)).

The Kozeny-Carman equation then reads as:

$$k = k_0 \frac{[min(\phi_{\text{eff}}) - \phi_{\text{c}}]^3}{2.9715^2 \cdot \left[-\frac{3}{3.8509 \times 10^{-4}\, m} \phi_{\text{eff}} ln(\phi_{\text{eff}}) \right]^2}, \tag{112}$$

with $k_0 = 0.5$ being the geometrical parameter for spherical particles (Kozeny, 1927) and $\phi_c = 0.01$ as the critical porosity threshold. This threshold is lower than the published value of $\phi_c = 0.03$ (Van der Marck, 1996; Rintoul, 2000; Wadsworth et al., 2016). However, one of the subsamples used in this study had a porosity of 0.01 while still exhibiting a percolating cluster. For this reason, we here employed a critical porosity of $\phi_c = 0.01$.

With our parameterization for S, the permeability parameterization of Martys et al. (1994) reads as follows:

$$k = \frac{2[1 - min(\phi_{\text{eff}}) - \phi_c]}{\left[-\frac{3}{3.8509 \times 10^{-4}\, m} \phi_{\text{eff}} ln(\phi_{\text{eff}}) \right]^2} [min(\phi_{\text{eff}}) - \phi_c]^{4.2}, \tag{113}$$

From the grain size distribution of the glass beads used in this study (see Appendix 5.6.4), we also determined the average grain diameter d and the harmonic mean diameter D, both within uncertainties equal to 1.20 mm. Inserting into the respective parameterizations of Revil and Cathles III (1999) and Garcia et al. (2009) (see eq. (92) and (93)) results in:

$$k = \frac{[1.20 \times 10^{-3}\, m]^2 min(\phi_{\text{eff}})^{5.1}}{24}, \tag{114}$$

$$k = min(\phi_{\text{eff}})^{0.11} [1.20 \times 10^{-3}\, m]^2 \tag{115}$$

The permeability parameterizations in general show similar trends but differ in the predicted permeability value. The Kozeny-Carman relation shows good agreement with the experimentally measured samples, but also shows some offset towards the numerically computed values. A similarly good fit is obtained by the permeability parameterization of Martys et al. (1994). The parameterizations by Garcia et al. (2009) and Revil and Cathles III (1999) tend to underestimate permeability, which might be related to their assumptions on the samples heterogeneity.

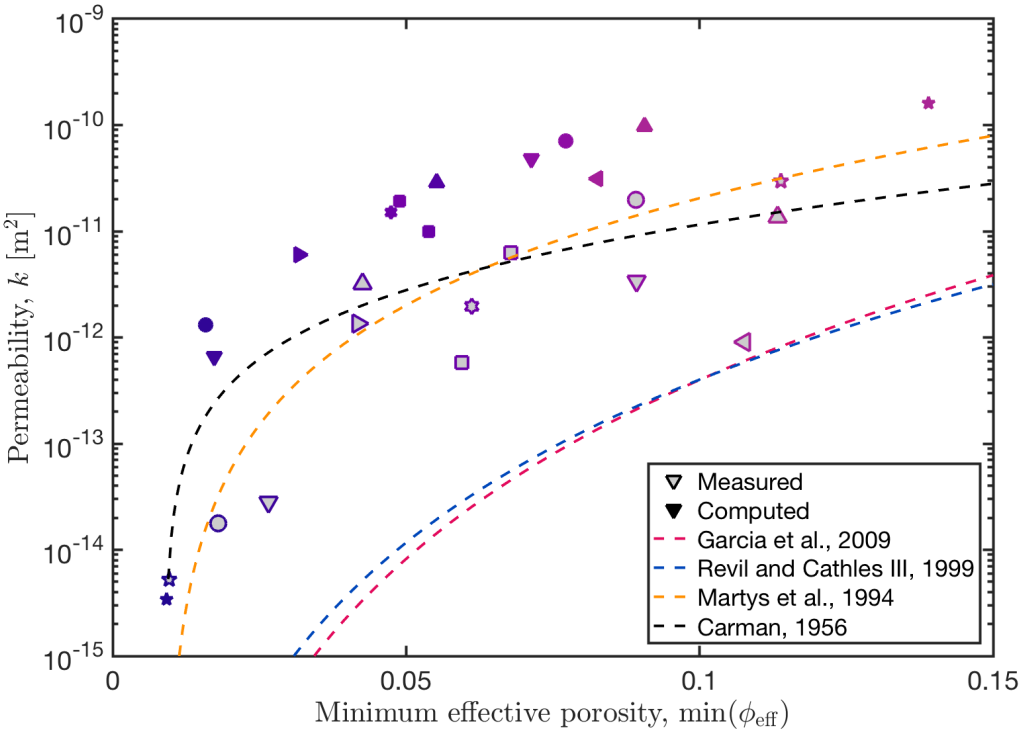

Figure 5.5: Computed and measured permeability against minimum effective porosity. Symbols of the same shape and color represent the same sample. Samples with grey face color represent measured values, whereas color only symbols stand for computed subsamples. The computed permeabilities represent the geometric mean values of all subsamples. To verify existing permeability parameterizations, we plotted the relations of Revil and Cathles III (1999), Garcia et al. (2009) and Carman (1956) and Martys et al. (1994) against the experimental and numerical permeabilities. Note that estimated errors for the experimental permeability measurements (table 5.1a) are smaller than the displayed symbols. Some subsamples with low effective porosity did not show a continuous pathway throughout the subsample, thus we assumed a very low permeability of $10^{-20}\,\mathrm{m}^2$.

5.5 Discussion and conclusion

In this paper, we determine the permeability of nearly isotropic porous media consisting of sintered glass beads using a combined experimental-numerical approach. We analyzed sample microstructures using CT data and determined flow properties

both experimentally and numerically. Using this data, we test different permeability parameterizations that have been proposed in the literature. The goal of this study was to particularly improve permeability parameterizations at low porosities (<20%).

Two particular microstructural parameters that we determined were the specific surface S and the hydraulic tortuosity τ_h. As these two parameters are frequently used in permeability parameterizations, we tested whether existing parameterizations are also valid in our case. We find that the effective specific surface is well predicted by the parameterization eq. (109) proposed by Koponen et al. (1996), not only for the chosen subsamples but also for the full samples. The fitted hydraulic radius of 0.385 mm is reasonable as the initial grain size of the glass beads is around 1 mm and the hydraulic pore radius of the glass beads is reduced during sample sintering.

Only few studies have investigated hydraulic tortuosity for three dimensional porous media (Du Plessis and Masliyah, 1991; Ahmadi et al., 2011; Backeberg et al., 2017). As the hydraulic tortuosity is challenging to determine in experiments, experimental studies have often used this parameter as a fitting variable. Our data shows that - contrary to previous suggestions - the hydraulic tortuosity does not change significantly with decreasing effective porosity (Matyka et al., 2008; Koponen et al., 1996; Mota et al., 2001), at least at the low porosities investigated in this study. This observation agrees with the study by Koponen et al. (1996), but is at odds with the studies by Matyka et al. (2008) and Mota et al. (2001). The study by Koponen et al. (1996) was based on 2D numerical simulations and found hydraulic tortuosity values close to 2 whereas our data lies around a value of 3. The difference between previous relations and our data is likely related to the different particle geometries used and that previous studies were done in 2D, while we employ 3D samples.

Measured and computed permeabilities are generally in good agreement, with computed permeabilities consistently yielding towards higher values than experimentally measured permeabilities. The experimental measured permeabilities show some scatter which might be related to heterogeneities within the sample. Interestingly, numerical permeability computations based on subsamples show much less scatter. Both the modified Kozeny-Carman relation and the parameterization by Martys et al. (1994) predict numerically computed and experimentally measured permeability values well. In the modified Kozeny-Carman relation, hydraulic tortuosity seems to have a second order influence on the permeability of porous media. The permeability parameterizations by Revil and Cathles III (1999) and Garcia et al. (2009) underestimate permeabilities, which could be related to the assumptions used in these studies. It should be noted that Garcia et al. (2009) investigated heterogeneous

sand packs and found that permeabilities for homogeneous packs are 1.6 – 1.8 times higher.

There are several reasons for the discrepancy between experimental and numerical values. First, numerical permeability predictions are based on simulations on subsamples, where free slip boundary conditions are employed. These boundary conditions do not accurately represent the flow field within the full sample and are therefore a possible source of error. This error can be estimated to about 20-50% of the computed value (Gerke et al., 2019). Second, the numerical computations compute the flow field on a discretized grid with a given resolution. In particular at low porosities, pore structures may be too small to be well resolved by the grid. As discussed by previous studies the accuracy of permeability prediction improves with increasing numerical resolution (Gerke et al., 2018; Keehm, 2003; Eichheimer et al., 2019). To investigate this effect with respect to our samples, we computed the permeability of two subsamples (Ex35Sub04 and Ex36Sub02 see supplemental material) using an increased resolution of 1024^3 grid points. The two samples with effective porosities at around 9 and 15% represent samples on both sides of the median of the present study's effective porosity range ($1.5 - 22\%$). The permeability obtained using doubled grid resolution decreases only by around $\approx 2-4\%$ compared to the outcome of models with 512^3 grid resolution (see Appendix 5.6.6). We are therefore confident that the calculations with 512^3 grid points provide sufficiently accurate results. To further increase the accuracy of the numerical computations, adaptive meshing methods could be useful.

Third and most important, it is not clear whether either the subsamples used in the numerical computations or the full samples used for experimental measurements can be considered representative volume elements at a certain porosity. The scatter that we observe in both numerical and experimental permeability measurements indicates that this may not be the case, in particular at porosities close to the critical porosity. A potential remedy for this issue would be the use of larger samples in both experiments and numerical simulations. However, using larger samples is not trivial. On the numerical side larger samples require significantly more computational resources. On the experimental side, larger samples reduce the resolution of the CT scans, which would in turn reduce the value of microstructural analysis. Additionally, a reduced CT resolution would also affect numerical permeability measurements.

We show that several permeability parameterizations (the modified Kozeny-Carman equation and the permeability parameterization by Martys et al. (1994)) are capable to predict the numerically and experimentally determined permeabilities obtained in our study. However, this could only be done by determining several microstructural parameters from CT scans and by modifying the respective equations to fit

our data. In that repsect, the parameterization by Martys et al. (1994) requires less fitting parameters, which makes it in our opinion preferable. However, our results also show a significant scatter in both numerical and experimental permeability measurements which are not predicted by either parameterization. This shows that further work is needed to obtain a more universal parameterization connecting microstructural parameters to permeability. To first order, the different permeability parameterizations can be used in numerical models to simulate fluid flow in isotropic low porosity media on the larger scale. However, it has to be kept in mind that rocks in nature are commonly more complex, as they (1) often consist of grains with different shapes and sizes, (2) contain fractures which serve as preferred pathways for fluid flow and (3) often also contain anisotropic structures.

Nevertheless, our study demonstrates that numerical permeability computations can complement laboratory measurements, in particular in cases of small sample sizes or effective porosities $< 5\%$. We provide segmented input files of several samples with different porosities in the supplementary. We hope that this will allow other researchers to use this data and our results to benchmark other numerical methods in the future.

Acknowledgements

This work has been supported by DFG (grant no. GRK 2156/1), the JSPS Japanese-German graduate externship and BMBF (grant no. 03G0865A). M.T. was supported by the Bayerisches Geoinstitut Visitors Program. Calculations were performed on clusters btrzx2, University of Bayreuth and Mogon II, Johannes Gutenberg University Mainz. We thank Kirill Gerke and an anonymous reviewer for their constructive comments that helped to improve the manuscript considerably.

5.6 Appendix

5.6.1 Minimum effective porosity

This figure shows the comparison between the effective porosity and the minimum effective porosity, which may control the fluid flow within the sample. The minimum effective porosity is used in Fig. 5.5.

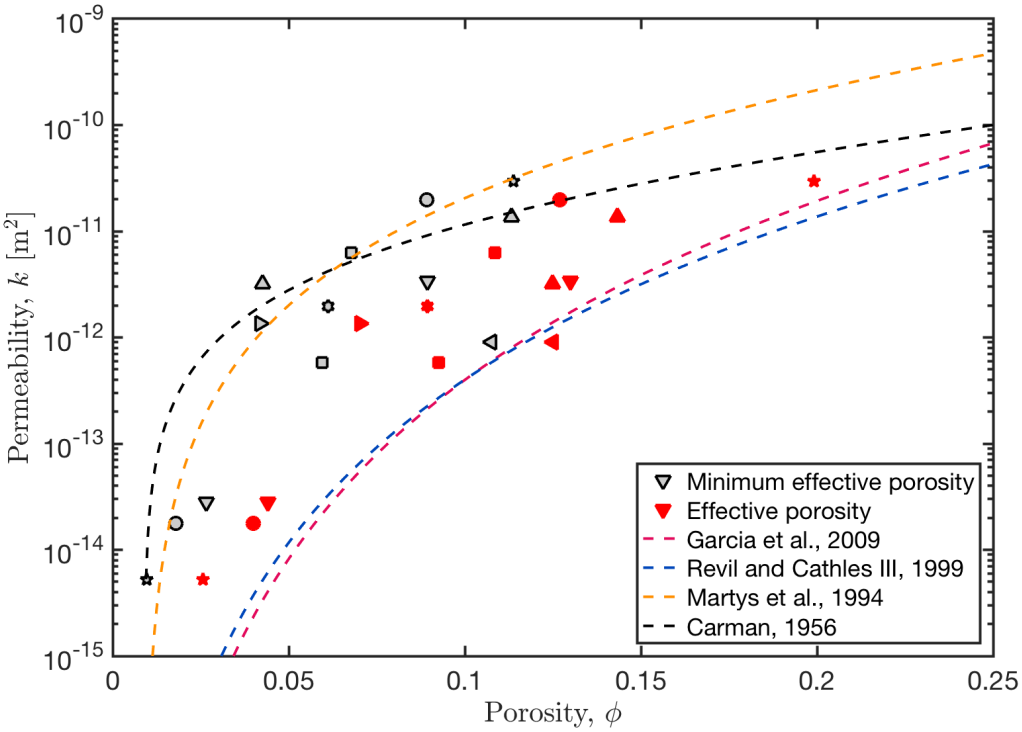

Figure 5.6: Measured permeability against porosity. Symbols with grey face color represent sample using the minimum effective porosity per sample, while red symbols display measured sample using the effective porosity. Dashed lines show several permeability parameterizations.

5.6.2 Permability of each subsample

This figure shows the computed permeability of each subsample together with the measured permeability values and the permeability parameterizations.

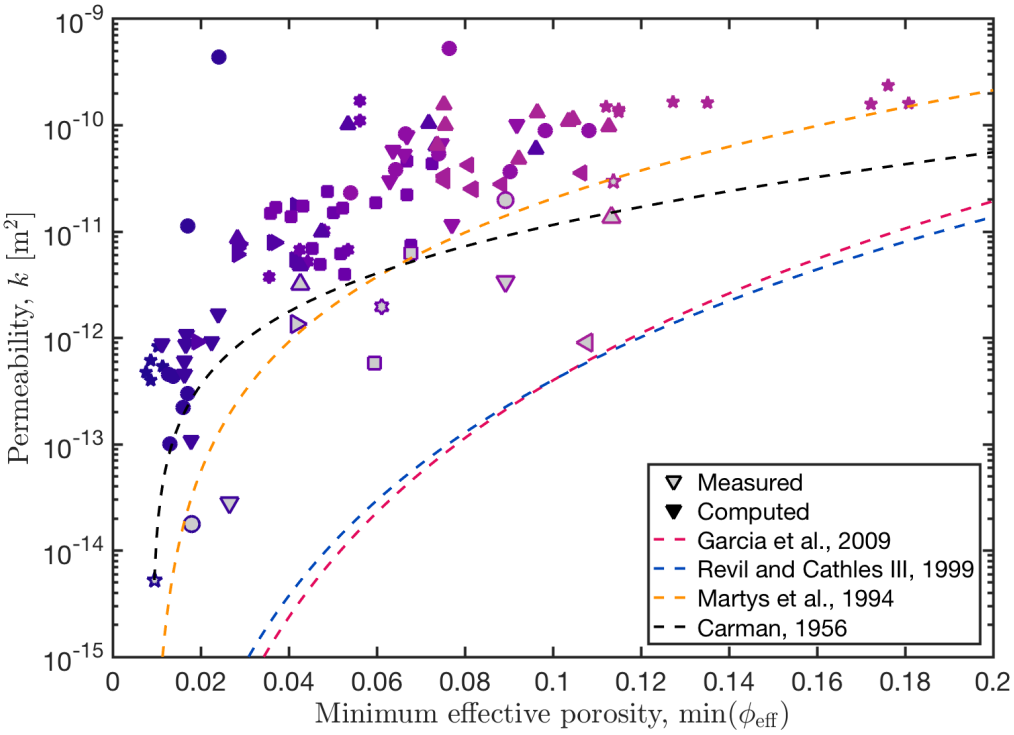

Figure 5.7: Computed and measured permeability against minimum effective porosity. Symbols of the same shape and color represent the same sample. Samples with grey face color represent measured values, whereas color only symbols stand for computed subsamples. To verify existing permeability parameterizations, we plotted the relations of Revil and Cathles III (1999), Garcia et al. (2009) and Carman (1956) and Martys et al. (1994) against the experimental and numerical permeabilities. Note that estimated errors for the experimental permeability measurements (table 5.1a) are smaller than the displayed symbols.

5.6.3 Applicability of Darcy's Law

For the numerical permeability computation using the Stokes equations we assume laminar flow conditions and incompressibility. Laminar flow conditions are represented by a linear relationship between applied pressure gradient and flow rate (Fig. 5.8). Regarding the incompressibility of the working gas during the measurements we computed permeabilities using both Darcy's law (eq. (86)) and Darcy's law for compressible gas as follows (Takeuchi et al., 2008):

$$\frac{P_2^2 - P_1^2}{2P_2 L} = \frac{\eta \nu_0}{k}, \tag{116}$$

with P_2 and P_1 being the pressures at the inlet and outlet side of the sample respectively, and ν_0 being the volume flux, which is calculated from the flow rate divided by cross-sectional area of the sample. The left-hand side of eq. (116) represents the modified pressure gradient that includes the compressibility of working gas. The difference between both computed permeabilities is less than 10 %, we therefore assume the effect of compressibility to be minor.

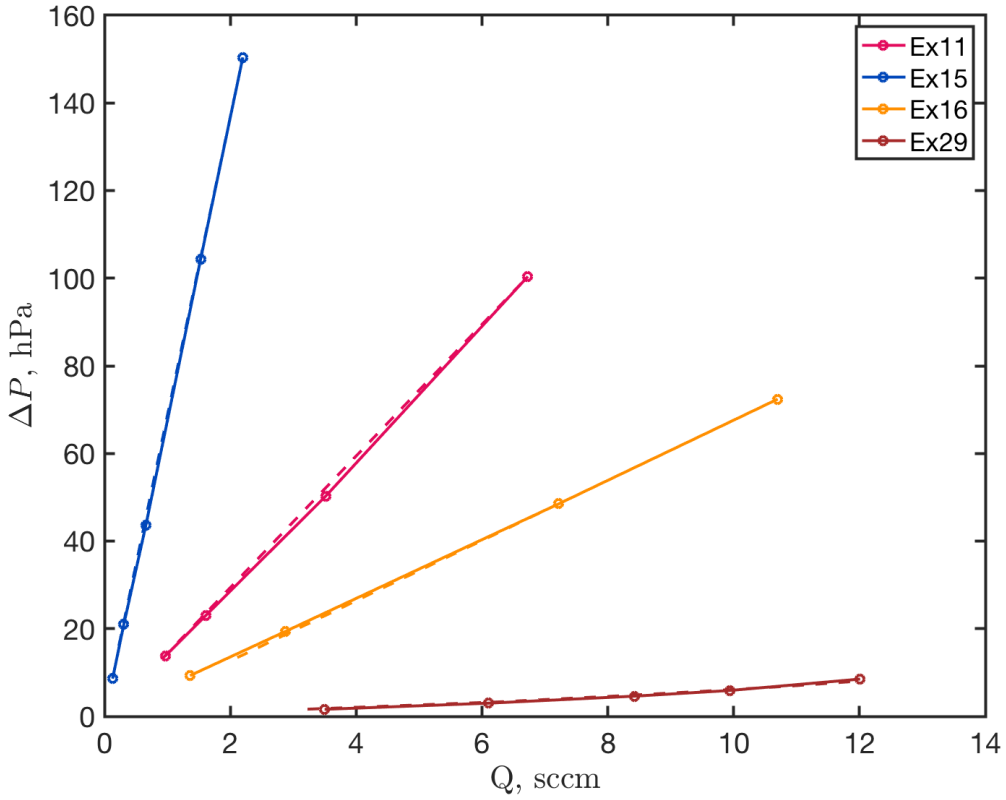

Figure 5.8: The linear relations between applied pressure difference and flow rate show that Darcy's law is valid and no turbulent flow occurs. Solid lines represent measurements while increasing the pressure difference and dashed lines while decreasing the pressure difference. The unit of *sccm* refers to a standard cubic centimeter per minute.

5.6.4 Grain size distribution of used glass beads

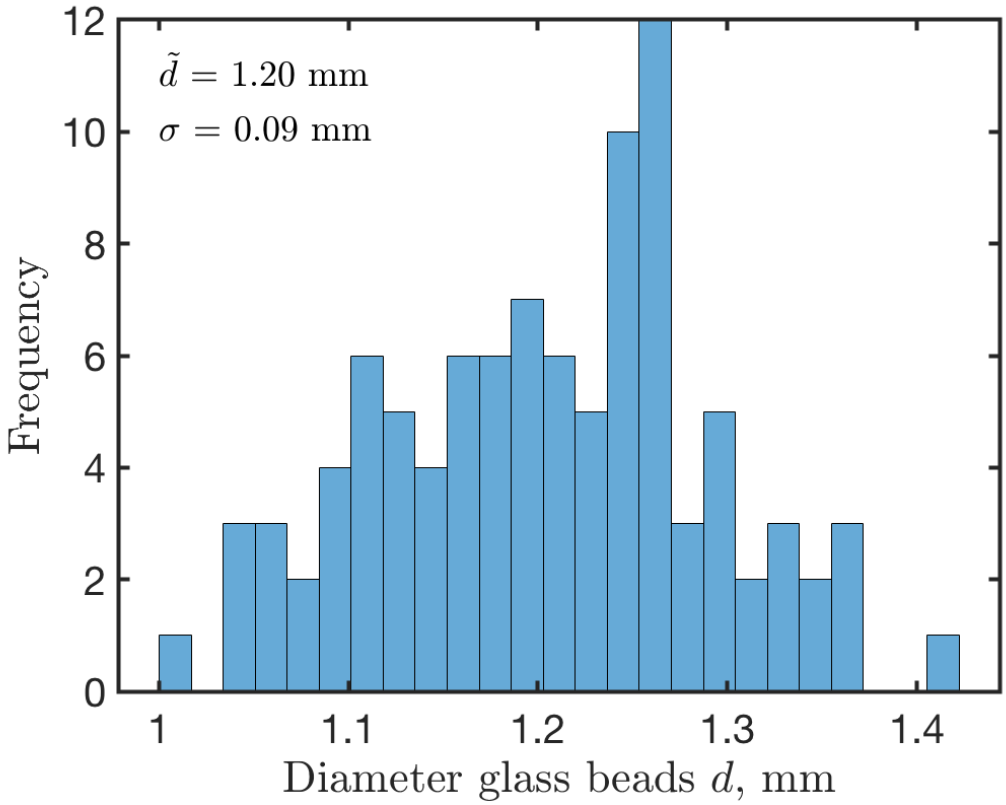

Figure 5.9: Size frequency distribution of the glass beads diameter. Beside the distribution, both arithmetic mean $\widetilde{d}$ and standard deviation σ are given.

5.6.5 Permeability upscaling schemes

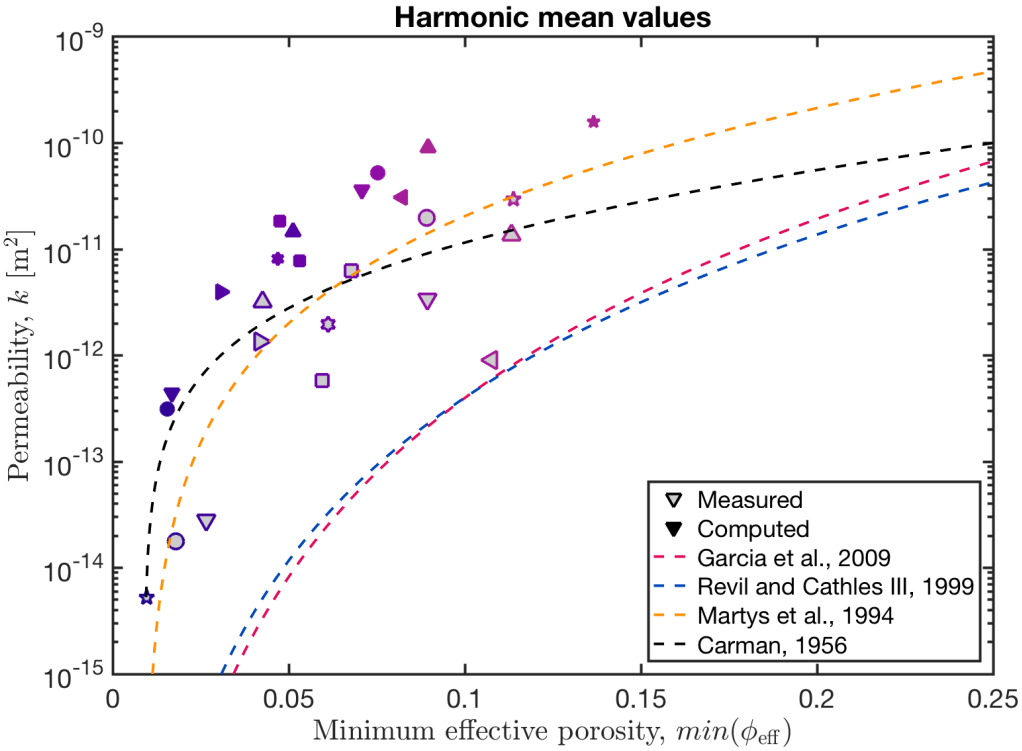

Figure 5.10: Computed and measured permeability against minimum effective porosity. Symbols of the same shape and color represent the same sample. Samples with grey face color represent measured values, whereas color only symbols stand for computed subsamples. The computed permeabilities represent the harmonic mean values of all subsamples. To verify existing permeability parameterizations, we plotted the relations of Revil and Cathles III (1999), Garcia et al. (2009) and Carman (1956) and Martys et al. (1994) against the experimental and numerical permeabilities. Note that estimated errors for the experimental permeability measurements (table 5.1a) are smaller than the displayed symbols.

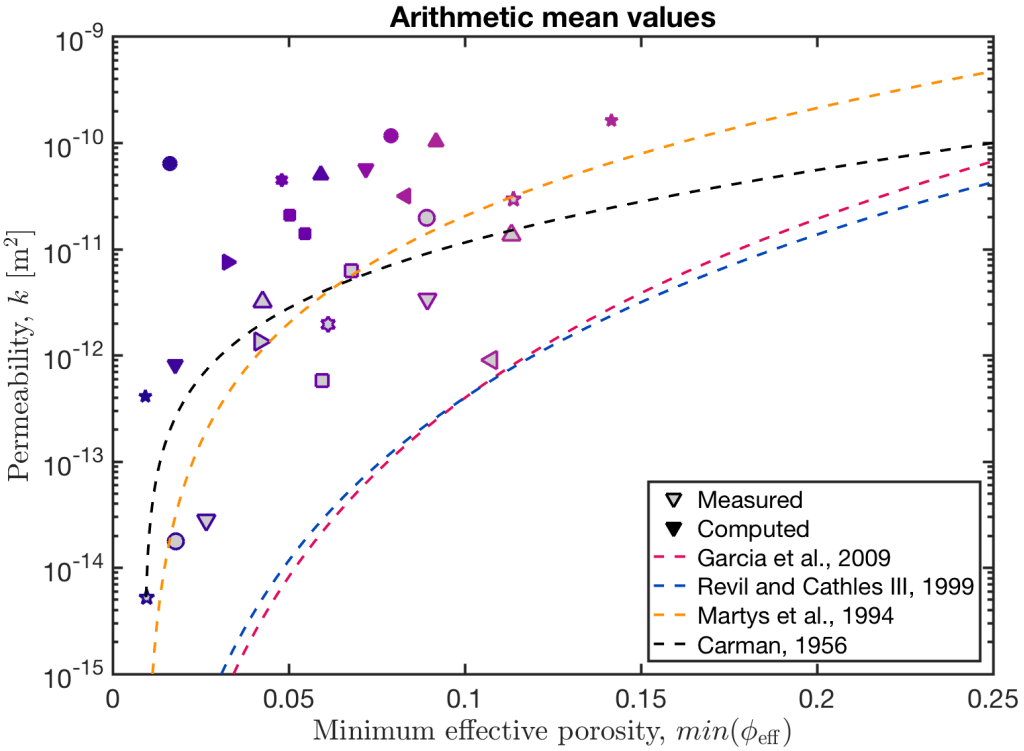

Figure 5.11: Computed and measured permeability against minimum effective porosity. Symbols of the same shape and color represent the same sample. Samples with grey face color represent measured values, whereas color only symbols stand for computed subsamples. The computed permeabilities represent the arithmetic mean values of all subsamples. To verify existing permeability parameterizations, we plotted the relations of Revil and Cathles III (1999), Garcia et al. (2009) and Carman (1956) and Martys et al. (1994) against the experimental and numerical permeabilities. Note that estimated errors for the experimental permeability measurements (table 5.1a) are smaller than the displayed symbols.

5.6.6 Resolution test

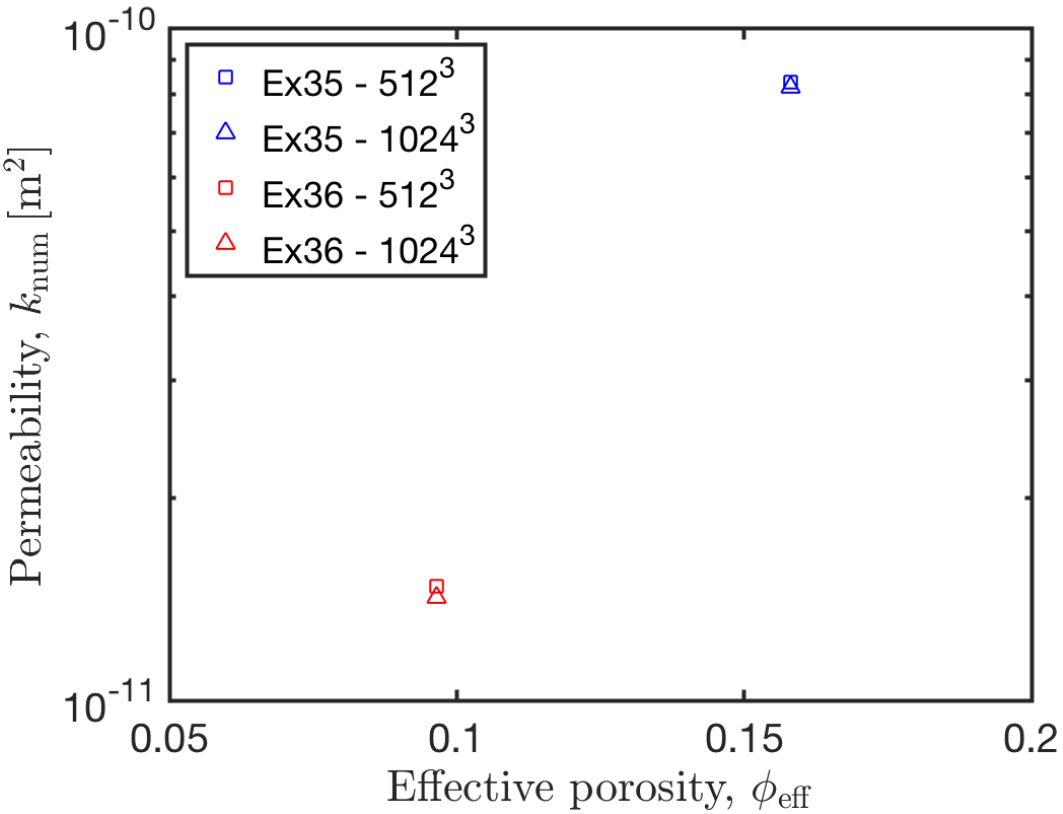

Figure 5.12: Resolution test using samples Ex35Sub04 and Ex36Sub02 (for details see also tables in the supplement). Colored squares denote standard resolution of 512^3, whereas colored triangles are simulations with resolution of 1024^3 voxels.

5.6.7 Error propagation

Darcy's Law:

$$k = -\frac{\eta Q L}{\Delta P A} \tag{117}$$

Partial derivations of Darcy's Law (assuming η to be constant during the experiment)

$$\frac{\partial k}{\partial L} = -\frac{\eta Q}{\Delta P A} \tag{118}$$

$$\frac{\partial k}{\partial \Delta P} = \frac{\eta Q L}{\Delta P^2 A} \tag{119}$$

$$\frac{\partial k}{\partial A} = \frac{\eta Q L}{\Delta P A^2} \tag{120}$$

$$\frac{\partial k}{\partial Q} = -\frac{\eta L}{\Delta P A} \tag{121}$$

Equation for error propagation:

$$\Delta k = \sqrt{\left(\frac{\partial k}{\partial L}\Delta L\right)^2 + \left(\frac{\partial k}{\partial \Delta P}\Delta P\right)^2 + \left(\frac{\partial k}{\partial A}\Delta A\right)^2 + \left(\frac{\partial k}{\partial Q}\Delta Q\right)^2} \tag{122}$$

As an example we compute the error using Darcy's Law for sample Ex16sub02. We use a precision for surface area determination A of 5 %, thickness of the sample d of 10 %, pressure measurement using the digital manometer ΔP of 0.05 % and for the flow rate Q a precision of 1 %. Using the values of sample Ex16sub02 we compute the misfits and finally the cumulative error, which is ≈5.09 %.

5.6.8 Geometric tortuosity

The geometric tortuosity is defined as (Adler, 1992; Ghanbarian et al., 2013):

$$\tau_g = \frac{L_g}{L}, \tag{123}$$

where L_g is the shortest pathway and L the length of a straight line through the sample. In order to predict geometric tortuosity models based on several geometric properties (e.g. particles size, arrangement, shape etc.) have been postulated. The model of Yu and Li (2004) predicts the geometrical tortuosity of a porous medium consisting of two-dimensional squared solid particles. The proposed equation states

as follows:

$$\tau_g = \frac{1}{2}\left[1 + \frac{1}{2}\sqrt{1-\phi} + \frac{\sqrt{\left(1-\sqrt{1-\phi}\right)^2 + (1-\phi)/4}}{1-\sqrt{1-\phi}}\right] \tag{124}$$

Another model developed by Li and Yu (2011) describes the tortuosity for a Sierpinski carpet in 2D using a pore fractal model with different particles sizes:

$$\tau_g = \left(\frac{19}{18}\right)^{ln(\phi)/ln(8/9)} \tag{125}$$

Furthermore geometric tortuosity for three-dimensional porous media with different shapes exist as proposed by Yun et al. (2006). This model also predicts geometric tortuosity for spherical particles.

In this study the geometrical tortuosity is calculated using built-in MatLab functions. In a first step the particles of the fluid phase at the top of the sample are extracted and an undirected graph is computed for all particles of the fluid phase at the bottom of the sample. The resulting arclength of each path of the undirected graph is used to compute the geometric tortuosity according to eq. (123).

The geometric tortuosity represents the shortest geometric way through a given porous medium and is not considered in the Kozeny-Carman relation. In our case it serves as a comparison to the hydraulic tortuosity and as to our knowledge there has not been any study computing the geometric tortuosity for three dimensional non-overlapping spheres.

The computed geometric tortuosity of the sintered samples is shown in Fig. 5.13b. In order to obtain reliable data we decided to plot the minimum, mean and maximum peak of each geometric tortuosity distribution as highlighted in Fig. 5.13a. The shown geometric tortuosity is relatively small compared to studies of Yu and Li (2004) and Li and Yu (2011), but shows a similar trend, especially towards small porosities.
The fitted curves as a function of porosity represent the famous $\tau = 1 - Bln(\phi)$ type proposed by Comiti and Renaud (1989). This type of equation is used to predict hydraulic tortuosities of several materials and shapes, but broadly agrees with our data and the geometric predictions by Yun et al. (2006) for three dimensional spherical particles.

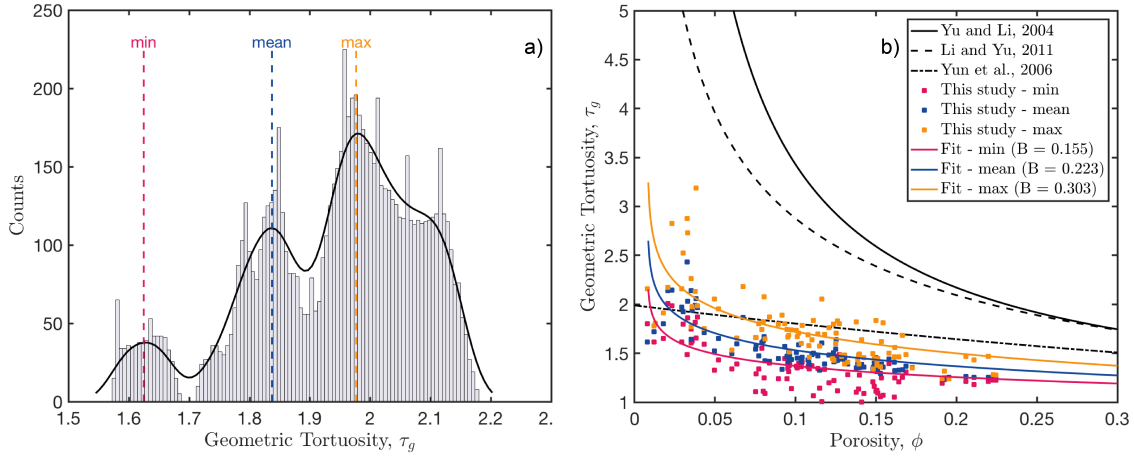

Figure 5.13: **a)** Shows the distribution of geometric tortuosity within a subsample and the peaks used for plotting. **b)** represents the prediction of geometric tortuosity against porosity using different models for two and three-dimensional porous media. Blue squares represent the mean computed geometric tortuosity, yellow the maximum values and red the minimum values of each distribution.

5.6.9 Detailed data tables for each sample

Sample name	x_{start}	y_{start}	z_{start}	Resolution	ϕ_{tot}	ϕ_{eff}	S_{tot}	S_{eff}	$\widetilde{\tau_h}$	k_{num}
Ex02Sub01	260	300	250	512x512x512	0.2058	0.2058	0.0027	0.0027	2.7974	1.3285×10^{-10}
Ex02Sub02	500	300	250	512x512x512	0.2244	0.2244	0.0026	0.0026	2.7637	2.3722×10^{-10}
Ex02Sub03	260	480	250	512x512x512	0.2196	0.2196	0.0027	0.0027	2.7806	1.5939×10^{-10}
Ex02Sub04	500	480	250	512x512x512	0.2229	0.2229	0.0027	0.0027	2.9140	1.6083×10^{-10}
Ex02Sub05	260	300	492	512x512x512	0.1925	0.1924	0.0025	0.0025	2.7807	1.4017×10^{-10}
Ex02Sub06	500	300	492	512x512x512	0.1954	0.1953	0.0024	0.0024	2.7434	1.6425×10^{-10}
Ex02Sub07	260	480	492	512x512x512	0.2108	0.2108	0.0025	0.0025	2.9747	1.6320×10^{-10}
Ex02Sub08	500	480	492	512x512x512	0.1911	0.1910	0.0024	0.0024	2.7406	1.4882×10^{-10}

x_{start}: Starting point in x-direction in the full sample

y_{start}: Starting point in y-direction in the full sample

z_{start}: Starting point in z-direction in the full sample

ϕ_{tot}: Total porosity of the subsample

ϕ_{eff}: Effective porosity of the subsample

S_{tot}: Total specific surface of the subsample $[\mu m^{-1}]$

S_{eff}: Effective specific surface of the subsample $[\mu m^{-1}]$

$\widetilde{\tau_h}$: Average hydraulic tortuosity of the subsample

k_{num}: Numerical estimate for the permeability of the subsample $[m^2]$

Table 5.2: Table presenting all computed parameters for each subsample of full sample 02.

Sample name	x_{start}	y_{start}	z_{start}	Resolution	ϕ_{tot}	ϕ_{eff}	S_{tot}	S_{eff}	$\widetilde{\tau_h}$	k_{num}
Ex11Sub01	280	190	200	512x512x512	0.041458	0.03268	0.001167	0.000886	2.7716	2.2256×10^{-13}
Ex11Sub02	470	190	200	512x512x512	0.071224	0.06746	0.001179	0.000997	2.1095	4.3785×10^{-10}
Ex11Sub03	280	450	200	512x512x512	-	-	-	-	-	-
Ex11Sub04	470	450	200	512x512x512	0.037491	0.020753	0.001150	0.000604	2.5783	2.2256×10^{-13}
Ex11Sub05	280	190	438	512x512x512	0.045670	0.035713	0.001211	0.00950	3.5928	4.3251×10^{-13}
Ex11Sub06	470	190	438	512x512x512	0.054834	0.05215	0.001183	0.001044	2.1776	1.1288×10^{-11}
Ex11Sub07	280	450	438	512x512x512	0.040818	0.023252	0.001130	0.000612	3.0747	1.0000×10^{-13}
Ex11Sub08	470	450	438	512x512x512	0.038262	0.03304	0.001107	0.00858	3.0947	3.0000×10^{-13}

x_{start}: Starting point in x-direction in the full sample
y_{start}: Starting point in y-direction in the full sample
z_{start}: Starting point in z-direction in the full sample
ϕ_{tot}: Total porosity of the subsample
ϕ_{eff}: Effective porosity of the subsample
S_{tot}: Total specific surface of the subsample $[\mu m^{-1}]$
S_{eff}: Effective specific surface of the subsample $[\mu m^{-1}]$
$\widetilde{\tau_h}$: Average hydraulic tortuosity of the subsample
k_{num}: Numerical estimate for the permeability of the subsample $[m^2]$

Table 5.3: Table presenting all computed parameters for each subsample of full sample 11. Empty cells denote subsample without interconnected pathways.

Sample name	x_{start}	y_{start}	z_{start}	Resolution	ϕ_{tot}	ϕ_{eff}	S_{tot}	S_{eff}	$\widetilde{\tau}_h$	k_{num}
Ex14Sub01	200	200	200	512x512x512	0.1542	0.1540	0.0034	0.0034	2.7813	$1.0111990 \times 10^{-10}$
Ex14Sub02	200	200	200	512x512x512	0.1571	0.1571	0.0034	0.0034	2.7612	$1.0443840 \times 10^{-10}$
Ex14Sub03	200	200	200	512x512x512	0.1448	0.1447	0.0034	0.0034	2.8081	$6.4047690 \times 10^{-11}$
Ex14Sub04	200	200	200	512x512x512	0.1486	0.1470	0.0034	0.0034	2.9281	$5.9222040 \times 10^{-11}$
Ex14Sub05	200	200	200	512x512x512	0.1029	0.1001	0.0027	0.0025	2.8168	$4.1996600 \times 10^{-12}$
Ex14Sub06	200	200	200	512x512x512	0.1194	0.1131	0.0027	0.0025	2.8374	$7.6716540 \times 10^{-12}$
Ex14Sub07	200	200	200	512x512x512	0.1065	0.1059	0.0027	0.0027	3.6978	$9.6691650 \times 10^{-12}$
Ex14Sub08	200	200	200	512x512x512	0.1191	0.1188	0.0029	0.0028	3.9223	$9.4282180 \times 10^{-12}$

x_{start}: Starting point in x-direction in the full sample
y_{start}: Starting point in y-direction in the full sample
z_{start}: Starting point in z-direction in the full sample
ϕ_{tot}: Total porosity of the subsample
ϕ_{eff}: Effective porosity of the subsample
S_{tot}: Total specific surface of the subsample $[\mu m^{-1}]$
S_{eff}: Effective specific surface of the subsample $[\mu m^{-1}]$
$\widetilde{\tau}_h$: Average hydraulic tortuosity of the subsample
k_{num}: Numerical estimate for the permeability of the subsample $[m^2]$

Table 5.4: Table presenting all computed parameters for each subsample of full sample 14.

Sample name	x_{start}	y_{start}	z_{start}	Resolution	ϕ_{tot}	ϕ_{eff}	S_{tot}	S_{eff}	$\widetilde{\tau_h}$	k_{num}
Ex15Sub01	210	200	200	512x512x512	0.023587	0.012874	0.000814	0.000392	2.9814	3.9788×10^{-13}
Ex15Sub02	390	200	200	512x512x512	0.023149	0.018063	0.000833	0.000584	3.0012	8.3110×10^{-13}
Ex15Sub03	210	450	200	512x512x512	-	-	-	-	-	-
Ex15Sub04	390	450	200	512x512x512	0.024866	0.007898	0.000797	0.000264	3.4385	5.4179×10^{-13}
Ex15Sub05	210	200	438	512x512x512	0.025917	0.011987	0.000836	0.000326	2.6455	4.7369×10^{-13}
Ex15Sub06	390	200	438	512x512x512	0.023433	0.007965	0.000850	0.000242	2.6323	6.1786×10^{-13}
Ex15Sub07	210	450	438	512x512x512	-	-	-	-	-	-
Ex15Sub08	390	450	438	512x512x512	-	-	-	-	-	-

x_{start}: Starting point in x-direction in the full sample
y_{start}: Starting point in y-direction in the full sample
z_{start}: Starting point in z-direction in the full sample
ϕ_{tot}: Total porosity of the subsample
ϕ_{eff}: Effective porosity of the subsample
S_{tot}: Total specific surface of the subsample $[\mu m^{-1}]$
S_{eff}: Effective specific surface of the subsample $[\mu m^{-1}]$
$\widetilde{\tau_h}$: Average hydraulic tortuosity of the subsample
k_{num}: Numerical estimate for the permeability of the subsample $[m^2]$

Table 5.5: Table presenting all computed parameters for each subsample of full sample 15. Empty cells denote subsamples without interconnected pathways.

Sample name	x_{start}	y_{start}	z_{start}	Resolution	ϕ_{tot}	ϕ_{eff}	S_{tot}	S_{eff}	$\widetilde{\tau_h}$	k_{num}
Ex16Sub01	250	200	200	512x512x512	0.04444	0.035153	0.001122	0.000877	3.1145	6.0323×10^{-13}
Ex16Sub02	460	200	200	512x512x512	0.047556	0.038212	0.001159	0.000875	2.9813	1.0871×10^{-13}
Ex16Sub03	250	500	200	512x512x512	0.038939	0.030048	0.001068	0.00826	3.2202	9.1519×10^{-13}
Ex16Sub04	460	500	200	512x512x512	0.048469	0.043199	0.001210	0.001048	2.9144	1.6762×10^{-12}
Ex16Sub05	250	200	338	512x512x512	0.044808	0.039079	0.001031	0.000857	3.0482	4.5359×10^{-13}
Ex16Sub06	460	200	338	512x512x512	0.045129	0.037607	0.001088	0.000867	3.1044	8.8232×10^{-13}
Ex16Sub07	250	500	338	512x512x512	0.036912	0.02939	0.001005	0.0000793	3.0625	8.6359×10^{-13}
Ex16Sub08	460	500	338	512x512x512	0.044741	0.03507	0.001138	0.00883	2.8814	1.0756×10^{-12}

x_{start}: Starting point in x-direction in the full sample
y_{start}: Starting point in y-direction in the full sample
z_{start}: Starting point in z-direction in the full sample
ϕ_{tot}: Total porosity of the subsample
ϕ_{eff}: Effective porosity of the subsample
S_{tot}: Total specific surface of the subsample $[\mu m^{-1}]$
S_{eff}: Effective specific surface of the subsample $[\mu m^{-1}]$
$\widetilde{\tau_h}$: Average hydraulic tortuosity of the subsample
k_{num}: Numerical estimate for the permeability of the subsample $[m^2]$

Table 5.6: Table presenting all computed parameters for each subsample of full sample 16.

Sample name	x_{start}	y_{start}	z_{start}	Resolution	ϕ_{tot}	ϕ_{eff}	S_{tot}	S_{eff}	$\widetilde{\tau_h}$	k_{num}
Ex17Sub01	220	190	130	512x512x384	0.1290	0.128185	0.001997	0.001972	3.3537	3.3763×10^{-11}
Ex17Sub02	460	190	130	512x512x384[a]	0.131047	0.13049	0.002044	0.002025	3.2969	2.5265×10^{-11}
Ex17Sub03	220	490	130	512x512x384[a]	0.123565	0.123132	0.001996	0.001982	3.3160	3.2781×10^{-11}
Ex17Sub04	460	490	130	512x512x384[a]	0.125292	0.12505	0.001990	0.001979	3.1973	2.4791×10^{-11}
Ex17Sub05	220	190	196	512x512x384[a]	0.133309	0.132519	0.002042	0.002025	3.1319	4.2441×10^{-11}
Ex17Sub06	460	190	196	512x512x384[a]	0.138704	0.138543	0.002081	0.002071	3.2603	3.5374×10^{-11}
Ex17Sub07	220	490	196	512x512x384[a]	0.12386	0.123625	0.002013	0.002005	3.2825	3.0172×10^{-11}
Ex17Sub08	460	490	196	512x512x384[a]	0.127575	0.127238	0.002012	0.002003	3.1150	2.7717×10^{-11}

x_{start}: Starting point in x-direction in the full sample
y_{start}: Starting point in y-direction in the full sample
z_{start}: Starting point in z-direction in the full sample
ϕ_{tot}: Total porosity of the subsample
ϕ_{eff}: Effective porosity of the subsample
S_{tot}: Total specific surface of the subsample $[\mu m^{-1}]$
S_{eff}: Effective specific surface of the subsample $[\mu m^{-1}]$
$\widetilde{\tau_h}$: Average hydraulic tortuosity of the subsample
k_{num}: Numerical estimate for the permeability of the subsample $[m^2]$

Table 5.7: Table presenting all computed parameters for each subsample of full sample 17.

It should be noted that the employed micro-CT scanner only provides a fixed amount of pixels in the vertical direction, thus for larger samples the resolution in vertical direction decreases. For this reason the resolution in z-direction of sample 17 is restricted to 384 pixels.

Sample name	x_{start}	y_{start}	z_{start}	Resolution	ϕ_{tot}	ϕ_{eff}	S_{tot}	S_{eff}	$\widetilde{\tau_h}$	k_{num}
Ex29Sub01	250	270	300	512x512x512	0.079443	0.079136	0.001746	0.001726	3.0436	6.9842×10^{-12}
Ex29Sub02	550	270	300	512x512x512	0.094175	0.091719	0.001863	0.001831	2.7007	1.500×10^{-11}
Ex29Sub03	250	560	300	512x512x512	0.097119	0.096135	0.001830	0.001806	2.9604	2.3861×10^{-12}
Ex29Sub04	550	560	300	512x512x512	0.084301	0.083867	0.001732	0.001714	2.7236	4.9509×10^{-12}
Ex29Sub05	250	270	688	512x512x512	0.0101234	0.101158	0.001734	0.001728	2.9145	6.1631×10^{-12}
Ex29Sub06	550	270	688	512x512x512	0.095257	0.095225	0.001813	0.001808	2.9061	3.9683×10^{-12}
Ex29Sub07	250	560	688	512x512x512	0.139354	0.1393344	0.002002	0.002001	2.9462	4.3762×10^{-11}
Ex29Sub08	550	560	688	512x512x512	0.108302	0.108272	0.001898	0.001894	3.1530	7.4544×10^{-12}

x_{start}: Starting point in x-direction in the full sample
y_{start}: Starting point in y-direction in the full sample
z_{start}: Starting point in z-direction in the full sample
ϕ_{tot}: Total porosity of the subsample
ϕ_{eff}: Effective porosity of the subsample
S_{tot}: Total specific surface of the subsample $[\mu m^{-1}]$
S_{eff}: Effective specific surface of the subsample $[\mu m^{-1}]$
$\widetilde{\tau_h}$: Average hydraulic tortuosity of the subsample
k_{num}: Numerical estimate for the permeability of the subsample $[m^2]$

Table 5.8: Table presenting all computed parameters for each subsample of full sample 29.

Sample name	x_{start}	y_{start}	z_{start}	Resolution	ϕ_{tot}	ϕ_{eff}	S_{tot}	S_{eff}	$\widetilde{\tau_h}$	k_{num}
Ex30Sub01	300	270	220	512x512x512	0.081708	0.081016	0.001643	0.001643	2.8136	1.7547×10^{-11}
Ex30Sub02	570	270	220	512x512x512	0.061623	0.060453	0.001480	0.001411	2.9487	7.0034×10^{-12}
Ex30Sub03	300	620	220	512x512x512	0.078211	0.077074	0.001632	0.001586	3.1405	7.8634×10^{-12}
Ex30Sub04	570	620	220	512x512x512	0.052056	0.049618	0.001420	0.001321	2.3078	9.1998×10^{-13}
Ex30Sub05	300	270	588	512x512x512	0.080040	0.079915	0.001656	0.001646	3.0186	7.8493×10^{-12}
Ex30Sub06	570	270	588	512x512x512	0.064841	0.063569	0.001474	0.001426	3.0924	6.0615×10^{-12}
Ex30Sub07	300	620	588	512x512x512	0.075901	0.075296	0.001600	0.001566	2.9057	7.6428×10^{-12}
Ex30Sub08	570	620	588	512x512x512	0.075952	0.075502	0.001545	0.001518	3.5890	5.4412×10^{-12}

x_{start}: Starting point in x-direction in the full sample
y_{start}: Starting point in y-direction in the full sample
z_{start}: Starting point in z-direction in the full sample
ϕ_{tot}: Total porosity of the subsample
ϕ_{eff}: Effective porosity of the subsample
S_{tot}: Total specific surface of the subsample $[\mu m^{-1}]$
S_{eff}: Effective specific surface of the subsample $[\mu m^{-1}]$
$\widetilde{\tau_h}$: Average hydraulic tortuosity of the subsample
k_{num}: Numerical estimate for the permeability of the subsample $[m^2]$

Table 5.9: Table presenting all computed parameters for each subsample of full sample 30.

Sample name	x_{start}	y_{start}	z_{start}	Resolution	ϕ_{tot}	ϕ_{eff}	S_{tot}	S_{eff}	$\widetilde{\tau_h}$	k_{num}
Ex31Sub01	300	200	300	512x512x512	0.083755	0.080562	0.001589	0.001494	3.9590	3.7192×10^{-12}
Ex31Sub02	570	200	300	512x512x512	0.112373	0.111034	0.001696	0.001650	2.3322	1.6933×10^{-10}
Ex31Sub03	300	580	300	512x512x512	0.094594	0.094583	0.001737	0.001734	-	-
Ex31Sub04	570	580	300	512x512x512	0.097983	0.097562	0.001777	0.001756	3.1126	6.7461×10^{-12}
Ex31Sub05	300	200	585	512x512x512	0.102019	0.101986	0.001814	0.001808	3.3335	1.0271×10^{-11}
Ex31Sub06	570	200	585	512x512x512	0.116349	0.116260	0.001781	0.001770	3.3330	1.1042×10^{-10}
Ex31Sub07	300	580	585	512x512x512	0.093658	0.093150	0.001813	0.001799	2.9759	6.7769×10^{-12}
Ex31Sub08	570	580	585	512x512x512	0.095722	0.095647	0.001842	0.001833	3.0146	5.2386×10^{-12}

x_{start}: Starting point in x-direction in the full sample
y_{start}: Starting point in y-direction in the full sample
z_{start}: Starting point in z-direction in the full sample
ϕ_{tot}: Total porosity of the subsample
ϕ_{eff}: Effective porosity of the subsample
S_{tot}: Total specific surface of the subsample $[\mu m^{-1}]$
S_{eff}: Effective specific surface of the subsample $[\mu m^{-1}]$
$\widetilde{\tau_h}$: Average hydraulic tortuosity of the subsample
k_{num}: Numerical estimate for the permeability of the subsample $[m^2]$

Table 5.10: Table presenting all computed parameters for each subsample of full sample 31. Empty cells denote a simulation which did not converge.

Sample name	x_{start}	y_{start}	z_{start}	Resolution	ϕ_{tot}	ϕ_{eff}	S_{tot}	S_{eff}	$\widetilde{\tau_h}$	k_{num}
Ex32Sub01	260	200	300	512x512x512	0.14897	0.148925	0.002311	0.002307	2.9500	5.7975×10^{-11}
Ex32Sub02	480	200	300	512x512x512	0.139209	0.139177	0.002183	0.002180	2.7449	6.6573×10^{-11}
Ex32Sub03	260	580	300	512x512x512	0.108525	0.108454	0.001954	0.001946	3.0370	2.9841×10^{-11}
Ex32Sub04	480	580	300	512x512x512	0.126154	0.126113	0.002051	0.002047	3.0112	5.3088×10^{-11}
Ex32Sub05	260	200	688	512x512x512	0.15043	0.150423	0.002209	0.002208	-	-
Ex32Sub06	480	200	688	512x512x512	0.153428	0.153424	0.002277	0.002276	2.7845	1.0090×10^{-10}
Ex32Sub07	260	580	688	512x512x512	0.121058	0.120886	0.001923	0.001912	2.9216	1.1587×10^{-11}
Ex32Sub08	480	580	688	512x512x512	0.13975	0.139708	0.002132	0.002127	2.8426	7.9489×10^{-11}

x_{start}: Starting point in x-direction in the full sample
y_{start}: Starting point in y-direction in the full sample
z_{start}: Starting point in z-direction in the full sample
ϕ_{tot}: Total porosity of the subsample
ϕ_{eff}: Effective porosity of the subsample
S_{tot}: Total specific surface of the subsample $[\mu m^{-1}]$
S_{eff}: Effective specific surface of the subsample $[\mu m^{-1}]$
$\widetilde{\tau_h}$: Average hydraulic tortuosity of the subsample
k_{num}: Numerical estimate for the permeability of the subsample $[m^2]$

Table 5.11: Table presenting all computed parameters for each subsample of full sample 32. Empty cells denote a simulation which did not converge.

Sample name	x_{start}	y_{start}	z_{start}	Resolution	ϕ_{tot}	ϕ_{eff}	S_{tot}	S_{eff}	$\widetilde{\tau}_h$	k_{num}
Ex33Sub01	250	200	300	512x512x512	0.142643	0.14262	0.002280	0.002277	2.9375	6.4878×10^{-11}
Ex33Sub02	500	200	300	512x512x512	0.15276	0.15275	0.002372	0.002370	2.7040	1.1327×10^{-10}
Ex33Sub03	250	620	300	512x512x512	0.168557	0.16850	0.002375	0.002370	2.8905	1.0842×10^{-10}
Ex33Sub04	500	620	300	512x512x512	0.148534	0.14809	0.002285	0.002274	2.7569	4.8053×10^{-11}
Ex33Sub05	250	200	688	512x512x512	0.166676	0.16642	0.002194	0.002186	2.6611	1.5603×10^{-10}
Ex33Sub06	500	200	688	512x512x512	0.161741	0.16171	0.002186	0.002184	2.7634	1.3074×10^{-10}
Ex33Sub07	250	620	688	512x512x512	0.173051	0.17265	0.002252	0.002243	2.9900	1.0015×10^{-10}
Ex33Sub08	500	620	688	512x512x512	0.164098	0.16408	0.002197	0.002194	2.8590	9.7772×10^{-11}

x_{start}: Starting point in x-direction in the full sample
y_{start}: Starting point in y-direction in the full sample
z_{start}: Starting point in z-direction in the full sample
ϕ_{tot}: Total porosity of the subsample
ϕ_{eff}: Effective porosity of the subsample
S_{tot}: Total specific surface of the subsample $[\mu m^{-1}]$
S_{eff}: Effective specific surface of the subsample $[\mu m^{-1}]$
$\widetilde{\tau}_h$: Average hydraulic tortuosity of the subsample
k_{num}: Numerical estimate for the permeability of the subsample $[m^2]$

Table 5.12: Table presenting all computed parameters for each subsample of full sample 33.

Sample name	x_{start}	y_{start}	z_{start}	Resolution	ϕ_{tot}	ϕ_{eff}	S_{tot}	S_{eff}	$\widetilde{\tau_h}$	k_{num}
Ex35Sub01	300	230	300	512x512x512	0.128539	0.12846	0.002130	0.002123	2.8561	3.6485×10^{-11}
Ex35Sub02	620	230	300	512x512x512	0.141053	0.14103	0.002016	0.002013	2.8673	5.2640×10^{-10}
Ex35Sub03	300	600	300	512x512x512	0.130561	0.13053	0.002168	0.002164	3.0336	5.4220×10^{-11}
Ex35Sub04	620	600	300	512x512x512	0.158124	0.15811	0.002252	0.002249	3.0041	8.3366×10^{-11}
Ex35Sub04	620	600	300	1024x1024x1024	0.158124	0.15811	0.002252	0.002249	3.0041	8.1811×10^{-11}
Ex35Sub05	300	230	688	512x512x512	0.125034	0.12390	0.002057	0.002027	2.9775	2.3044×10^{-11}
Ex35Sub06	620	230	688	512x512x512	0.148442	0.14842	0.002095	0.002091	2.9155	3.8459×10^{-11}
Ex35Sub07	300	600	688	512x512x512	0.151153	0.15098	0.002146	0.002139	2.7789	8.9612×10^{-11}
Ex35Sub08	620	600	688	512x512x512	0.150795	0.15066	0.002102	0.002096	2.7790	8.8771×10^{-11}

x_{start}: Starting point in x-direction in the full sample
y_{start}: Starting point in y-direction in the full sample
z_{start}: Starting point in z-direction in the full sample
ϕ_{tot}: Total porosity of the subsample
ϕ_{eff}: Effective porosity of the subsample
S_{tot}: Total specific surface of the subsample $[\mu m^{-1}]$
S_{eff}: Effective specific surface of the subsample $[\mu m^{-1}]$
$\widetilde{\tau_h}$: Average hydraulic tortuosity of the subsample
k_{num}: Numerical estimate for the permeability of the subsample $[m^2]$

Table 5.13: Table presenting all computed parameters for each subsample of full sample 35.

Sample name	x_{start}	y_{start}	z_{start}	Resolution	ϕ_{tot}	ϕ_{eff}	S_{tot}	S_{eff}	$\widetilde{\tau_h}$	k_{num}
Ex36Sub01	270	280	300	512x512x512	0.114534	0.11375	0.001944	0.001924	3.0055	1.7302×10^{-11}
Ex36Sub02	600	280	300	512x512x512	0.096502	0.09645	0.001954	0.001947	2.9384	1.4803×10^{-11}
Ex36Sub02	600	280	300	1024x1024x1024	0.096502	0.09645	0.001954	0.001947	2.9384	1.4227×10^{-11}
Ex36Sub03	270	600	300	512x512x512	0.118101	0.11803	0.001933	0.001926	2.9195	4.6326×10^{-11}
Ex36Sub04	600	600	300	512x512x512	0.107842	0.10777	0.001922	0.001914	2.8096	1.8616×10^{-11}
Ex36Sub05	270	280	588	512x512x512	0.111694	0.11026	0.001890	0.001842	3.1584	1.3812×10^{-11}
Ex36Sub06	600	280	588	512x512x512	0.089328	0.08929	0.001851	0.001845	2.9481	1.6967×10^{-11}
Ex36Sub07	270	600	588	512x512x512	0.115202	0.11509	0.001956	0.001948	3.0272	2.2184×10^{-11}
Ex36Sub08	600	600	588	512x512x512	0.103681	0.10360	0.001956	0.001949	3.2698	1.6661×10^{-11}

x_{start}: Starting point in x-direction in the full sample
y_{start}: Starting point in y-direction in the full sample
z_{start}: Starting point in z-direction in the full sample
ϕ_{tot}: Total porosity of the subsample
ϕ_{eff}: Effective porosity of the subsample
S_{tot}: Total specific surface of the subsample $[\mu m^{-1}]$
S_{eff}: Effective specific surface of the subsample $[\mu m^{-1}]$
$\widetilde{\tau_h}$: Average hydraulic tortuosity of the subsample
k_{num}: Numerical estimate for the permeability of the subsample $[m^2]$

Table 5.14: Table presenting all computed parameters for each subsample of full sample 36.

References

Adler, P. (1992). *Porous media: Geometry and Transports*. Oxford: Butterworth-Heinemann.

Ahmadi, M. M., Mohammadi, S. & Hayati, A. N. (2011). Analytical derivation of tortuosity and permeability of monosized spheres: A volume averaging approach. *Phys. Rev. E*, *83*, 026312. doi:10.1103/PhysRevE.83.026312

Andrä, H., Combaret, N., Dvorkin, J., Glatt, E., Han, J., Kabel, M., ... Zhan, X. (2013a). Digital rock physics benchmarks—Part I: Imaging and segmentation. *Computers & Geosciences*, *50*, 25–32. doi:https://doi.org/10.1016/j.cageo.2012.09.005

Andrä, H., Combaret, N., Dvorkin, J., Glatt, E., Han, J., Kabel, M., ... Zhan, X. (2013b). Digital rock physics benchmarks—Part II: Computing effective properties. *Computers & Geosciences*, *50*, 33–43. doi:https://doi.org/10.1016/j.cageo.2012.09.008

Arns, C. H. (2004). A comparison of pore size distributions derived by NMR and X-ray-CT techniques. *Physica A: Statistical Mechanics and its Applications*, *339*(1-2), 159–165. doi:10.1016/j.physa.2004.03.033

Arns, C. H., Knackstedt, M. A., Pinczewski, M. V. & Lindquist, W. (2001). Accurate estimation of transport properties from microtomographic images. *Geophysical Research Letters*, *28*(17), 3361–3364. doi:10.1029/2001GL012987

Azar, J. H., Javaherian, A., Pishvaie, M. R. & Nabi-Bidhendi, M. (2008). An approach to defining tortuosity and cementation factor in carbonate reservoir rocks. *Journal of Petroleum Science and Engineering*, *60*(2), 125–131. doi:10.1016/j.petrol.2007.05.010

Backeberg, N. R., Lacoviello, F., Rittner, M., Mitchell, T. M., Jones, A. P., Day, R., ... Striolo, A. (2017). Quantifying the anisotropy and tortuosity of permeable pathways in clay-rich mudstones using models based on X-ray tomography. *Scientific Reports*, *7*(1), 14838. doi:10.1038/s41598-017-14810-1

Balay, S., Abhyankar, S., Adams, M., Brown, J., Brune, P., Buschelman, K., ... Zhang, H. (2019). *PETSc users manual* (tech. rep. No. ANL-95/11 - Revision 3.12). Argonne National Laboratory.

Bear, J. (1988). *Dynamics of fluids in porous media*. New York: Dover Publications Inc.

Bekins, B. A. & Dreiss, S. J. (1992). A simplified analysis of parameters controlling dewatering in accretionary prisms. *Earth and Planetary Science Letters*, *109*(3), 275–287. doi:https://doi.org/10.1016/0012-821X(92)90092-A

Berg, R. R. (1975). Capillary Pressures in Stratigraphic Traps. *AAPG Bulletin*, *59*(6), 939–956. doi:10.1306/83D91EF7-16C7-11D7-8645000102C1865D

Bernabé, Y., Li, M. & Maineult, A. (2010). Permeability and pore connectivity: A new model based on network simulations. *Journal of Geophysical Research: Solid Earth*, *115*(B10). doi:10.1029/2010JB007444

Bernabe, Y., Brace, W. & Evans, B. (1982). Permeability, porosity and pore geometry of hot-pressed calcite. *Mechanics of Materials*, *1*(3), 173–183. doi:https://doi.org/10.1016/0167-6636(82)90010-2

Bird, M., Butler, S. L., Hawkes, C. & Kotzer, T. (2014). Numerical modeling of fluid and electrical currents through geometries based on synchrotron X-ray tomographic images of reservoir rocks using Avizo and COMSOL. *Computers & Geosciences*, *73*, 6–16. doi:10.1016/j.cageo.2014.08.009

Bird, R., Stewart, W. & Lightfoot, E. (2006). *Transport Phenomena*. Revised second Edition. New York, London: Wiley.

Bosl, W. J., Dvorkin, J. & Nur, A. (1998). A study of porosity and permeability using a lattice Boltzmann simulation. *Geophysical Research Letters*, *25*(9), 1475–1478. doi:10.1029/98GL00859

Bourbie, T., Coussy, O., Zinszner, B. & Junger, M. C. (1992). Acoustics of porous media. *The Journal of the Acoustical Society of America*, *91*(5), 3080–3080.

Brace, W. F. (1980). Permeability of crystalline and argillaceous rocks. *International Journal of Rock Mechanics and Mining Sciences & Geomechanics Abstracts*, *17*(5), 241–251. doi:10.1016/0148-9062(80)90807-4

Carman, P. C. (1937). Fluid flow through granular beds. *Transactions, Institution of Chemical Engineers*, *15*, 150–166.

Carman, P. C. (1956). *Flow of gases through porous media*. New York: Academic Press.

Chapuis, R. P. & Aubertin, M. (2003). On the use of the kozeny–carman equation to predict the hydraulic conductivity of soils. *Canadian Geotechnical Journal*, *40*(3), 616–628. doi:10.1139/t03-013

Clennell, M. B. (1997). Tortuosity: A guide through the maze. *Geological Society, London, Special Publications*, *122*(1), 299–344.

Collinson, A. & Neuberg, J. (2012). Gas storage, transport and pressure changes in an evolving permeable volcanic edifice. *Journal of Volcanology and Geothermal Research*, *243-244*, 1–13. doi:https://doi.org/10.1016/j.jvolgeores.2012.06.027

Comiti, J. & Renaud, M. (1989). A new model for determining mean structure parameters of fixed beds from pressure drop measurements: Application to beds packed with parallelepipedal particles. *Chemical Engineering Science*, *44*(7), 1539–1545. doi:https://doi.org/10.1016/0009-2509(89)80031-4

Darcy, H. P. G. (1856). *Les Fontaines publiques de la ville de Dijon: exposition et application des principes à suivre et des formules à employer dans les questions de distribution d'eau.* Paris: V. Dalamont.

Domenico, P. A. & Schwartz, F. W. (1998). *Physical and chemical hydrogeology.* New York: Wiley.

Du Plessis, J. P. & Masliyah, J. H. (1991). Flow through isotropic granular porous media. *Transport in Porous Media*, *6*(3), 207–221. doi:10.1007/BF00208950

Dvorkin, J., Derzhi, N., Diaz, E. & Fang, Q. (2011). Relevance of computational rock physics. *Geophysics*, *76*(5), E141–E153. doi:10.1190/geo2010-0352.1

Eichheimer, P., Thielmann, M., Popov, A., Golabek, G. J., Fujita, W., Kottwitz, M. O. & Kaus, B. J. P. (2019). Pore-scale permeability prediction for newtonian and non-newtonian fluids. *Solid Earth*, *10*(5), 1717–1731. doi:10.5194/se-10-1717-2019

Fehn, U. & Cathles, L. M. (1979). Hydrothermal convection at slow-spreading mid-ocean ridges. *Tectonophysics*, *55*(1-2), 239–260. doi:10.1016/0040-1951(79)90343-3

Garcia, X., Akanji, L. T., Blunt, M. J., Matthai, S. K. & Latham, J. P. (2009). Numerical study of the effects of particle shape and polydispersity on permeability. *Phys. Rev. E*, *80*, 021304. doi:10.1103/PhysRevE.80.021304

Gerke, K. M., Karsanina, M. V. & Katsman, R. (2019). Calculation of tensorial flow properties on pore level: Exploring the influence of boundary conditions on the permeability of three-dimensional stochastic reconstructions. *Phys. Rev. E*, *100*, 053312. doi:10.1103/PhysRevE.100.053312

Gerke, K. M., Vasilyev, R. V., Khirevich, S., Collins, D., Karsanina, M. V., Sizonenko, T. O., ... Mallants, D. (2018). Finite-difference method Stokes solver (FDMSS) for 3D pore geometries: Software development, validation and case studies. *Computers & Geosciences*, *114*, 41–58. doi:10.1016/j.cageo.2018.01.005

Ghanbarian, B., Hunt, A. G., Ewing, R. P. & Sahimi, M. (2013). Tortuosity in porous media: A critical review. *Soil science society of America journal*, *77*(5), 1461–1477.

Gleeson, T. & Ingebritsen, S. E. (2016). *Crustal permeability.* John Wiley & Sons, Ltd. doi:10.1002/9781119166573

Harlow, F. H. & Welch, J. E. (1965). Numerical Calculation of Time-Dependent Viscous Incompressible Flow of Fluid with Free Surface. *The Physics of Fluids*, *8*(12), 2182–2189. doi:10.1063/1.1761178

Hendraningrat, L., Li, S. & Torsæter, O. (2013). A coreflood investigation of nanofluid enhanced oil recovery. *Journal of Petroleum Science and Engineering*, *111*, 128–138. doi:10.1016/j.petrol.2013.07.003

Hernández-López, M. F., Gironás, J., Braud, I., Suárez, F. & Muñoz, J. F. (2014). Assessment of evaporation and water fluxes in a column of dry saline soil subject to different water table levels. *Hydrological Processes*, *28*(10), 3655–3669. doi:10.1002/hyp.9912

Hölting, B. & Coldewey, W. G. (2019). *Hydrogeology*. Berlin: Springer-Verlag GmbH. doi:10.1007/978-3-662-56375-5

Honarpour, M. M. (2018). *Relative Permeability Of Petroleum Reservoirs: Boca Raton, Florida*. CRC press.

Jang, J., Narsilio, G. A. & Santamarina, J. C. (2011). Hydraulic conductivity in spatially varying media—a pore-scale investigation. *Geophysical Journal International*, *184*(3), 1167–1179. doi:10.1111/j.1365-246X.2010.04893.x

Kaus, B. J. P., Popov, A. A., Baumann, T. S., Püsök, A. E., Bauville, A., Fernandez, N. & Collignon, M. (2016). Forward and Inverse Modelling of Lithospheric Deformation on Geological Timescales. *NIC Series*, *48*, 299–307.

Keehm, Y. (2003). *Computational rock physics: Transport properties in porous media and applications* (Doctoral dissertation, Stanford University).

Keller, T. & Katz, R. F. (2016). The Role of Volatiles in Reactive Melt Transport in the Asthenosphere. *Journal of Petrology*, *57*(6), 1073–1108. doi:10.1093/petrology/egw030

Keller, T. & Suckale, J. (2019). A continuum model of multi-phase reactive transport in igneous systems. *Geophysical Journal International*, *219*(1), 185–222. doi:10.1093/gji/ggz287

Klug, C. & Cashman, K. V. (1996). Permeability development in vesiculating magmas: Implications for fragmentation. *Bulletin of Volcanology*, *58*(2), 87–100. doi:10.1007/s004450050128

Koponen, A., Kataja, M. & Timonen, J. (1997). Permeability and effective porosity of porous media. *Phys. Rev. E*, *56*, 3319–3325. doi:10.1103/PhysRevE.56.3319

Koponen, A., Kataja, M. & Timonen, J. v. (1996). Tortuous flow in porous media. *Physical Review E*, *54*(1), 406–410. doi:10.1103/PhysRevE.54.406

Kozeny, J. (1927). Über kapillare Leitung des Wassers im Boden. *Royal Academy of Science, Vienna, Proc. Class I*, *136*, 271–306.

Kuczynski, G. C. (1949). Study of the sintering of glass. *Journal of Applied Physics*, *20*(12), 1160–1163.

Lamur, A., Kendrick, J. E., Eggertsson, G. H., Wall, R. J., Ashworth, J. D. & Lavallée, Y. (2017). The permeability of fractured rocks in pressurised volcanic and geothermal systems. *Scientific Reports*, *7*(1), 6173. doi:10.1038/s41598-017-05460-4

Li, J.-H. & Yu, B.-M. (2011). Tortuosity of flow paths through a sierpinski carpet. *Chinese Physics Letters*, *28*(3), 034701.

Manickam, S. S., Gelb, J. & McCutcheon, J. R. (2014). Pore structure characterization of asymmetric membranes: Non-destructive characterization of porosity and tortuosity. *Journal of Membrane Science*, *454*, 549–554. doi:10.1016/j.memsci.2013.11.044

Manwart, C., Aaltosalmi, U., Koponen, A., Hilfer, R. & Timonen, J. (2002). Lattice-Boltzmann and finite-difference simulations for the permeability for three-dimensional porous media. *Physical Review E*, *66*(1), 016702. doi:10.1103/PhysRevE.66.016702

Martys, N. S., Torquato, S. & Bentz, D. P. (1994). Universal scaling of fluid permeability for sphere packings. *Phys. Rev. E*, *50*, 403–408. doi:10.1103/PhysRevE.50.403

Matyka, M., Khalili, A. & Koza, Z. (2008). Tortuosity-porosity relation in porous media flow. *Physical Review E*, *78*(2), 026306. doi:10.1103/PhysRevE.78.026306

Miller, K. J., Zhu, W.-l., Montési, L. G. & Gaetani, G. A. (2014). Experimental quantification of permeability of partially molten mantle rock. *Earth and Planetary Science Letters*, *388*, 273–282. doi:https://doi.org/10.1016/j.epsl.2013.12.003

Morais, A. F., Seybold, H., Herrmann, H. J. & Andrade, J. S. (2009). Non-newtonian fluid flow through three-dimensional disordered porous media. *Phys. Rev. Lett. 103*, 194502. doi:10.1103/PhysRevLett.103.194502

Mostaghimi, P., Blunt, M. J. & Bijeljic, B. (2013). Computations of Absolute Permeability on Micro-CT Images. *Mathematical Geosciences*, *45*(1), 103–125. doi:10.1007/s11004-012-9431-4

Mota, M., Teixeira, J. A., Bowen, W. R. & Yelshin, A. (2001). Binary spherical particle mixed beds: porosity and permeability relationship measurement. *17*(1-4), 101–106.

Mueller, S., Melnik, O., Spieler, O., Scheu, B. & Dingwell, D. B. (2005). Permeability and degassing of dome lavas undergoing rapid decompression: An experimental determination. *Bulletin of Volcanology*, *67*(6), 526–538. doi:10.1007/s00445-004-0392-4

Napolitano, A. & Hawkins, E. G. (1964). Viscosity of a standard soda-lime-silica glass. *J. Res. Nat. Bur. Stand. A. A*, *68*, 439–448.

Nemati, R., Shahrouzi, J. R. & Alizadeh, R. (2020). A stochastic approach for predicting tortuosity in porous media via pore network modeling. *Computers and Geotechnics*, *120*, 103406. doi:10.1016/j.compgeo.2019.103406

Norton, D. & Taylor Jr, H. P. (1979). Quantitative Simulation of the Hydrothermal Systems of Crystallizing Magmas on the Basis of Transport Theory and Oxygen Isotope Data: An analysis of the Skaergaard intrusion. *Journal of Petrology*, *20*(3), 421–486. doi:10.1093/petrology/20.3.421

Okumura, S., Nakamura, M., Takeuchi, S., Tsuchiyama, A., Nakano, T. & Uesugi, K. (2009). Magma deformation may induce non-explosive volcanism via degassing through bubble networks. *Earth and Planetary Science Letters*, *281*(3), 267–274. doi:https://doi.org/10.1016/j.epsl.2009.02.036

Okumura, S. & Sasaki, O. (2014). Permeability reduction of fractured rhyolite in volcanic conduits and its control on eruption cyclicity. *Geology*, *42*(10), 843–846. doi:10.1130/G35855.1

Osorno, M., Uribe, D., Ruiz, O. E. & Steeb, H. (2015). Finite difference calculations of permeability in large domains in a wide porosity range. *Archive of Applied Mechanics*, *85*(8), 1043–1054. doi:10.1007/s00419-015-1025-4

Otsu, N. (1979). A threshold selection method from gray-level histograms. *IEEE transactions on systems, man, and cybernetics*, *9*(1), 62–66.

Pape, H., Clauser, C. & Iffland, J. (2005). Permeability prediction for reservoir sandstones and basement rocks based on fractal pore space geometry. In *Seg technical program expanded abstracts 1998* (pp. 1032–1035). Society of Exploration Geophysicists. doi:10.1190/1.1820060

Pech, D. (1984). *Etude de la perméabilité de lits compressibles constitués de copeaux de bois partiellement destructurés* (Doctoral dissertation, INP Grenoble).

Ramandi, H. L., Mostaghimi, P. & Armstrong, R. T. (2017). Digital rock analysis for accurate prediction of fractured media permeability. *Journal of Hydrology*, *554*, 817–826. doi:https://doi.org/10.1016/j.jhydrol.2016.08.029

Ren, X., Zhao, Y., Deng, Q., Li, D. & Wang, D. (2016). A relation of hydraulic conductivity – Void ratio for soils based on Kozeny-Carman equation. *Engineering Geology*, *213*. doi:10.1016/j.enggeo.2016.08.017

Revil, A. & Cathles III, L. M. (1999). Permeability of shaly sands. *Water Resources Research*, *35*(3), 651–662. doi:10.1029/98WR02700

Rintoul, M. D. (2000). Precise determination of the void percolation threshold for two distributions of overlapping spheres. *Phys. Rev. E*, *62*, 68–72. doi:10.1103/PhysRevE.62.68

Sahimi, M. (2006). *Heterogeneous materials i: Linear transport and optical properties*. Interdisciplinary Applied Mathematics. Springer New York.

Saxena, N., Mavko, G., Hofmann, R. & Srisutthiyakorn, N. (2017). Estimating permeability from thin sections without reconstruction: Digital rock study of 3D properties from 2D images. *Computers & Geosciences*, *102*, 79–99. doi:10.1016/j.cageo.2017.02.014

Selvadurai, P. & Selvadurai, A. (2014). On the effective permeability of a heterogeneous porous medium: The role of the geometric mean. *Philosophical Magazine*, *94*(20), 2318–2338. doi:10.1080/14786435.2014.913111

Shabro, V., Kelly, S., Torres-Verdín, C., Sepehrnoori, K. & Revil, A. (2014). Pore-scale modeling of electrical resistivity and permeability in FIB-SEM images of organic mudrock. *Geophysics*, *79*(5), D289–D299. doi:10.1190/geo2014-0141.1

Suleimanov, B. A., Ismailov, F. S. & Veliyev, E. F. (2011). Nanofluid for enhanced oil recovery. *Journal of Petroleum Science and Engineering*, *78*(2), 431–437. doi:10.1016/j.petrol.2011.06.014

Taheri, S., Ghomeshi, S. & Kantzas, A. (2017). Permeability calculations in unconsolidated homogeneous sands. *Powder Technology*, *321*, 380–389. doi:10.1016/j.powtec.2017.08.014

Takeuchi, S., Nakashima, S. & Tomiya, A. (2008). Permeability measurements of natural and experimental volcanic materials with a simple permeameter: Toward an understanding of magmatic degassing processes. *Journal of Volcanology and Geothermal Research*, *177*(2), 329–339. doi:10.1016/j.jvolgeores.2008.05.010

Thorat, I. V., Stephenson, D. E., Zacharias, N. A., Zaghib, K., Harb, J. N. & Wheeler, D. R. (2009). Quantifying tortuosity in porous li-ion battery materials. *Journal of Power Sources*, *188*(2), 592–600. doi:10.1016/j.jpowsour.2008.12.032

Torquato, S. (2013). *Random heterogeneous materials: Microstructure and macroscopic properties*. Interdisciplinary Applied Mathematics. Springer New York.

Van der Marck, S. C. (1996). Network Approach to Void Percolation in a Pack of Unequal Spheres. *Phys. Rev. Lett. 77*, 1785–1788. doi:10.1103/PhysRevLett.77.1785

Wadsworth, F. B., Vasseur, J., Scheu, B., Kendrick, J. E., Lavallée, Y. & Dingwell, D. B. (2016). Universal scaling of fluid permeability during volcanic welding and sediment diagenesis. *Geology*, *44*(3), 219–222. doi:10.1130/G37559.1

Wadsworth, F. B., Vasseur, J., von Aulock, F. W., Hess, K.-U., Scheu, B., Lavallée, Y. & Dingwell, D. B. (2014). Nonisothermal viscous sintering of volcanic ash. *Journal of Geophysical Research: Solid Earth*, *119*(12), 8792–8804. doi:10.1002/2014JB011453

Wang, D., Han, D., Li, W., Zheng, Z. & Song, Y. (2017). Magnetic-resonance imaging and simplified kozeny-carman-model analysis of glass-bead packs as a frame

of reference to study permeability of reservoir rocks. *Hydrogeology Journal*, *25*(5), 1465–1476. doi:10.1007/s10040-017-1555-7

Warren, J. E. & Price, H. S. (1961). Flow in heterogeneous porous media. *Society of Petroleum Engineers Journal*, *1*(03), 153–169. doi:10.2118/1579-G

Waxman, M. H. & Smits, L. J. M. (1968). Electrical conductivities in oil-bearing shaly sands. *Society of Petroleum Engineers Journal*, *8*(02), 107–122. doi:10.2118/1863-A

Wu, M., Xiao, F., Johnson-Paben, R. M., Retterer, S. T., Yin, X. & Neeves, K. B. (2012). Single- and two-phase flow in microfluidic porous media analogs based on voronoi tessellation. *Lab Chip*, *12*, 253–261. doi:10.1039/C1LC20838A

Wyllie, M. R. J. & Gregory, A. R. (1955). Fluid flow through unconsolidated porous aggregates. *Industrial & Engineering Chemistry*, *47*(7), 1379–1388. doi:10.1021/ie50547a037

Yu, B.-M. & Li, J.-H. (2004). A geometry model for tortuosity of flow path in porous media. *Chinese Physics Letters*, *21*(8), 1569.

Yun, M., Yu, B., Xu, P. & Wu, J. (2006). Geometrical Models for Tortuosity of Streamlines in Three-Dimensional Porous Media. *The Canadian Journal of Chemical Engineering*, *84*(3), 301–309.

Zhang, H., Nikolov, A. & Wasan, D. (2014). Enhanced Oil Recovery (EOR) Using Nanoparticle Dispersions: Underlying Mechanism and Imbibition Experiments. *Energy & Fuels*, *28*(5), 3002–3009. doi:10.1021/ef500272r

Chapter 6 | Modelling of volatiles in Earth's mantle

Draft of manuscript in preparation: Eichheimer, P., Thielmann, M. & Golabek, G. J.: Modelling of volatiles in Earth's mantle

6.1 Abstract

The transport and storage of water in the mantle significantly affects various material properties of mantle rocks and thus water plays a key role in a variety of geodynamical processes like tectonics and magmatism. Geological and seismological observations suggest different inflow mechanisms of water via the subducting slab, like slab bending, thermal cracking and serpentinization. Recent studies showed the influence of thermal age, dipping angle and plate velocity of the downgoing lithosphere on the location and amount of water, which potentially can be transported into the deep mantle. Most of the studies did not take the effect of normal faults on storage and transport of water into account. To which extent both parameters influence the inflow and outflow of water into the mantle still remains unclear. Therefore, we use high resolution 2D finite element simulations, which allow us to resolve subducted sediments and crustal layers. For this purpose the finite element code MVEP2, is tested against benchmark results. In a first step we reproduced the analytical corner flow model used in the benchmark of van Keken et al. (2008). In a next step a water migration scheme is implemented and tested. Further steps consist of successively increasing model complexity, such as the incorporation of temperature field and normal faults.

6.2 Introduction

Earth is the only planet in our solar system that is habitable due to the presence of liquid water on its surface, which has been suggested to be essential for life (Popkin et al., 2010). Volatiles such as H_2O and CO_2 have a strong impact on existing plate tectonics and volcanism (Peacock, 1990; Iwamori, 1998; Hilton et al., 2002; Wallace, 2005). On Earth subduction zones are suggested to play an important role for the input of volatiles like water into the mantle (Pawley and Holloway, 1993; Iwamori, 2007; Cagnioncle et al., 2007; Korenaga, 2017). At subduction zones, several processes like plate bending, sediment/slab melting, thermal cracking and serpentinization have been suggested to have a significant effect on the input and output of water in Earth's mantle (Iwamori, 1998; Stern, 2002; Korenaga, 2007; Faccenda et al., 2008). Quantifying the transport and amount of water within Earth's mantle is a key to understand several of the distinct cycling processes. Subduction of wet oceanic crust delivers a significant amount of water into the mantle, which is assumed to cause the seismic velocity anomaly in the shallow mantle (Faccenda et al., 2008). Bending of the subducting oceanic lithosphere triggers the develop-

ment of faults up to 30 km depth allowing water to percolate downwards and enter the subducting slab (Rüpke et al., 2004; Iwamori, 2007; van Keken et al., 2008; Faccenda et al., 2009). In addition to plate bending, thermal cracking continuously develops faults through constant cooling of the oceanic crust and therefore introduces additional water into the mantle (Korenaga, 2007, 2017). Moreover, through the plate's residence at the seafloor continously sediments are added onto it, storing both chemically bound and pore water (Rüpke et al., 2004).

The output of volatiles from the slab and mantle is also governed by several processes. Following Rüpke et al. (2004) water is released into the mantle at different depths. At shallow depth (< 20 km) sediments loose their water through fluid expulsion (Hensen et al., 2004). Between $20 - 100$ km sediments and the altered oceanic crust release additional water, which could lead to cold upwellings in the 'subduction channel' (Gerya et al., 2002). Additionally deep fluids are released (> 100 km) from the hydrated lithosphere through deserpentinization, triggering arc volcanism (Rüpke et al., 2004). The released water has a significant effect on both rheology of the mantle wedge and slab (Bell and Rossman, 1992; Schmidt and Poli, 1998; Hirth and Kohlstedt, 2013; Hacker, 2008) as well as on the melting processes within the mantle wedge (von Huene and Scholl, 1991; Grove et al., 2006).

Despite the large number of studies on deep volatile cycling, it still remains unclear how much water is actually transported into the mantle and released through dehydration. In recent years several authors focused on different mechanisms (e.g. chemical, mechanical) affecting the deep volatile cycle and therefore a wide range of estimations on the amount of water, which potentially could be transported into the deeper mantle via subduction zones exist (von Huene and Scholl, 1991; Wallmann, 2001; Rüpke et al., 2004; Iwamori, 2007; Johnson and Pruis, 2003; van Keken et al., 2011; Magni et al., 2014; Korenaga et al., 2017; Abers et al., 2017; Cai et al., 2018). Figure 6.1 summarizes the influxes of water proposed by various studies.

The present study has the aim of investigating fluid flow and dehydration within a subducting slab to predict the amount of water, which can potentially be transported into the deep mantle. Several studies assumed a continous distribution of water within the subducting slab (Gerya and Meilick, 2011; Angiboust et al., 2012), whereas other recent publications showed that in particular fault zones provide discrete zones of concentrated amounts of water and therefore an increased permeability (Carson and Screaton, 1998; Moore, 1989; Faccenda et al., 2008, 2009; Zhou et al., 2015). For this reason we plan to employ several discrete zones of high permeability and water concentration within the subducting slab. The distance between those zones and the number of normal faults will be changed systematically to simulate

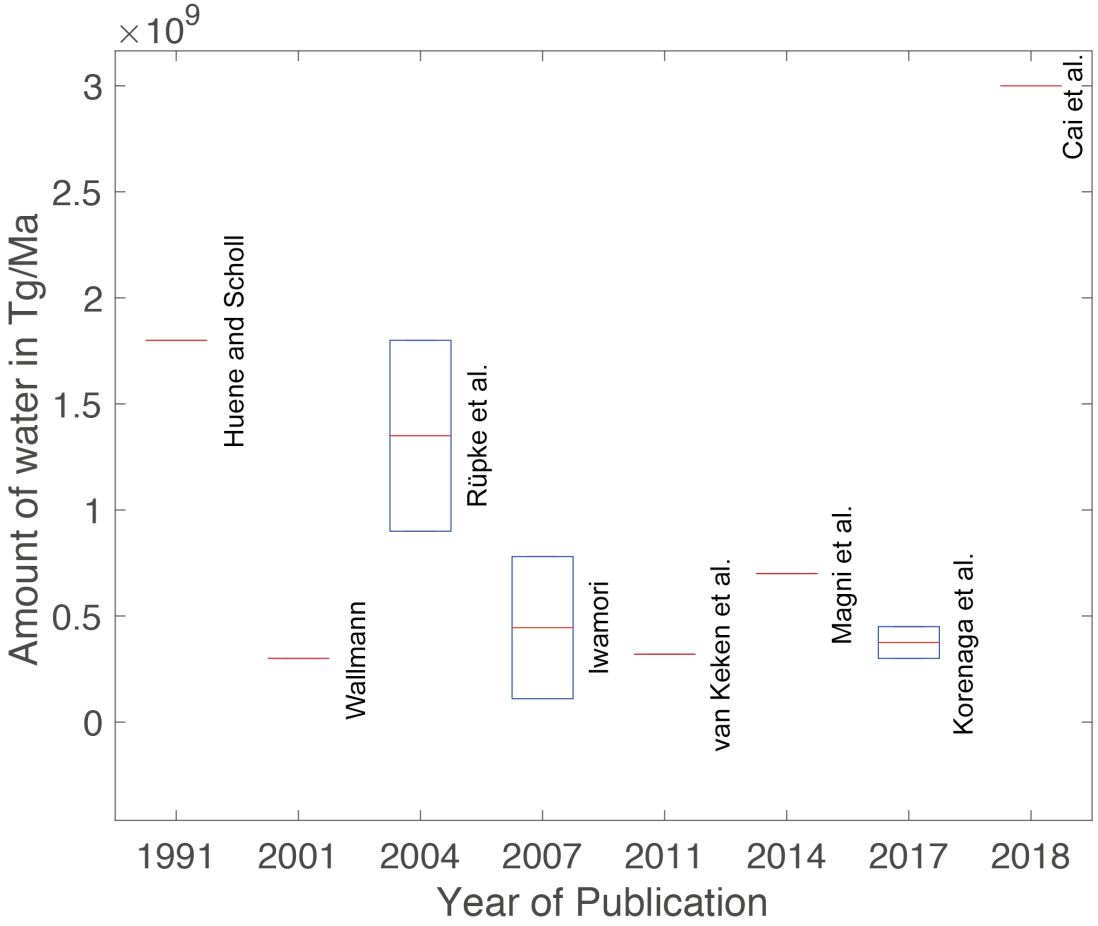

Figure 6.1: Estimated values of water influx into the mantle suggested by various authors. As explained above predictions differ since authors focused on different influx mechanisms and therefore used various assumptions. Red lines indicate the mean estimate, whereas blue boxes represent the minimum and maximum estimated values from each study.

the effect on the fluid flow within the slab and its implications on the mantle wedge.

6.3 Methods

6.3.1 Governing equations

Conservation of mass and momentum for slow creeping incompressible rocks are given as:

$$\frac{\partial v_i}{\partial x_i} = 0, \tag{126}$$

$$\frac{\partial P}{\partial x_i} - \frac{\partial \tau_{ij}}{\partial x_j} = \rho g_i, \tag{127}$$

where v is the velocity, x the spatial coordinate, P the pressure, τ the deviatoric stress tensor, ρ the density, g the gravitational acceleration. The density depends on temperature:

$$\rho(T) = \rho_0[1 - \alpha(T - T_0)], \tag{128}$$

with ρ_0 and T_0 being the reference density and temperature. Furthermore α is the thermal expansion coefficient. Due to the chosen setup, the rheology of the rocks is assumed to be viscous only. In the present study we employ dislocation and diffusion creep laws, where effective viscosities are given by:

$$\eta_{\text{eff}}^{\text{disl}} = A^{-1/n}\dot{\varepsilon}_{II}^{-1/n} \exp\left(\frac{E^{\text{disl}}}{nRT}\right), \tag{129}$$

$$\eta_{\text{eff}}^{\text{diff}} = A^{-1}d^{p} \exp\left(\frac{E^{\text{diff}}}{nRT}\right), \tag{130}$$

with A, n, E, T, R being rheological prefactor, power law exponent, activation energy for the respective creep law, temperature and the universal gas constant. $\dot{\varepsilon}_{II}$ is the second invariant of the strain rate and d is the grain size and p the grain size exponent. The effective creep viscosity is computed via:

$$\eta_{\text{eff}} = min\left[\left(\eta_{\text{eff}}^{\text{disl}}, \eta_{\text{eff}}^{\text{diff}}\right)\right]. \tag{131}$$

Conservation of energy is given by:

$$\rho C_p\left(\frac{\partial T}{\partial t} + v_i\frac{\partial T}{\partial x_i}\right) = \frac{\partial}{\partial x_i}\left(\kappa\frac{\partial T}{\partial x_i}\right) + H, \tag{132}$$

with C_p being the heat capacity, t the time, κ the thermal conductivity and H the radiogenic heat source term.

6.3.2 Numerical method & model setup

We consider a 2D model domain of 2500 km x 2000 km with a subducting slab placed at the left corner of the setup and an underlying mantle. The slab is subdivided into an upper and lower oceanic plate. In later stages it is planned to add several layers of sediments on top of the slab introducting another source of water to the model. The model domain is discretized using triangular elements with quadratic shape functions for velocity and temperature and discontinuous linear shape functions for pressure (Cuvelier et al., 1986). To reduce computational costs, mesh refinement is used. Thus, the triangular mesh has a coarser resolution in the ambient mantle and slab, whereas it is finer in the mantle wedge. For coarser parts of the mesh we have

an average element area of 0.1452 (non-dimensional) and for finer parts an average element area of 0.0059 (non-dimensional). According to the mesh refinement also the marker density, tracking material properties, is denser for the mantle wedge, whereas it is less dense in the slab and ambient mantle.

For the simulations the finite element code MVEP2 (Kaus, 2010; Thielmann et al., 2014) is used. MVEP2 uses an efficient matrix assembly method (Dabrowski et al., 2008) and was modified to simulate large-scale geological models. Material properties are tracked on markers, which are used to transfer the properties from the old deformed mesh to the current undeformed one (Thielmann and Kaus, 2012; Thielmann et al., 2014). Furthermore as with time the mesh deforms we perform remeshing after several time steps. The code solves eqs. (126)-(132), including the Stokes conservative equations for incompressible materials (eqs. (126) and (127)). To avoid numerical instabilities lower and upper viscosity cutoffs are set to 10^{18} and 10^{28} Pa s

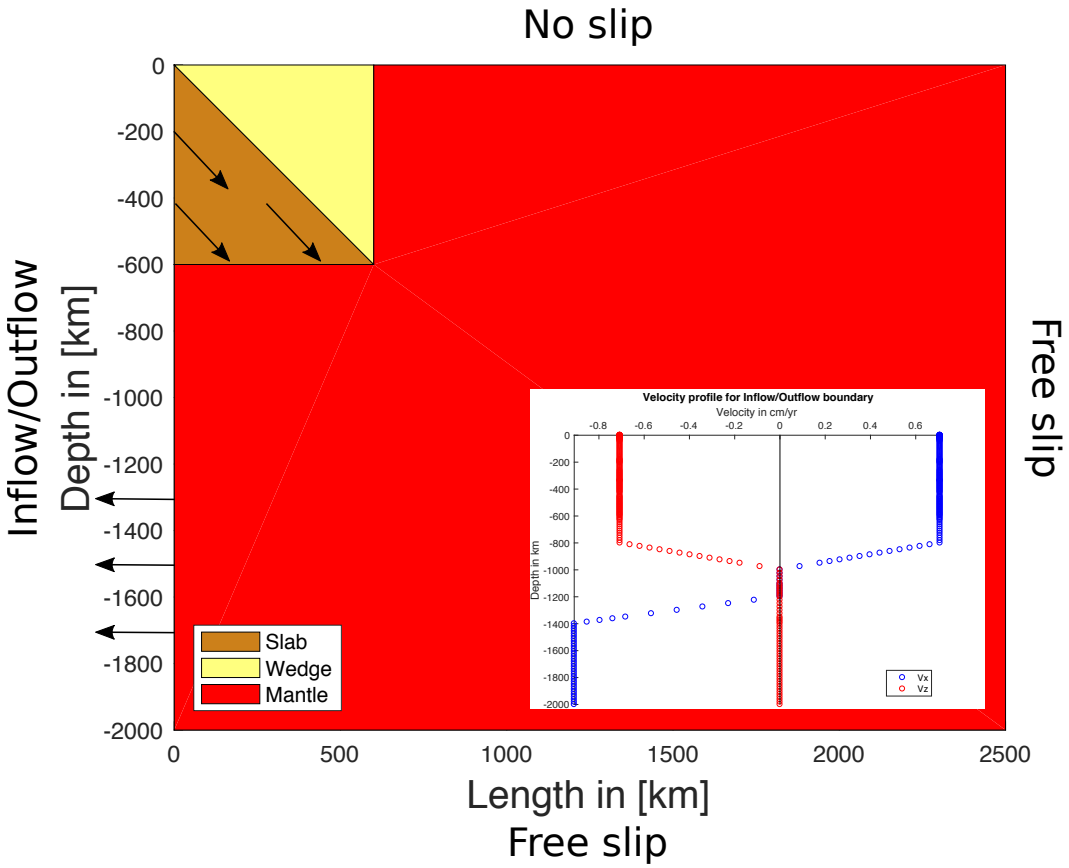

Figure 6.2: Model setup as used in the simulations. The inset represents the given velocity profile of the left inflow/outflow boundary. Brown color shows the slab, whereas yellow color represents the mantle wedge and red color the remaining mantle. Boundary conditions are set as indicated.

The top boundary mimics a rigid continental plate and therefore the boundary condition is set to no slip. Free slip conditions are employed at the right and bottom boundary. To conserve mass and momentum within the modelled domain the amount of material which is introduced into the domain via the subducting slab needs to be extracted elsewhere. For this reason inflow/outflow boundary conditions are implemented at the left side of the domain. The used velocity profile is shown in Fig. 6.2; inset. In the future an initial temperature profile will be set according to the subduction benchmark of van Keken et al. (2008). The temperature profile of the subducting slab will be computed numerically solving a 1D heat-diffusion equation for a half space cooling model. Isothermal top and bottom boundaries will be set to 20 and 1350 °C, whereas the left and right boundary will be set to zero flux.

6.4 Results

6.4.1 Corner flow

To produce reasonable results the code is tested against a benchmark for subduction zones (van Keken et al., 2008). Several previous studies (Spiegelman and McKenzie, 1987; Davies and Stevenson, 1992; Iwamori, 2007) used an analytical solution based on the corner flow of Batchelor (1967):

$$f(\theta) = A' sin(\theta) + B' cos(\theta) + C' \theta sin(\theta) + D' \theta cos(\theta), \tag{133}$$

with θ is the dip angle of the slab and A' to D' are computed prefactors as stated below:

$$A' = -\theta_0^2, \tag{134}$$

$$B' = 0, \tag{135}$$

$$C' = \theta - sin(\theta_0) cos(\theta_0), \tag{136}$$

$$D' = sin^2(\theta_0), \tag{137}$$

with $\theta_0 = 90° - \theta$. Figure 6.3 shows the analytical solution for the corner flow between two fixed plates as derived by Batchelor (1967). Velocities within the slab are prescribed using internal boundary conditions and are not part of the computed analytical solution, which only applies for the mantle wedge.

Figure 6.4 **a)+b)** present the absolute error between the computed velocities from MVEP2 and the analytical solution of Batchelor (1967). As the corner flow of

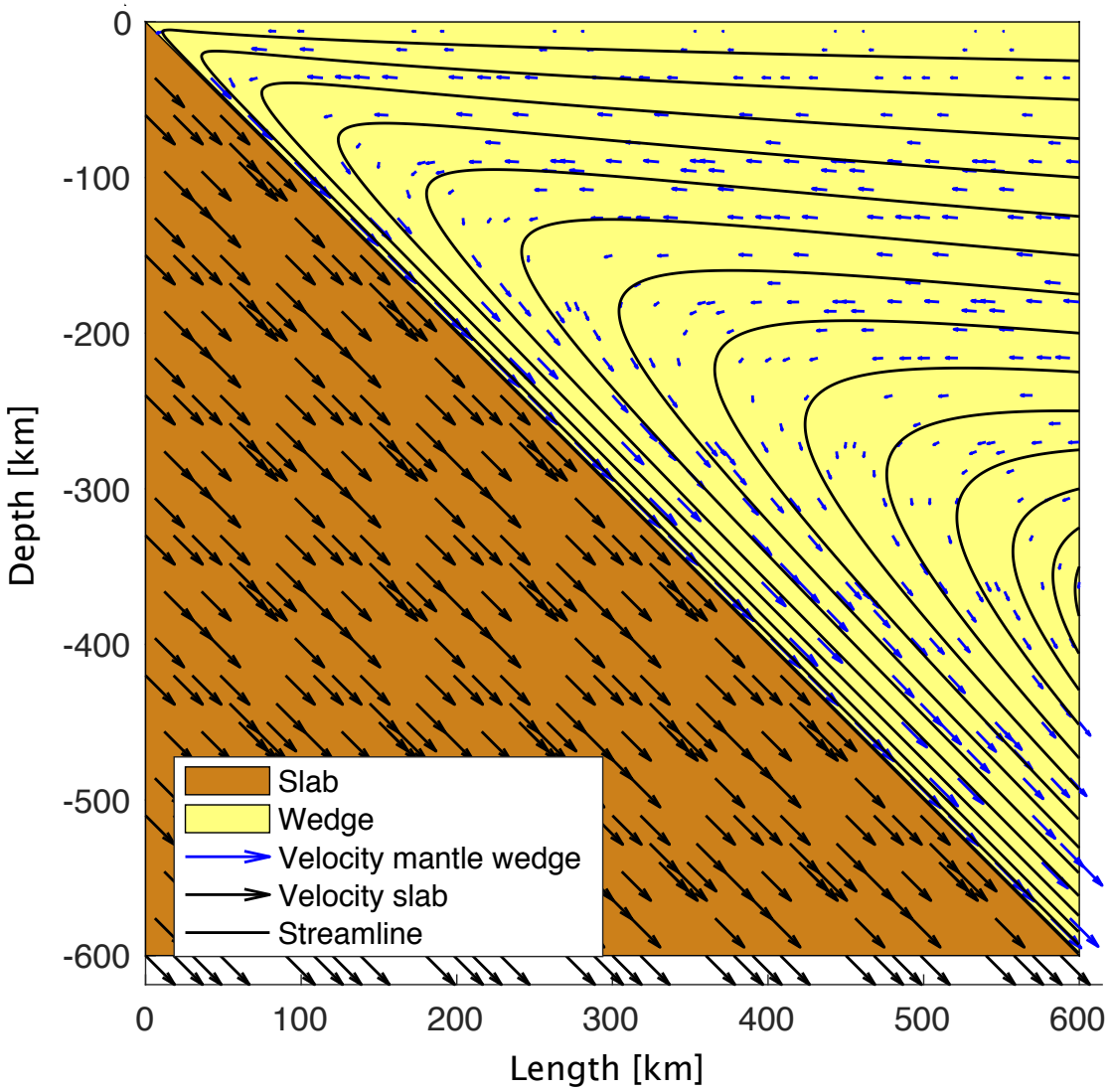

Figure 6.3: Computed analytical solution of flow between two fixed plates (Batchelor, 1967). Black arrows represent prescribed velocities in the slab due to internal boundary conditions. Blue arrows symbolize computed velocities of the analytical solution from Batchelor (1967). Additionally black lines show computed streamlines of the analytical solution.

Batchelor (1967) is only valid for the mantle wedge, velocities computed outside the wedge introduce some errors at the boundary between mantle wedge and mantle domain. To avoid these errors within the corner flow we extended the slab by about 100 km, which results in excellent agreement with the analytical solution of Batchelor (1967).

6.4.2 Water migration scheme

Subducting crust provides water to the mantle in two ways: (1) free water that is contained in the pore space of the rocks and may percolate along grain boundaries (Miller et al., 2003; Abers, 2005) and (2) chemically bound water in crystal structures

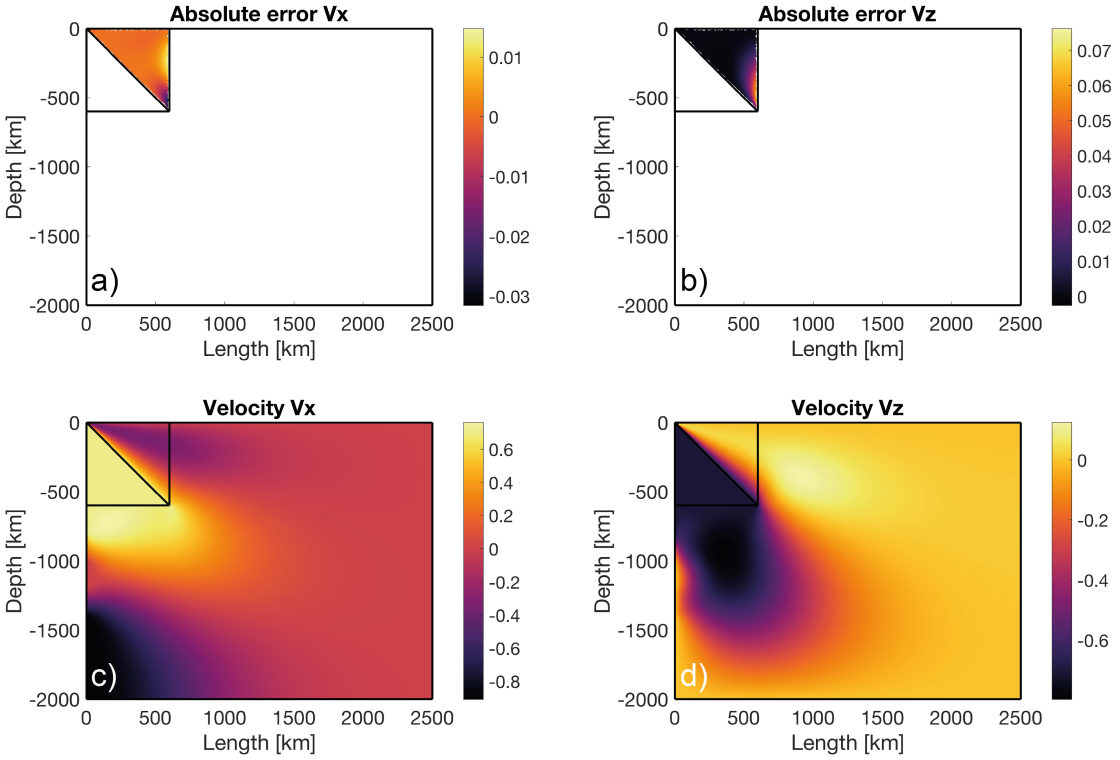

Figure 6.4: **a) + b)** show the absolute error of velocity in x and y direction in comparison to the analytical solution of Batchelor (1967). As the analytical solution is only valid for the corner flow, prescribed velocities in the slab and computed velocities in the remaining domain are left blank. **c)+d)** represent computed velocities in x and y direction. Black lines contour the slab and mantle wedge.

(Davies, 1999; Stern, 2002). Once a slab starts subducting, free water stored in the pore space of the rocks is released through compression and is not transported further into the mantle. Hydrated minerals like chlorine, serpentine and amphibole release mineralogically bound water when they undergo phase transitions.

In general, water migration can be modelled as a two-phase flow, but as we are interested in a first order estimate of water migration behaviour, we try to keep the models as simple as possible. We follow the work of Quinquis and Buiter (2014), in which mineralogically bound water is advected along the solid phase flow and free water migrates along pressure gradients. For this reason each marker of the model does not only contain information on material properties, but additionally on the amount of both bound and free water. The water migration scheme consists of three steps: (1) determine the amount of free and bound water as well as the maximum storage capacity of each marker. (2) extract pressure gradients of the solid phase flow to compute Darcy velocities. (3) advect free water with the computed Darcy velocities.

The interpolation of free water between markers and mesh is done using a k-nearest neighbour algorithm. If the amount of mineralogically bound water of the particle exceeds the water storage capacity it is oversaturated in water and dehydration occurs. The released free water moves through the model along the corresponding pressure gradients. If the mineralogically bound water of the marker is below the storage capacity it is undersaturated in water and no free water is released. Instead it can incorporate free water, which was released through dehydration of oversaturated markers. The velocity of the Darcy flow in x- and z-direction is computed via (Faccenda et al., 2009, 2012):

$$v_{fx} = v_s - \frac{k\Delta P_x}{\eta_f \phi}, \tag{138}$$

$$v_{fz} = v_s - \frac{k(\Delta P_z - \rho_f g)}{\eta_f \phi}, \tag{139}$$

where v_s is the velocity of the solid, k is the permeability, ΔP the pressure difference in x- and z- direction, ρ_f the fluid density, η_f the fluid viscosity, ϕ is the porosity and g the gravitational acceleration.

Figure 6.5 shows the time evolution of a test setup assuming a rising sphere of free water. At the beginning of the simulation the sphere is oversaturated in water, whereas the surrounding rock is undersaturated. Due to the positive buoyancy the free water moves upwards. During its rise, free water is absorbed by the previously unsaturated rock until no free water is left. This benchmark shows that water is

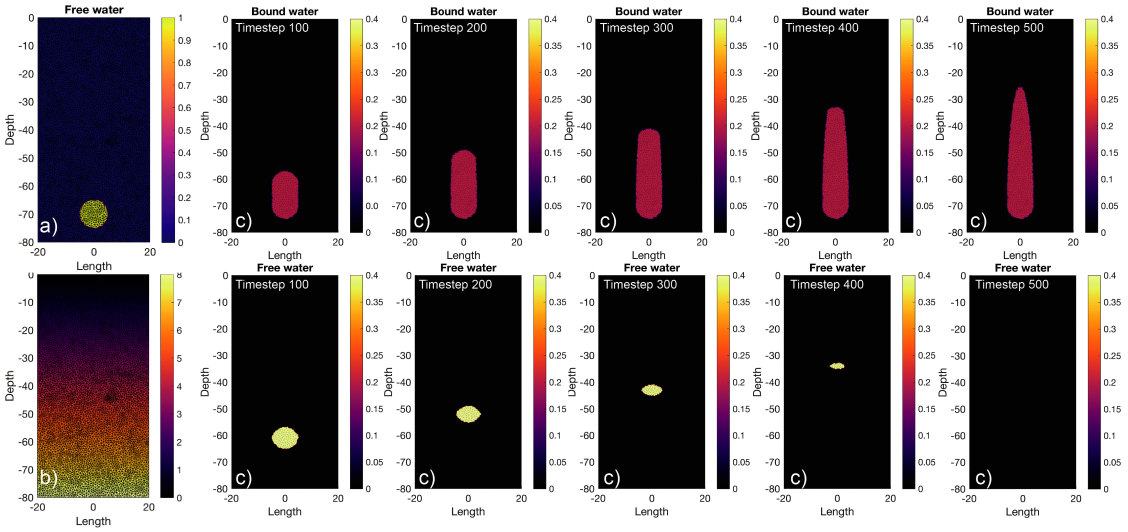

Figure 6.5: Benchmark setup of an hydrated sphere. **a)** shows the initial setup. An oversaturated sphere is placed within an undersaturated material. **b)** represents the applied pressure gradient in non-dimensional units. **c)** shows the model evolution over time. The free water moves upwards and is consumed by the undersaturated rock material. In the last timestep free water is completely incorporated into the surrounding rocks. All parameters in this model are non-dimensional.

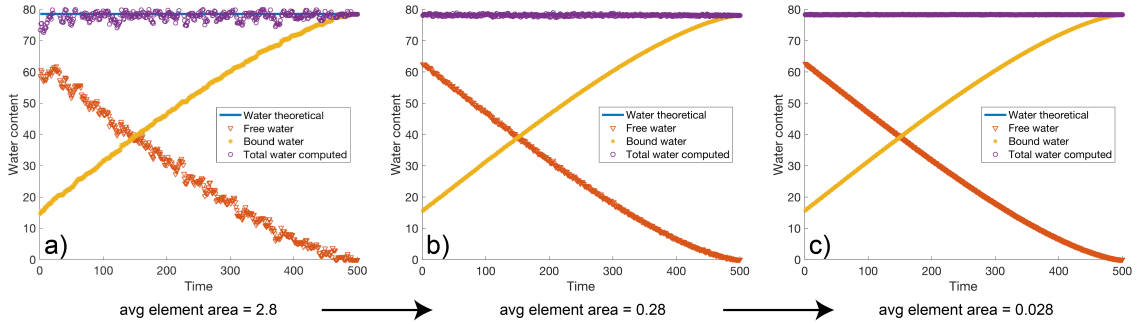

Figure 6.6: Conservation of water using different element areas. Units of water content are non-dimensional.

conserved over time (Fig. 6.6). Figure 6.6 a)-c) shows that with increasing numerical resolution the conservation of water improves. Therefore we are confident that a minimum average element area of 0.2803 (non-dimensional) as used in Fig. 6.6b is sufficient for our simulations.

6.5 Conclusion

The present study demonstrates that MVEP2 is capable of successfully reproducing the analytical solution of Batchelor (1967). To simulate fluid flow the water migration scheme from Quinquis and Buiter (2014) was implemented and tested. Further studies are required to include sediments on top of the slab storing additional free water and a rigid plate at the top boundary. Also a temperature field needs to be included and its evolution tested against a benchmark for subduction zones by van Keken et al. (2008). In the final steps distinct zones (e.g. fault zones, fractures) with increased permeability and high amount of water will be introduced. During the simulations the amount and geometry of the distinct zones will be changed systematically to investigate their influence on the resulting fluid flow in the subducting slab and the mantle wedge. Additonally to simulate the effect of dipping angle and subduction velocity on the amount of water transported into the mantle both parameters will be changed systematically.

Symbol	Description	Proposed value
d_{sediment}	Thickness sediment (km)	6 (Turcotte and Schubert, 2002)
d_{plate}	Thickness rigid plate (km)	50 (van Keken et al., 2008)
d_{slab}	Thickness slab (km)	60 (Clauser, 2014)
v_{slab}	Velocity slab (cm/yr)	1-5 (Morishige and van Keken, 2018)
A_{slab}	Dip angle slab (°)	20-60
ρ_{sediment}	Density sediment (kg/m^3)	2600 (Athy, 1930)
ρ_{plate}	Density rigid plate (kg/m^3)	2700 (Athy, 1930)
ρ_{slab}	Density slab (kg/m^3)	2900 (Turcotte and Schubert, 2002)
ρ_{mantle}	Density mantle (kg/m^3)	3300 (Wilson et al., 2014)
$\rho_{0\text{f}}$	Density fluid (kg/m^3)	1000 (Morishige and van Keken, 2018)
η_{sediment}	Viscosity sediment (Pa s)	10^{20}
η_{plate}	Viscosity rigid plate (Pa s)	10^{24}
η_{slab}	Viscosity slab (Pa s)	10^{24} (Morishige and van Keken, 2018)
η_{mantle}	Viscosity mantle (Pa s)	10^{21} (Clauser, 2014)
T_{mantle}	Temperature mantle (°C)	1400 (Wilson et al., 2014)
T_{surface}	Temperature surface (°C)	273 (Wilson et al., 2014)
T_{age}	Thermal age slab (Ma)	50 (Wilson et al., 2014)
κ	Thermal conductivity (W/(mK))	10^{-6}
g	Gravitational acceleration (m/s^2)	9.81

Table 6.1: Table representing model parameters that will be used in further simulations. Additionally viscosities of the materials will also be changed to test different dislocation and diffusion creep laws. So far these model parameters are suggestions and no simulations have been run using the values given above.

References

Abers, G. A., van Keken, P. & Hacker, B. (2017). The cold and relatively dry nature of mantle forearcs in subduction zones. *Nature Geoscience*, *10*, 333–337. doi:10.1038/ngeo2922

Abers, G. A. (2005). Seismic low-velocity layer at the top of subducting slabs: observations, predictions, and systematics. *Physics of the Earth and Planetary Interiors*, *149*(1), 7–29. doi:10.1016/j.pepi.2004.10.002

Angiboust, S., Wolf, S., Burov, E., Agard, P. & Yamato, P. (2012). Effect of fluid circulation on subduction interface tectonic processes: Insights from thermo-mechanical numerical modelling. *Earth and Planetary Science Letters*, *357-358*, 238–248. doi:10.1016/j.epsl.2012.09.012

Athy, L. F. (1930). Density, Porosity, and Compaction of Sedimentary Rocks. *AAPG Bulletin*, *14*(1), 1–24. doi:10.1306/3D93289E-16B1-11D7-8645000102C1865D

Batchelor, G. K. (1967). *An Introduction to Fluid Mechanics*. Cambridge: Cambridge University Press.

Bell, D. R. & Rossman, G. R. (1992). Water in Earth's Mantle: The Role of Nominally Anhydrous Minerals. *Science*, *255*(5050), 1391–1397. doi:10.1126/science.255.5050.1391

Cagnioncle, A., Parmentier, E. M. & Elkins-Tanton, L. T. (2007). Effect of solid flow above a subducting slab on water distribution and melting at convergent plate boundaries. *Journal of Geophysical Research: Solid Earth*, *112*(B9). doi:10.1029/2007JB004934

Cai, C., Wiens, D. A., Shen, W. & Eimer, M. (2018). Water input into the Mariana subduction zone estimated from ocean-bottom seismic data. *Nature*, *563*(7731), 389–392.

Carson, B. & Screaton, E. J. (1998). Fluid flow in accretionary prisms: Evidence for focused, time-variable discharge. *Reviews of Geophysics*, *36*(3), 329–351. doi:10.1029/97RG03633

Clauser, C. (2014). *Einführung in die Geophysik*. Berlin, Heidelberg: Springer. doi:10.1007/978-3-662-46884-5

Cuvelier, C., Segal, A. & van Steenhoven, A. (1986). *Finite Element Methods and Navier-Stokes Equations*. Mathematics and its applications. Dordrecht: Reidel.

Dabrowski, M., Krotkiewski, M. & Schmid, D. W. (2008). MILAMIN: MATLAB-based finite element method solver for large problems. *Geochemistry, Geophysics, Geosystems*, *9*(4). doi:10.1029/2007GC001719

Davies, J. H. (1999). The role of hydraulic fractures and intermediate-depth earthquakes in generating subduction-zone magmatism. *Nature*, *398*(6723), 142–145. doi:10.1038/18202

Davies, J. H. & Stevenson, D. J. (1992). Physical model of source region of subduction zone volcanics. *Journal of Geophysical Research: Solid Earth*, *97*(B2), 2037–2070. doi:10.1029/91JB02571

Faccenda, M., Burlini, L., Gerya, T. V. & Mainprice, D. (2008). Fault-induced seismic anisotropy by hydration in subducting oceanic plates. *Nature*, *455*(7216), 1097–1100. doi:10.1038/nature07376

Faccenda, M., Gerya, T. V. & Burlini, L. (2009). Deep slab hydration induced by bending-related variations in tectonic pressure. *Nature Geoscience*, *2*(11), 790–793. doi:10.1038/ngeo656

Faccenda, M., Gerya, T. V., Mancktelow, N. S. & Moresi, L. (2012). Fluid flow during slab unbending and dehydration: Implications for intermediate-depth seismicity, slab weakening and deep water recycling. *Geochemistry, Geophysics, Geosystems*, *13*(1). doi:10.1029/2011GC003860

Gerya, T. V. & Meilick, F. I. (2011). Geodynamic regimes of subduction under an active margin: effects of rheological weakening by fluids and melts. *Journal of Metamorphic Geology*, *29*(1), 7–31. doi:10.1111/j.1525-1314.2010.00904.x

Gerya, T. V., Stöckhert, B. & Perchuk, A. L. (2002). Exhumation of high-pressure metamorphic rocks in a subduction channel: A numerical simulation. *Tectonics*, *21*(6), 6-1-6-19. doi:10.1029/2002TC001406

Grove, T. L., Chatterjee, N., Parman, S. W. & Médard, E. (2006). The influence of H_2O on mantle wedge melting. *Earth and Planetary Science Letters*, *249*(1-2), 74–89. doi:10.1016/j.epsl.2006.06.043

Hacker, B. R. (2008). H_2O subduction beyond arcs. *Geochemistry, Geophysics, Geosystems*, *9*(3). doi:10.1029/2007GC001707

Hensen, C., Wallmann, K., Schmidt, M., Ranero, C. R. & Suess, E. (2004). Fluid expulsion related to mud extrusion off Costa Rica—A window to the subducting slab. *Geology*, *32*(3), 201–204. doi:10.1130/G20119.1

Hilton, D. R., Fischer, T. P. & Marty, B. (2002). Noble Gases and Volatile Recycling at Subduction Zones. *Reviews in Mineralogy and Geochemistry*, *47*(1), 319–370. doi:10.2138/rmg.2002.47.9

Hirth, G. & Kohlstedt, D. (2013). Rheology of the Upper Mantle and the Mantle Wedge: A View from the Experimentalists. In *Inside the subduction factory* (pp. 83–105). American Geophysical Union (AGU). doi:10.1029/138GM06

Iwamori, H. (1998). Transportation of H_2O and melting in subduction zones. *Earth and Planetary Science Letters*, *160*(1-2), 65–80.

Iwamori, H. (2007). Transportation of H_2O beneath the Japan arcs and its implications for global water circulation. *Chemical Geology*, *239*(3-4), 182–198. doi:10.1016/j.chemgeo.2006.08.011

Johnson, H. & Pruis, M. J. (2003). Fluxes of fluid and heat from the oceanic crustal reservoir. *Earth and Planetary Science Letters*, *216*(4), 565–574. doi:https://doi.org/10.1016/S0012-821X(03)00545-4

Kaus, B. J. P. (2010). Factors that control the angle of shear bands in geodynamic numerical models of brittle deformation. *Tectonophysics*, *484*(1-4), 36–47. doi:10.1016/j.tecto.2009.08.042

Korenaga, J. (2007). Thermal cracking and the deep hydration of oceanic lithosphere: A key to the generation of plate tectonics? *Journal of Geophysical Research: Solid Earth*, *112*(B5). doi:10.1029/2006JB004502

Korenaga, J. (2017). On the extent of mantle hydration caused by plate bending. *Earth and Planetary Science Letters*, *457*, 1–9. doi:10.1016/j.epsl.2016.10.011

Korenaga, J., Planavsky, N. J. & Evans, D. A. D. (2017). Global water cycle and the coevolution of Earth's interior and surface environment. *Philosophical Transactions of the Royal Society A: Mathematical, Physical and Engineering Sciences*, *375*(2094), 20150393. doi:10.1098/rsta.2015.0393

Magni, V., Bouilhol, P. & van Hunen, J. (2014). Deep water recycling through time. *Geochemistry, Geophysics, Geosystems*, *15*(11), 4203–4216. doi:10.1002/2014GC005525

Miller, S. A., van der Zee, W., Olgaard, D. L. & Connolly, J. A. D. (2003). A fluid-pressure feedback model of dehydration reactions: experiments, modelling, and application to subduction zones. *Tectonophysics*, *370*(1-4), 241–251. doi:10.1016/S0040-1951(03)00189-6

Moore, J. C. (1989). Tectonics and hydrogeology of accretionary prisms: role of the décollement zone. *Journal of Structural Geology*, *11*(1-2), 95–106. doi:10.1016/0191-8141(89)90037-0

Morishige, M. & van Keken, P. E. (2018). Fluid Migration in a Subducting Viscoelastic Slab. *Geochemistry, Geophysics, Geosystems*, *19*(2), 337–355. doi:10.1002/2017GC007236

Pawley, A. R. & Holloway, J. R. (1993). Water Sources for Subduction Zone Volcanism: New Experimental Constraints. *Science*, *260*(5108), 664–667. doi:10.1126/science.260.5108.664

Peacock, S. M. (1990). Fluid Processes in Subduction Zones. *Science*, *248*(4953), 329–337. doi:10.1126/science.248.4953.329

Popkin, B. M., D'Anci, K. E. & Rosenberg, I. H. (2010). Water, Hydration, and Health. *Nutrition Reviews*, *68*(8), 439–458. doi:10.1111/j.1753-4887.2010.00304.x

Quinquis, M. E. T. & Buiter, S. J. H. (2014). Testing the effects of basic numerical implementations of water migration on models of subduction dynamics. *Solid Earth*, *5*(1), 537–555. doi:10.5194/se-5-537-2014

Rüpke, L. H., Morgan, J. P., Hort, M. & Connolly, J. A. D. (2004). Serpentine and the subduction zone water cycle. *Earth and Planetary Science Letters*, *223*(1-2), 17–34. doi:10.1016/j.epsl.2004.04.018

Schmidt, M. W. & Poli, S. (1998). Experimentally based water budgets for dehydrating slabs and consequences for arc magma generation. *Earth and Planetary Science Letters*, *163*(1-4), 361–379.

Spiegelman, M. & McKenzie, D. (1987). Simple 2-D models for melt extraction at mid-ocean ridges and island arcs. *Earth and Planetary Science Letters*, *83*(1-4), 137–152. doi:10.1016/0012-821X(87)90057-4

Stern, R. J. (2002). Subduction zones. *Reviews of Geophysics*, *40*(4), 3-1-3-38. doi:10.1029/2001RG000108

Thielmann, M. & Kaus, B. J. P. (2012). Shear heating induced lithospheric-scale localization: Does it result in subduction? *Earth and Planetary Science Letters*, *359–360*, 1–13. doi:10.1016/j.epsl.2012.10.002

Thielmann, M., May, D. A. & Kaus, B. J. P. (2014). Discretization Errors in the Hybrid Finite Element Particle-in-cell Method. *Pure and Applied Geophysics*, *171*(9), 2165–2184. doi:10.1007/s00024-014-0808-9

Turcotte, D. L. & Schubert, G. (2002). *Geodynamics*. New York: Cambridge Univ. Press.

van Keken, P. E., Currie, C., King, S. D., Behn, M. D., Cagnioncle, A., He, J., ... Spiegelman, M. et al. (2008). A community benchmark for subduction zone modeling. *Physics of the Earth and Planetary Interiors*, *171*(1), 187–197. doi:10.1016/j.pepi.2008.04.015

van Keken, P. E., Hacker, B. R., Syracuse, E. M. & Abers, G. A. (2011). Subduction factory: 4. Depth-dependent flux of H_2O from subducting slabs worldwide. *Journal of Geophysical Research: Solid Earth*, *116*(B1). doi:10.1029/2010JB007922

von Huene, R. E. & Scholl, D. W. (1991). Observations at convergent margins concerning sediment subduction, subduction erosion, and the growth of continental crust. *Reviews of Geophysics*, *29*(3), 279–316.

Wallace, P. J. (2005). Volatiles in subduction zone magmas: concentrations and fluxes based on melt inclusion and volcanic gas data. *Journal of Volcanology and Geothermal Research*, *140*(1), 217–240. doi:10.1016/j.jvolgeores.2004.07.023

Wallmann, K. (2001). The geological water cycle and the evolution of marine $\delta^{18}O$ values. *Geochimica et Cosmochimica Acta*, *65*(15), 2469–2485. doi:10.1016/S0016-7037(01)00603-2

Wilson, C. R., Spiegelman, M., van Keken, P. E. & Hacker, B. R. (2014). Fluid flow in subduction zones: The role of solid rheology and compaction pressure. *Earth and Planetary Science Letters*, *401*, 261–274.

Zhou, Z., Lin, J., Behn, M. D. & Olive, J.-A. (2015). Mechanism for normal faulting in the subducting plate at the Mariana Trench. *Geophysical Research Letters*, *42*(11), 4309–4317. doi:10.1002/2015GL063917

Chapter 7 | Resume and Outlook

Fluid flow is essential for several geological fields, including hydrogeology, petrology and volcanology. In geosciences several processes like volcanism are affected and controlled by fluid flow occurring on different length scales. In subduction zones, for example, dehydration of minerals releases water, which subsequently rises along grain boundaries into the mantle wedge, leading to partial melting and volcanism. Therefore this thesis had the aim to investigate fluid flow and its related parameters on different scales ranging from pore- to macroscale.

The first manuscript presents the benchmarking of the implementation of the stencil rescaling method into the Finite Difference code LaMEM. Code benchmarking against a set of simplified model setups, for which analytical solutions of permeability are known, show an increase in accuracy at no additional computational cost. Furthermore I present results on the computation of permeability for a Fontainebleau sandstone sample showing both numerical convergence and very good agreement with experimentally measured permeability. Fluid flow using non-Newtonian rheology gains significant interest for example due to the use of nanofluids in enhanced oil recovery. I therefore show also the ability of LaMEM to handle complex non-Newtonian rheologies by computing the fluid flow through a Fontainebleau sandstone using a power-law rheology. However, the computation of permeability for highly resolved rock sample images using LaMEM remains computationally expensive. Different methods can compute permeability more efficiently in terms of shorter computation times and less computational costs, but are only capable of using Newtonian rheology. With the ascent of new technologies like machine learning and increasing computational resources the computation of high resolution rock images will improve in the future and therefore provide new insights into morphology and fluid flow in three dimensional porous media.

To use this method for permeability prediction in large-scale numerical simulations, parameterizations of permeability from the micro- to the macroscale are needed. For this reason I sinter soda-lima glass bead samples with various porosities. Microstructural and flow parameters needed to predict permeability using the well-known Kozeny-Carman equation are determined by using image processing and LaMEM. The obtained modified Kozeny-Carman equation can be used to simulate fluid flow and therefore permeability in large-scale numerical models. However, in application to Earth's crust this parameterization represents sedimentary rocks down to ≈20 km. For instance, especially in subduction zones a large variety of rocks and compositions are present. To account for those more complex microstructures, which are important in subduction systems, parameterizations of permeability need to be performed according to the present study. Future work should include the microstructural analysis and computation of permeability and hydraulic tortuosity for

typical subduction zone rocks like antigorite. In subduction zones usually most of the sediments have anisotropic properties, which can develop through compaction. To which extent these properties influence permeability and therefore the fluid flow on the large-scale remains at the moment unclear.

Modelling fluid flow on the large-scale led me to investigate fluid flow within a subduction zone. For this purpose I designed a subduction zone setup, which is tested against an analytical solution for corner flow. To simulate fluid flow I implemented a water migration scheme, which allows chemically bound and pore water to move through the model domain. This scheme supports the hydration and dehydration of under- and oversaturated particles. First simulations show that the total amount of water remains constant, in case the numerical resolution is sufficiently high. Further studies are required including a benchmark of the temperature field based on a half-space cooling model and the addition of several normal faults, filled with free water. So far, in my models water, which is available through dehydration, is not capable of lowering the melting point in the mantle and therefore creating partial melting. Nevertheless, this study could give insights into water migration influenced by normals faults and its overall effect on subduction zone dynamics.

To conclude, this thesis provides the methodology to determine permeability on the microscale accurately using both Newtonian and non-Newtonian rheology. It furthermore provides an experimental and numerical workflow to parameterize permeability from the micro- to the large-scale and additionally investigates the fluid flow within a subduction zone. Future projects should apply the stencil rescaling method (see Section 4) on several, in particular anisotropic minerals occurring in subduction zones. This way parameterizations can be derived for permeability (see Section 5), which can be used as an input parameter for complex large-scale numerical simulations (see Section 6). These simulations could give new insights into the effect of anisotropic permeability on the fluid flow occurring in subduction zones, but moreover could provide estimates to which extent normal faults participate in storage and transport of water into the deeper mantle.

Acknowledgements

First of all I would like to thank my supervisors Prof. Dr. Gregor Golabek and Dr. Marcel Thielmann. It was a great pleasure working with you over the last three years. Thank you for your continuous support, encouragement and passion for research. You gave me the opportunity to follow my own ideas and helped me whenever I struggled. I enjoyed the conferences, workshops and inspiring discussions with you so much. Throughout my time here I grew not only scientifically but even more personally. I appreciate your support, especially towards and during my stay in Sendai and I am grateful for the time you spent visiting me.

Additionally I want to thank Prof. Dr. Michihiko Nakamura, Wakana Fujita, Dr. Satoshi Okumura and all members of the Volcanology and Geofluids Research Group at Tohoku University for the great time I had during my research stay and the fruitful discussions and collaboration. It was a great experience learning from you and get insights into experimental work.

I want to thank all colleagues at BGI, which I could meet over the last years. Special thanks goes to Nicki Siersch and Caterina Melai for support, advice, sports and coffee breaks.

And most importantly I want to thank my fiancée Bea for her patience, support and love. I know whenever I need you, you will be at my side for all the ways we are going, now and in the future.

Eidesstattliche Erklärungen

(§ 9 Satz 2 Nr. 3 PromO BayNAT)

Hiermit versichere ich eidesstattlich, dass ich die Arbeit selbständig verfasst und keine anderen als die von mir angegebenen Quellen und Hilfsmittel benutzt habe (vgl. Art. 64 Abs. 1 Satz 6 BayHSchG).

(§ 9 Satz 2 Nr. 3 PromO BayNAT)

Hiermit erkläre ich, dass ich die Dissertation nicht bereits zur Erlangung eines akademischen Grades eingereicht habe und dass ich nicht bereits diese oder eine gleichartige Doktorprüfung endgültig nicht bestanden habe.

(§ 9 Satz 2 Nr. 4 PromO BayNAT)

Hiermit erkläre ich, dass ich Hilfe von gewerblichen Promotionsberatern bzw. -vermittlern oder ähnlichen Dienstleistern weder bisher in Anspruch genommen habe noch künftig in Anspruch nehmen werde.

(§ 9 Satz 2 Nr. 7 PromO BayNAT)

Hiermit erkläre ich mein Einverständnis, dass die elektronische Fassung meiner Dissertation unter Wahrung meiner Urheberrechte und des Datenschutzes einer gesonderten Überprüfung unterzogen werden kann.

(§ 9 Satz 2 Nr. 8 PromO BayNAT)

Hiermit erkläre ich mein Einverständnis, dass bei Verdacht wissenschaftlichen Fehlverhaltens Ermittlungen durch universitätsinterne Organe der wissenschaftlichen Selbstkontrolle stattfinden können.

Bayreuth, den 25.06.2020

.....

(Ort, Datum, Unterschrift)